

Tracing the Faintest Milky Way Satellites

Shane Michael Walsh

September 2008

A thesis submitted for the degree of Doctor of Philosophy
of the Australian National University





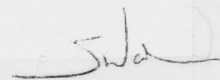
Declaration

The work in this thesis is my own except where stated below. Helmut Jerjen and Beth Willman were the principal supervisors of this work and have directed and contributed to the research, and are co-authors on the three papers that comprise this thesis.

Chapters 2, 3 and 4 have been submitted as a single article to the *Astronomical Journal*. The authors were Shane Walsh, Beth Willman and Helmut Jerjen. The introduction text was written by Beth and myself.

Chapter 5 was a letter published on June 20, 2007 in volume 662 of the *Astrophysical Journal*, pages L83-L86. The authors were Shane Walsh, Helmut Jerjen and Beth Willman. Helmut and Beth contributed to the editing of the text.

Chapter 6 has been accepted for publication as an article in the *Astrophysical Journal*. The authors were Shane Walsh, Beth Willman, David Sand, Jason Harris, Anil Seth, Dennis Zaritsky and Helmut Jerjen. The introduction and sections 6.4 and 6.5 were written by Beth and myself. The contributions of each author are as follows: Beth Willman - performed the data reduction and wrote the accompanying section, and produced Figure 6.2. Dave Sand - contributed to the acquisition, reduction, and analysis of the data. Jason Harris - contributed to the analysis of the data, in particular performed all of the artificial star testing and completeness limits. Anil Seth - contributed to data reduction, analysis and interpretation. Dennis Zaritsky - original PI of project with Beth Willman and played an advisory role in obtaining and interpreting observations. Helmut Jerjen - Contributed to the statistical analysis.



Shane Walsh

Acknowledgements

Many thanks go to my supervisor Helmut Jerjen, for offering perhaps the best PhD project Stromlo has ever seen, for supporting me over the last three years and change, and for the endless optimism. I am tremendously indebted to my NYU/CfA/Haverford supervisor Beth Willman, whose persistence (and patience) polished my work to a high sheen, and for introducing me to Armando's Pizzas and Subs.

I thank Armando's Pizzas and Subs for sustenance during time spent working at CfA, and the CfA Institute for Theory and Computation for the hospitality during my two visits.

This thesis benefited from the stimulating discussions over many McLunches, so thanks to Jose Robles, Brad Tucker and Chas Egan. Stromlo has been made a home by the fellow residents of House 10: Brad, Emma, Leith and particularly Mitey the Cat who always offered a fluffy, if somewhat diseased, tummy to rub at the end of a long day.

Finally thanks to my mum. Words can't express just how awesome she is.

Abstract

In the last three years the number of known Milky Way (MW) satellite galaxies has doubled, thanks to the Sloan Digital Sky Survey (SDSS), which has prompted a flurry of activity in the field of the missing satellites problem. The previously undetectable satellites can be located as statistically significant overdensities of resolved stars with colors and magnitudes consistent with old, metal poor stellar populations. The Australian National University is about to complete construction of the SkyMapper telescope which will produce a photometric catalog of the entire southern sky comparable with SDSS in the north. This thesis compiles the work resulting from the development of an algorithm for detecting MW satellites in just such a catalog, which was tested on SDSS Data Release 6 (DR6) in anticipation of SkyMapper and the *Stromlo Missing Satellites Survey*.

Beginning with the catalog of DR6 stellar sources, color and magnitude cuts are applied to enhance the signal of stellar overdensities indicative of low surface brightness dwarf spheroidal (dSph) MW companions. The remaining stars are then smoothed with a Plummer surface density profile and regions with a statistically significant density or characteristic area are flagged as detections. Applying this algorithm to DR6 yields detections of all 15 new MW satellites, six “classical” MW dSphs, and 19 globular or open clusters. One of the 15 detected new satellites was Boötes II, which was discovered with an early iteration of this algorithm. Background galaxies and galaxy clusters contaminate the detections, but 30 overdensities are detected with no known catalogued counterpart.

The detection limits of the DR6 survey were quantified by putting over 3,800,000 simulated galaxies through the algorithm with various combinations of luminosity, physical size, distance, and Galactic latitude. The resulting detection efficiency maps show a smooth transition from 100% to 0% efficiency, and that Galactic latitude does not play an overly important role over the DR6 footprint. From the simulations, it is shown that all objects brighter than $M_V \approx -6.5$ are detectable out to 300 kpc. Using the derived detection efficiencies of the known satellites and assuming Boötes II, Willman 1 and Segue 1 occupy dark matter halos, the total number of MW satellites over the entire sky is estimated to be ~ 224 . A substantial number of these will be detected by the Stromlo Missing Satellites Survey.

The newly discovered satellites are only observable as resolved stars, and having total luminosities comparable to that of individual stars means that consideration of small number statistics is critical when measuring the properties of the satellite as a whole. The ambiguous location of Boötes II in size-luminosity space means that robust estimates of its parameters, and their uncertainties, are necessary to make any statements regarding its classification as a dSph or globular cluster. A bootstrap analysis of MMT/Megacam imaging shows that Boötes II is indeed distinct from the globular cluster population, and tidal arguments further sway classification in favor of dSph. The nature of Boötes II — as well as Willman 1 and Segue 1 — has significant impact on the extrapolated total number of MW satellites; if these objects are not resident in dark matter halos then the estimate of ~ 224 satellites drops to ~ 52 . Therefore, not only discovering, but also carefully characterizing new satellites is important for increasing the sample of objects needed to reassess the missing satellites problem.

Contents

Declaration	iii
Acknowledgements	v
Abstract	vii
1 Introduction	1
1.1 Slingshot the Cosmic Web	1
1.2 The Cosmological Substructure Problem	2
1.3 Problems With the Substructure Problem	5
1.4 Thesis Outline	6
2 Survey Method	9
2.1 Introduction	10
2.2 SDSS Data	12
2.3 Survey Method	12
2.3.1 Data Management	13
2.3.2 Selection Criteria	13
2.3.3 Spatial Smoothing	14
2.3.4 Detection Threshold(s)	15
2.3.5 Identifying and Evaluating Detections	17
2.4 Application to SDSS Data Release 6	18
2.4.1 Candidate Milky Way Satellites	20
3 Simulations	27
3.1 Exploring Detection Efficiency With Synthetic Satellites	27
3.1.1 Sowing the Simulated Fields	27
3.1.2 Forging Virtual Dwarfs	29
3.1.3 Charting Detection Efficiency	30
3.2 Dissecting Efficiency Trends	30
3.2.1 Efficiency Versus Distance	33
3.2.2 Efficiency Versus Scale-length	34
3.2.3 Analytically Expressing Detection Efficiency	35
3.2.4 Efficiency Versus Latitude	35

3.2.5	Comparing R_{99} , R_{90} and R_{50}	37
3.2.6	Caveats	38
4	Survey Punchline: Discussion and Implications	43
4.1	Comparison With Koposov et al. (2008)	43
4.2	The Still Missing Satellites	45
4.3	Allowing a Little Latitude	46
4.4	Conclusion	49
5	A Pair of Boötes: A New Milky Way Satellite	53
5.1	Introduction	53
5.2	Data and Discovery	54
5.3	Candidate Properties	57
5.4	Discussion and Conclusion	60
6	Boötes II ReBoöted: MMT/Megacam Follow-up	63
6.1	Introduction	64
6.2	Data	65
6.3	Boötes II Properties	67
6.3.1	Bootstrap Analysis	67
6.3.2	Central Position	68
6.3.3	Distance	68
6.3.4	Stellar Population	69
6.3.5	Structural Parameters	70
6.3.6	Luminosity	71
6.3.7	Morphology	75
6.4	Is Boötes II dark matter dominated?	77
6.4.1	Separation in size-luminosity space from dwarf galaxies and globular clusters	78
6.4.2	Minimum mass-to-light ratio to be bound	80
6.4.3	Mass-to-light ratio inferred from the King tidal radius	80
6.5	Conclusion	82
7	Conclusion and Future Directions	85
7.1	The Future	87
A	Candidate Satellite Detections	89
	Bibliography	98

List of Figures

1.1	Via Lactea density map	4
2.1	CMD showing selection cuts	14
2.2	Distribution of $\max(S)$ values	17
2.3	“Detection” area vs. $\max(S)/S_{th}(n_*)$	18
2.4	DR6 footprint showing dSph positions	19
2.5	Same as Figure 2.3 with real detections overplotted	21
2.6	Spatial plots and CMDs of dSph detections	22
2.7	Spatial plots and CMDs of dSph detections <i>cont</i>	23
2.8	Spatial plots and CMDs of dSph detections <i>cont</i>	24
2.9	Detections of Abell 1413 and NGC 4486	25
2.10	Detections of four candidate dSphs	26
3.1	The fraction of sky as observed by SDSS DR6 at each latitude	28
3.2	Stellar density vs. absolute Galactic latitude	29
3.3	<i>HST</i> data of three MW satellite dSphs with SDSS isochrones	31
3.4	Simulated dSph systems	32
3.5	Detection efficiency for specific galaxy parameters	39
3.6	Comparison of simulated vs. semianalytical detection efficiency.	40
3.7	Detection efficienct maps at different latitudes	40
3.8	Completeness distances as a function of magnitude at three Galactic latitudes	41
3.9	Comparison of 50% detection distance with K08	42
4.1	Cumulative histograms of the Galactic latitude and longitud of DR6	48
5.1	Detection significance of Boötes II	55
5.2	Spatial plot of stars near Boötes I and II	56
5.3	Comparison of known objects with Boötes II detection	57
5.4	SDSS image centered on Boötes II with galaxies highlighted	58
5.5	Radial density profile of Boötes II	59
5.6	Absolute magnitude vs. half-light radius for Galactic companions discovered in SDSS.	61

6.1	CMD of Boötes II from SDSS and MMT/Megacam	67
6.2	CMD of Boötes II from MMT/Megacam with globular cluster fiducials overplotted	69
6.3	Spatial plot of stars passing selection cuts	72
6.4	Surface density profile of stars passing selection cuts	73
6.5	Density contour of King profile bootstrap results	74
6.6	Smoothed contour plot of Boötes II	76
6.7	Smoothed contour plot of 9 randomly selected resamples of Boötes II stars	77
6.8	Size-luminosity plot of known Galactic satellites	79
A.1	90
A.2	90
A.3	90
A.4	90
A.5	91
A.6	91
A.7	91
A.8	91
A.9	92
A.10	92
A.11	92
A.12	92
A.13	93
A.14	93
A.15	93
A.16	93
A.17	94
A.18	94
A.19	94
A.20	94
A.21	95
A.22	95
A.23	95
A.24	95
A.25	96
A.26	96
A.27	96
A.28	96
A.29	97
A.30	97

List of Tables

2.1	Angular sizes of the satellites detected in SDSS.	15
2.2	Positions of Strongest MW Satellite Candidates	20
3.1	Comparison of Interpolated and Analytical Detection Efficiencies	36
4.1	Summary of Comparison with Koposov et al. (2008).	45
5.1	Properties of Boötes II	59
6.1	Boötes II Properties from MMT/Megacam	83

Chapter 1

Introduction

*The bag's not for what I take, Colson,
it's for what I find along the way.*

–Angus MacGyver

1.1 Slinging the Cosmic Web

In 1922 Edwin Hubble used Cepheid variable stars to show that the Andromeda Nebula, and indeed all spiral nebulae, were not part of the Milky Way but were comparable stellar systems at then-inconceivably large distances. Since then we have observed tremendous variety in the properties of these island universes, or galaxies, the fundamental units of cosmology. It was the recession velocities of galaxies that told us the universe was expanding (Hubble & Humason, 1931), and the motion of galaxies both within clusters (Zwicky, 1937) and internally (Volders, 1959), that first alluded to dark matter. While there has been no direct detection of dark matter and its true nature still eludes understanding, it is now widely believed that dark matter dominates over baryonic matter and as such has heavily influenced the structure formation of the universe.

The currently accepted model of describing the evolution of the universe consists of cold dark matter plus Einstein's (in)famous cosmological constant Λ (Λ CDM). This cosmology has tremendous success in describing the transition from the smooth early universe as deduced from the cosmic microwave background (CMB, Penzias & Wilson, 1965; Spergel et al., 2007) to the filamentary large scale structure of galaxies observed by the Sloan Digital Sky Survey (SDSS, York et al., 2000a) and the 2dF Galaxy Redshift Survey (2dFGRS, Colless et al., 2001). A distinguishing feature of cold dark matter is the prediction that structure forms through hierarchical mergers (“bottom-up”), rather than through collapse and fragmentation (“top-down”) as predicted by hot dark matter models. Therefore, our own Galaxy would have formed through successive mergers of smaller building blocks, the dwarf galaxies.

The first observational evidence for such a scenario came from Searle & Zinn (1978) who found that the elemental abundances of globular clusters in the halo showed no

trend with galactocentric distance, as would be expected from a single formation event. Further evidence for discrete accretion events came from the dynamics of the Magellanic Stream (Kunkel, 1979) and its possible association with the MW dwarf spheroidals (Lynden-Bell, 1982; Majewski, 1994), and the presence of moving groups of halo stars (Arnold & Gilmore, 1992; Majewski et al., 1996). The process of accretion continues today, spectacularly illustrated by the Sagittarius dwarf (Ibata et al., 1994) and its trail of stellar debris (Ibata et al., 2001; Martínez-Delgado et al., 2001; Majewski et al., 2003). In the age of wide field photometric surveys, the MW halo has revealed many other signs of accretion events such as the Monoceros Ring (Newberg et al., 2002), the Orphan Stream (Belokurov et al., 2006a), and the $> 22^\circ$ tidal tails of the disrupting globular cluster Palomar 5 (Grillmair & Dionatos, 2006).

The Milky Way is a large spiral galaxy in the Local Group, a group of galaxies within a $\sim 1 \text{ Mpc}^3$ cube consisting of the two other large spirals M31 (Andromeda) and M33 (Triangulum), and at least four dozen dwarf galaxies, most of which are satellites of one of the much more luminous spirals. Dwarf galaxies may be the most dark matter dominated objects in the universe (e.g. Kleyna et al., 2001) and represent the overwhelming majority of all galaxies by number (e.g. González et al., 2006 and references therein). As the smallest surviving remnants of the formation of large scale structure, the Local Group dwarfs are excellent test particles for cosmological models on local scales. They are sufficiently close to allow detailed studies of their structure and kinematics, and they can be resolved into individual stars. Unfortunately for Λ CDM, it's success in the extragalactic arena has not been paralleled in the domain of near-field cosmology.

1.2 The Cosmological Substructure Problem

The currently favored “bottom-up” scenario of galaxy and structure formation can be traced to Peebles (1965), who suggested that rather than forming from a single gravitational collapse, a “galaxy of normal size” forms through successive accretion of gas clouds. The first cosmological N -body simulation was conducted by Press & Schechter (1974) and consisted of a gas of self-gravitating masses in an expanding Friedmann cosmology. The functional form of the resulting mass distribution of particle condensates agreed with the luminosity function of the Coma cluster, but the model lacked distinctness between scales (galaxies to galaxy clusters). White & Rees (1978) proposed a two-stage model of galaxy formation, in which a gravitationally dominant dark matter component collapses to form dark potentials, while the more centralized luminous mass is governed by dissipative gas dynamics within these potentials, accounting for characteristic size of galaxies. This idea was extended to study galaxy formation in a flat cold dark matter (CDM) universe by White & Frenk (1991) who incorporated gas dynamics, star formation and stellar feedback.

Early models of hierarchical merging found that little substructure (bound halos within larger halos) survived the accretion process. This led to Galactic halos with

a smooth internal DM distribution, a process referred to as “overmerging” (Katz & White, 1993; Summers et al., 1995; Frenk et al., 1996). This raised the question of how galaxies could remain intact within dense cluster halos and how satellite galaxies could survive within their host’s halo. The possible solution to this problem was the dissipative processes of baryons within the dark halos which centralized the baryons, increasing their resistance to disruption. Analytically, substructure was expected to survive dependent upon the density profiles in individual halos (Moore et al., 1996). Higher resolution simulations of clusters confirmed that overmerging was indeed predominantly due to lack of resolution and that galaxy sized halos survived within the larger cluster halo without the need for baryonic influence (Ghigna et al., 1998; Moore et al., 1998; Klypin et al., 1999a; Okamoto & Habe, 1999).

A semi-analytic model of galaxy formation put forward by Kauffmann et al. (1993) used observed properties of the Milky Way to tune their incorporated baryonic processes, which then successfully reproduced observed trends in the properties of the Virgo cluster. Applying the same parameters to a global galaxy population led to an over-estimate of B -band luminosity of the Universe by a factor of 2, implying that some halos remained undetectable. This work heralded the *missing satellites problem*, which received little attention until cosmological simulations caught up.

The first attempts to numerically study MW like halos came from Klypin et al. (1999b) and Moore et al. (1999). The former work examined MW and Local Group type environments in using two different CDM cosmologies and found both produced an overabundance of subhalos by a factor of ~ 5 times the known satellites of the MW and M31. The latter reported a more extreme overabundance by a factor of ~ 50 and noted that the dark matter substructure of a Galaxy sized halo was simply a scaled down version of that found within a cluster sized halo. Rather than solving the overmerging issue, these high resolution simulations seemed to have switched it’s polarity. The issue of abundant subhalos still persists in the recent Via Lactea (Diemand et al., 2007), the highest resolution simulation to date of a MW like halo (Figure 1.1), which finds over 2000 subhalos with mass greater than $4 \times 10^6 M_{\odot}$ within 389 kpc. In addition to the abundance of subhalos, Via Lactea also reveals sub-substructure and bound dark matter clumps interior to the Solar circle. Therefore the question is why the MW neighbourhood is not replete with observed substructure.

Proposed solutions to the missing satellites problem can be cosmological or astrophysical. Cosmological solutions require altering fundamental properties of dark matter, such as reducing the power of the primordial density fluctuations on small scales (Kamionkowski & Liddle, 2000; Zentner & Bullock, 2003), substituting CDM for warm dark matter (Colín et al., 2000; Bode et al., 2001), self-interacting dark matter (Spergel & Steinhardt, 2000), annihilating dark matter (Kaplinghat et al., 2000; Natarajan et al., 2008) or decaying dark matter (Abdelqader & Melia, 2008). These scenarios inhibit the formation of lower mass halos, whereas the more conservative astrophysical solutions reduce the efficiency of low mass halos to accrete and retain luminous matter. It is perhaps expected that the baryons in the shallow potentials of lower mass halos are more susceptible to the disruptive effects of cosmic reionization (Bullock et al., 2000;



Fig. 1.1 — Projected density map of dark matter taken from the Via Lactea Milky Way-size halo simulation. The map covers 800×600 kpc and is 600 kpc deep. The abundance of substructure far exceeds that observed around the Milky Way (Diemand et al., 2007).

Somerville, 2002), supernova feedback (Dekel & Silk, 1986; Mori et al., 2002), tidal stripping (Kravtsov et al., 2004), and/or ram pressure stripping (Mayer et al., 2006). This implies that the profusion of low mass subhalos is real, but we only observe some fraction that successfully accreted and retained gas to form stars. The effects of completely dark halos may be observable through gravitational lensing or disruptions to the MW disk, which could offer clues as to whether the cosmological or astrophysical solutions are responsible for the apparent lack of luminous substructure.

The deficit of observed satellites is not the only test for Λ CDM simulations. If the known MW satellites represent a luminous sub population of dark matter subhalos, then their spatial distribution should be consistent with that of the underlying subhalo distribution. Kravtsov et al. (2004) pointed out that the radial distribution of observed satellites was more compact than that of the Λ CDM subhalos, while Kroupa et al. (2005) found that the highly anisotropic “great disk of Milky-Way satellites” was inconsistent with essentially isotropic cosmological substructure at the 99.5% confidence level. HST proper motion measurements of several MW dSphs by Piatek et al. (2007) conclude that the great disk is not a kinematic structure, although Metz et al. (2008) argue that it may indeed be rotationally supported.

If cosmic reionization plays an important role in governing whether or not a subhalo will form and retain luminous matter, then the known dwarfs should correspond to the earliest forming subhalos and/or most massive before reionization. The luminous population of subhalos would therefore not be a reflection of the distribution of all subhalos, but of those that are more likely to be luminous. Libeskind et al. (2005) found the spatial distribution of the 11 MW satellites known at the time was similar to that of the subhalos that had the most massive progenitors, but significantly different to the distribution of the most massive present day subhalos. This was supported by Zentner et al. (2005), who then highlighted that an isotropic distribution of subhalos was not the correct null hypothesis for observationally testing Λ CDM. Both Libeskind et al. (2005) and Zentner et al. (2005) propose that a disc-like distribution of satellites can be recreated if subhalos are preferentially accreted into triaxial potentials along the filaments of the large scale cosmic web.

1.3 Problems With the Substructure Problem

Despite the progress in cosmological structure formation simulations and proposed explanations that can largely reconcile the discrepancy between simulations and observed properties of the MW neighbourhood, there are some rather serious caveats that must be considered. Firstly, simulated subhalos are subject to resolution issues; early N -body simulations produced smooth featureless dark matter halos (Summers et al., 1995; Frenk et al., 1996) which was later shown to be a numerical artifact (Klypin et al., 1999a). The high resolution Via Lactea simulation (Diemand et al., 2007) shows that galaxy halos contain tens of thousands of subhalos, an order of magnitude increase over previous simulations. This lack of convergence indicates that the results of simulations may

still be resolution-dependent, and that any explanations which could resolve the substructure problem as it stands now would have to be reconsidered if future simulations continue the trend.

Secondly, the ability to link the internal properties of observed MW satellites to that of simulated subhalos is tenuous at best. Subhalos are typically characterized by their peak circular velocity which is not directly related to an observable quantity. Converting an observed velocity dispersion to a peak circular velocity requires extrapolation based on the assumed cosmology and dark matter properties, and is also hampered by the fact that a dark halo typically extends significantly beyond the luminous stellar component. Strigari et al. (2007a) address this by instead using $M_{0.6}$, the mass within 0.6 kpc, to compare simulated subhalos with MW satellites. The $M_{0.6}$ mass function of MW satellites appears consistent with that of the most massive subhalos before their accretion in Via Lactea, thereby solving part of the substructure problem. However, one glaring issue remains: the incompleteness of the MW satellite census.

The final, and currently most readily rectified issue is that a substantial number of MW satellites still remain to be discovered. It had been recognized that some dSphs eluded discovery (Mateo, 1998; Willman et al., 2004), but it was the flurry of discoveries using the Sloan Digital Sky Survey (SDSS, York et al., 2000a) that showed just how many were missed. The SDSS Data Release 6 (DR6, Adelman-McCarthy et al., 2008) covers 9,500 square degrees, less than one quarter of the sky, yet it has nearly doubled the number of known MW satellites (Willman et al., 2005a,b; Belokurov et al., 2006b; Zucker et al., 2006b,a; Belokurov et al., 2007; Irwin et al., 2007; Walsh et al., 2007; Belokurov et al., 2008). This implies there is a significant number of dwarfs in the remaining sky that will be discovered in future surveys such as Pan-STARRS (Kaiser, 2004) and LSST (Ivezic et al., 2008). An imminent survey of the southern sky, dubbed the Stromlo Missing Satellites Survey, will be completed using the Australian National University's SkyMapper Telescope¹ and will produce a photometric catalog of comparable depth and quality to SDSS (Keller et al., 2007) which will almost certainly provide a wealth of new MW satellite discoveries. An algorithm to detect these satellites is the subject of this thesis.

1.4 Thesis Outline

This thesis presents the description and results of a Milky Way satellite detection algorithm developed using the Sloan Digital Sky Survey Data Release 6 (SDSS DR6, York et al., 2000a; Adelman-McCarthy et al., 2008). The aim of this in a larger context is the Stromlo Missing Satellites Survey² which will use the Australian National University's SkyMapper Telescope (Keller et al., 2007) to search the entire southern sky for previously unknown MW companions. Chapters 2, 3 and 4 comprise a paper concerning the details of the algorithm submitted to the *Astronomical Journal* (Walsh

¹<http://www.mso.anu.edu.au/skymapper/index.php>

²http://msowww.anu.edu.au/~jerjen/SMS_Survey.html

et al., 2008a). Chapter 5 is the Boötes II discovery paper as published in Walsh et al. (2007) and chapter 6 deals with MMT/Megacam followup of Boötes II (Walsh et al., 2008b).

Chapter 2 describes the algorithm in detail and the results of its application to DR6. After dividing the SDSS data into manageable portions, we describe the selection criteria used to remove contaminant foreground stars while preserving those of possible dwarfs. To quantify overdensities of selected stars we smooth the field with a Plummer surface density profile and define adaptive thresholds of signal peak and area. Applying this to DR6 reveals all known MW satellite galaxies and several globular clusters as well as background galaxies and galaxy clusters. Also identified are 30 unidentified overdensities, presented in Appendix A.

Chapter 3 concerns the simulations used to derive detection efficiencies of the algorithm as a function of various galaxy parameters. Using HST photometry of three MW dwarfs and SDSS field stars, over three million model galaxies are simulated and put through the algorithm. The resultant efficiency maps show the regions of parameter space any remaining hidden dwarfs are expected to occupy. Several parametrizations of the detection efficiency are presented to facilitate comparison of the observed dwarf population with theoretical predictions.

Chapter 4 compares the algorithm to a similar previous work (Koposov et al., 2008) and discusses what conclusions can be drawn from the survey and simulations. We make a back of the envelope estimate of how many MW satellites remain undetected within the DR6 footprint, and extrapolate this to estimate the total number of MW satellites. We also test to see if the detected objects are drawn from an isotropic distribution and discuss expectations for SkyMapper.

Chapter 5 reports the discovery of Boötes II and basic measurements of its structural properties using SDSS data. The detection algorithm was still in early stages and was substantially refined since the publication of this letter.

In chapter 6 improved measurements of Boötes II are derived using MMT/Megacam photometry. Because of the sparsity of stars in Boötes II, these measurements required a statistical approach. The aim of the paper was to determine whether Boötes II was a dwarf spheroidal galaxy or an extremely disrupting globular cluster. As would be shown in the results of chapter 4, the nature of Boötes II and fellow odd-ball objects Willman 1 and Segue 1 considerably alter the extrapolated estimate of the total number of Milky Way dwarf spheroidal satellites.

These chapters present the papers as they are published, except for Figure, Table and Section numbers and references which have been condensed into a global bibliography.

Chapter 2

Survey Method

Back off man, I'm a scientist.

–Peter Venkman

ABSTRACT

A specialized data-mining algorithm has been developed using wide-field photometry catalogs, enabling systematic and efficient searches for resolved, extremely low surface brightness satellite galaxies in the halo of the Milky Way (MW). Tested and calibrated with the Sloan Digital Sky Survey Data Release 6 (SDSS-DR6) we recover all 15 MW satellites recently detected in SDSS, six known MW/Local Group dSphs in the SDSS footprint, and 19 previously known globular and open clusters. In addition, 30 point-source overdensities have been found that correspond to no cataloged objects. The detection efficiencies of the algorithm have been carefully quantified by simulating more than three million model satellites embedded in star fields typical of those observed in SDSS, covering a wide range of parameters including galaxy distance, scale length, luminosity, and Galactic latitude. We present several parameterizations of these detection limits to facilitate comparison between the observed MW satellite population and predictions. We find that all known satellites would be detected with $> 90\%$ efficiency over all latitudes spanned by DR6 and that the MW satellite census within DR6 is complete to a magnitude limit of $M_V \approx -6.5$ and a distance of 300 kpc. Assuming all existing MW satellites contain an appreciable old stellar population and have sizes and luminosities comparable with currently known companions, we predict lower and upper limit totals of 52 and 340 MW dwarf satellites, respectively, within ~ 260 kpc if they are uniformly distributed across the sky. This result implies that many MW satellites still remain undetected. Identifying and studying these elusive satellites in future survey data will be fundamental to test the dark matter distribution on kpc scales.

2.1 Introduction

The dwarf galaxy population of the Milky Way (MW) provides invaluable insight into galaxy formation and evolution. Their resolved stars reveal formation histories and enable precise measurements of their structural parameters, ages and metallicities. These histories of individual, nearby systems provide a unique approach to studying the universe across the cosmic ages. Dwarf galaxies are also the most numerous type of galaxy in the universe (González et al., 2006) and are thought to be the building blocks of larger galaxies. Owing to their low masses, their properties may be strongly influenced by ionizing radiation in the early universe (Bullock et al., 2000; Somerville, 2002) and by the energy released by supernovae (Dekel & Silk, 1986; Mori et al., 2002). The impacts of both of these are weak links in our understanding of structure formation. Finding and studying nearby dwarfs of the lowest masses and luminosities is thus an essential component to understanding galaxy formation on all scales.

The MW dwarf galaxy population is also at present the most direct tracer of the abundance, mass spectrum, characteristic size, and spatial distribution of dark matter (DM) on subgalactic scales. Standard Λ cold dark matter (CDM) simulations of MW-size DM haloes predict many more DM subhalos than are observed as dwarf galaxies (Klypin et al., 1999b; Moore et al., 1999). The recent “Via Lactea” simulation contains 2000 DM subhalos within 289 kpc of the simulated primary galaxy (Diemand et al., 2007) which have no observed optically luminous counterparts. This discrepancy leads to the questions of how and in what mass regime baryons disappear from DM clumps. Studies of the spatial distributions of MW and M31 dwarf galaxy companions have also highlighted possible discrepancies between Λ CDM theory and observations (Kroupa et al., 2005; Kang et al., 2005; Metz et al., 2007).

The most obvious reason for these apparent discrepancies in the number and spatial distributions of dwarf galaxies is substantial incompleteness as the MW halo has not yet been uniformly searched for dwarf galaxy companions to low enough luminosities and star densities, in particular close to the Galactic plane where foreground contamination is severe. For example, Willman et al. (2004) compared the spatial distribution of MW satellites with that of M31’s population, as well as that of a simulated DM halo, and concluded that some dwarfs may have been missed at low Galactic latitudes and that the total number of MW satellites with properties similar to the known objects could be as many as triple the known population.

The viability of this solution, at least in part, has been underscored by the recent discoveries of 14 new Galactic companions from the photometric data of the Sloan Digital Sky Survey (SDSS). These objects all appear to be dominated by old ($\gtrsim 10$ Gyr) stellar populations, with the exception of Leo T (de Jong et al., 2008). Nine of these companions were immediately identified as dwarf spheroidal (dSph) galaxies: Ursa Major, Canes Venatici, Boötes, Ursa Major II, Canes Venatici II, Hercules, Leo IV, Coma Berenices, Leo T and Leo V (Willman et al., 2005b; Zucker et al., 2006b; Belokurov et al., 2006b; Zucker et al., 2006a; Belokurov et al., 2007; Irwin et al., 2007; Belokurov et al., 2008). Spectroscopic follow-up has confirmed that they all are highly

DM-dominated dwarf galaxies (Simon & Geha, 2007; Martin et al., 2007). Willman 1, Segue 1, and Boötes II (Willman et al., 2005a; Belokurov et al., 2007; Walsh et al., 2007) occupy a region of size–luminosity space not previously known to be inhabited by old stellar populations, at the intersection of MW dSphs and globular clusters. Spectroscopic studies (Martin et al., 2007) showed that Willman 1 may be resident inside a DM subhalo with a mass-to-light ratio of ~ 470 . If these ambiguous objects are gravitationally bound, then tidal arguments also favor them being DM-dominated (Walsh et al., 2008b). The remaining two objects discovered in SDSS, Koposov 1 and 2 (Koposov et al., 2007), are extremely faint Galactic globular clusters.

Numerous authors have shown that the predictions of Λ CDM simulations can be reconciled with the small number of observed MW dwarf galaxies if simple models for baryonic physical processes are taken into account when interpreting the results of numerical simulations (e.g. Bullock et al., 2001; Kravtsov et al., 2004; Simon & Geha, 2007). For example, Strigari et al. (2007a) show that the central masses ($M_{0.6kpc}$) of the MW dwarf galaxies are well constrained by the data and that their mass function closely matches the $M_{0.6kpc}$ mass function of both the earliest forming subhalos and the most massive accreted subhalos in the Via Lactea simulation.

A well-defined, deep survey of MW dwarf galaxies over a large fraction of the sky is critical to assess any of the above scenarios. The dwarf galaxies detected (or not) by such a survey will provide one of the best ways to rigorously test the Λ CDM paradigm by comparing a variety of metrics (distribution, mass, scale sizes, and number) of the MW dwarfs with the predictions of Λ CDM + galaxy formation models. Willman et al. (2002) and Koposov et al. (2008) have previously conducted automated searches for MW dwarfs in the SDSS and their corresponding detection limits. The original Willman et al. survey was only performed over a couple of thousand square degrees of sky. The Koposov et al. (2008) survey was performed with a more sensitive algorithm (critical, because they found many new satellites to be on the edge of detectability), but few galaxies were used to accurately quantify their detection limits.

In this paper, we present critical improvements to the present characterization of the detectability of MW dwarf galaxies over the ~ 9500 deg² of the SDSS in Data Release 6 (DR6). We also present an improved detection algorithm over previous searches. We aim to construct the most complete, well-defined census of MW satellites by embarking on a MW all sky satellite hunt. This search will ultimately combine SDSS DR6 (Adelman-McCarthy et al., 2008), the 2-Micron All Sky Survey (2MASS; Skrutskie et al., 2006) and the upcoming Southern Sky Survey (Keller et al., 2007). The Southern Sky Survey will cover the entire $\sim 20,000$ deg² below $\delta < 0^\circ$ using the new Australian National University (ANU) SkyMapper telescope equipped with a 5.7 deg² wide-field camera that is currently under construction, with survey operation expected to commence early 2009.

2.2 SDSS Data

The SDSS (York et al., 2000a) is an automated multicolor imaging and spectroscopic survey spanning 9500 deg^2 surrounding the North Galactic Pole. The $u, g, r, i,$ and z imaging data (Fukugita et al., 1996; Gunn et al., 1998) are photometrically and astrometrically reduced through an automatic pipeline (Hogg et al., 2001; Ivezić et al., 2004; Smith et al., 2002; Tucker et al., 2006; Pier et al., 2003). We subsequently correct for reddening with the Schlegel et al. (1998a) extinction values given in the SDSS catalog. All following work is performed on point sources from DR6, using the photometry flags from the examples of database queries appropriate for point sources available on the SDSS Skyserver Web site¹. To ameliorate effects of incompleteness in the point-source catalog and star/galaxy separation, we only consider sources brighter than $r = 22.0$. The photometric data are provided by the SDSS DR6 (Adelman-McCarthy et al., 2008).

2.3 Survey Method

Low surface brightness MW satellites are detectable only by their resolved stars. With the least-luminous known MW satellites, such as Boötes II, containing fewer than ~ 20 stars brighter than the main-sequence turn-off (MSTO, Walsh et al., 2008b), a deep, wide-field, uniform, multicolor photometric catalog is essential for searching for these objects. They will typically reveal their presence as statistically significant spatial overdensities relative to the Galactic foreground. Their signal can be enhanced by selecting stellar sources that are consistent in color–magnitude space with, for example, an old population of stars at a fixed distance. In this paper, we restrict ourselves to the old stellar populations characteristic of Local Group dSphs, but the population-specific elements of the algorithm can be easily modified for other systems. The strategy of our detection algorithm is built upon that of Willman et al. (2002) and Willman (2003) which utilized the photometric catalogs from SDSS and led to the discoveries of Ursa Major (Willman et al., 2005b) and Willman 1 (Willman et al., 2005a). It is also similar in spirit to Belokurov et al. (2007) and Koposov et al. (2008). Several systematic searches for MW dwarfs have also been done with non-SDSS data (Irwin, 1994; Kleyana et al., 1997; Whiting et al., 2007).

In summary, our algorithm applies color and magnitude cuts to stars in the DR6 catalog, stores their distribution in a spatial array with $0^{\circ}02 \times 0^{\circ}02$ pixels, spatially smoothes the array with a Plummer surface density profile, and sets comprehensive thresholds for detection. Each of these steps is described in detail in the following sections.

¹<http://cas.sdss.org/dr6/>

2.3.1 Data Management

In order to efficiently manage thousands of square degrees of survey data in a catalog containing tens of millions of stars, we first divide the data set (in the case discussed in this paper, SDSS DR6) into stripes, each spanning 3° in declination (to avoid projection effects) with 2° of overlap in declination between adjacent stripes. This overlap creates a substantial redundancy to ensure that real objects are situated in the central $\sim 2^\circ$ of declination in at least one stripe, away from possible edge-effects introduced at the stripe boundaries during the processing described in Section 2.3.3. We then take the longest continuous regions of the DR6 footprint in right ascension.

2.3.2 Selection Criteria

The mainly old, metal-poor stars of a nearby dwarf galaxy will occupy a well defined locus in the color–magnitude diagram (CMD), in contrast to MW stars which span a wide range in distance, age, and metallicity. Therefore selecting stars that are consistent in color–magnitude space with a population of old stars at a particular distance will significantly enhance the clustering contrast of a dwarf galaxy’s stars over the foreground noise from MW stars.

We use theoretical isochrones in SDSS filters from Girardi et al. (2004) to define the regions of $(g - r, r)$ space likely to be populated by old, metal-poor stars. Simon & Geha (2007) obtained spectra of stars in eight of the newly discovered dwarfs—CVn, CVn II, Com, Her, Leo IV, Leo T, UMa and UMa II—and found mean metallicities in the range $-2.29 < [\text{Fe}/\text{H}] < -1.97$. Based on this result, we consider isochrones for populations with metallicities of $[\text{Fe}/\text{H}] = -1.5$ and -2.27 (the lower limit in Girardi et al., 2004) and with ages 8 and 14 Gyr. Four isochrones in these ranges can be used to bound the region of CMD space we are interested in, namely the four combinations of $[\text{Fe}/\text{H}] = -1.5$ and -2.27 and ages 8 and 14 Gyr. Figure 2.1 shows these four isochrones projected to a distance of 20 kpc.

We define the selection criteria by the CMD envelope inclusive of these isochrones $\pm 1\sigma$ the $(g - r)$ color measurement error as a function of r magnitude. Shifting these isochrones over distances between $m - M = 16.5$ and 24.0 in 0.5 mag steps defines 16 different selection criteria appropriate for old stellar populations between $d \sim 20$ kpc and $\gtrsim 630$ kpc. We truncate our color–magnitude selection template at a faint magnitude limit of $r = 22.0$, beyond which photometric uncertainties in the colors and star/galaxy separation limit the ability to detect these populations. We also truncate the selection template at $g - r = 1.0$, as including redder objects adds more noise from MW dwarf stars than signal from more distant red giant branch (RGB) stars. Finally we do not include stars with δg or $\delta r > 0.3$ mag in our analysis. To efficiently select stars within this CMD envelope, we treat the CMD as an image of 0.025×0.125 (color \times mag) pixels and determine which stars fall into pixels classified as “good” according to the selection criteria. Figure 2.1 shows an example of the selection criteria, in this case for $m - M = 16.5$ (~ 20 kpc). The shaded region highlights pixels that would be classed as “good” for a system at ~ 20 kpc.

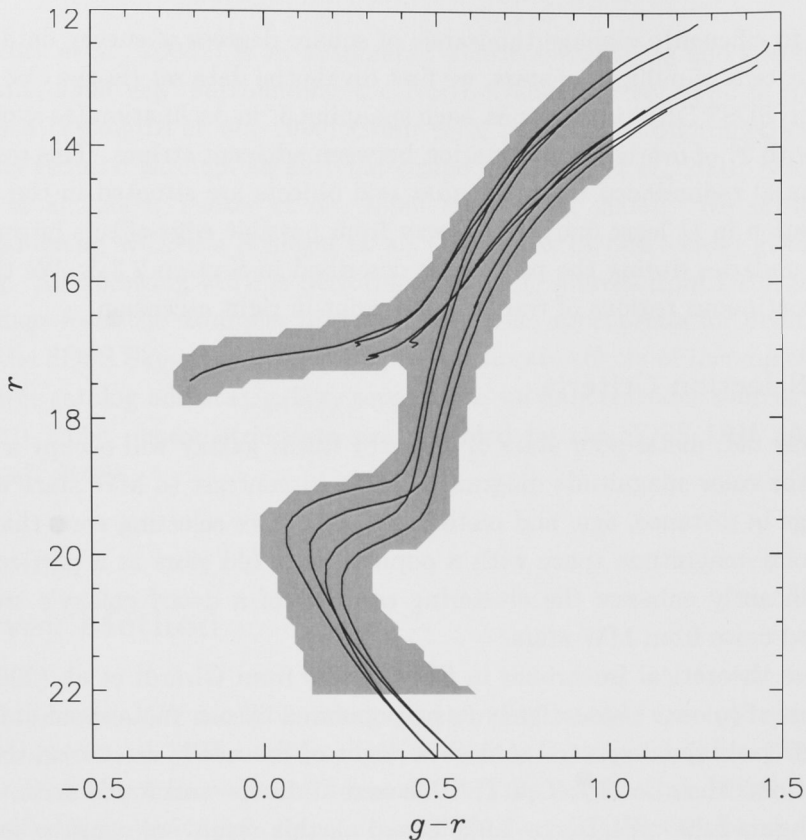


Fig. 2.1 — $(g-r, r)$ CMD showing the two reddest and two bluest theoretical isochrones for old stellar populations ($[\text{Fe}/\text{H}] = -2.27, -1.5$ and age = 8, 14 Gyr) at a distance modulus of $m-M = 16.5$ (~ 20 kpc), generated from Girardi et al. (2004). The shaded region shows pixels that pass the selection criteria.

2.3.3 Spatial Smoothing

After the photometric cuts are applied, we bin the spatial (R.A., decl.) positions of the selected stars into an array, E , with $0''.02 \times 0''.02$ pixel size. We then convolve this two-dimensional (2D) array with a spatial kernel corresponding to the expected surface density profile of a dSph. We refer to this smoothed spatial array as A . For our spatial kernel we use a Plummer profile with a $4''.5$ scale length. This value provides an effective compromise between the angular scale lengths of compact and/or distant objects with those of closer/more extended objects. For reference the angular sizes of the new satellites are listed in Table 2.1. We use the r_h values derived by Martin et al. (2008) except for Leo V (Belokurov et al., 2008).

The normalized signal in each pixel of A , denoted by S , gives the number of standard

Table 2.1. Angular sizes of the satellites detected in SDSS.

Object	r_h (arcmin)
Boötes	12.6
Boötes II	4.2
Canes Venatici	8.9
Canes Venatici II	1.6
Coma Berenices	6.0
Hercules	8.6
Leo IV	2.5
Leo V	0.8
Leo T	1.4
Segue 1	4.4
Ursa Major	11.3
Ursa Major II	16.0
Willman 1	2.3

deviations above the local mean for each element:

$$S = \frac{A - \bar{A}}{A_\sigma}.$$

The arrays of running means, \bar{A} , and running standard deviations, A_σ , are both calculated over a 0.9×0.9 window around each pixel of A . In particular, A_σ is given by

$$A_\sigma = \sqrt{\frac{n(A - \bar{A})^2 * B - ((A - \bar{A}) * B)^2}{n(n - 1)}}.$$

B is a box filter with n elements and is the same size as the running average window. The resulting array A_σ gives the standard deviation value for each pixel of A as measured over the 0.9×0.9 span of the filter. In the next section, we will define the detection threshold of this survey in terms of S , as well as in terms of the local stellar density E .

2.3.4 Detection Threshold(s)

In a large survey such as ours, it is critical to set detection thresholds strict enough to eliminate false detections but loose enough to retain known objects and promising candidates. To characterize the frequency and magnitude of purely random fluctuations in stellar density analyzed with our algorithm, we measure the maximum value of S for 199,000 $5.5 \times 3^\circ$ simulated fields of randomly distributed stars that have been smoothed

as described in the previous section. The only difference is that there is no gradient in stellar density across each field. In the interest of computational efficiency we do not use a running window for the mean and σ of each simulated field. The field size is chosen such that 1000 fields roughly total an area equal to the DR6 footprint (neglecting regions lost during convolution). We select 199 stellar densities n_* to simulate linearly spaced between 10 and 4000 stars per deg^2 . This range of stellar densities is to model the density range we find *after* applying the color–magnitude selection criteria described in Section 2.3.2 across the SDSS. In Section 3.1.1 we study the variation of detection limits with Galactic latitude (foreground stellar density); the typical number densities we will consider there are higher than 10–4000 stars per deg^2 because we wish to parameterize the detection limits in terms of the density of *all* stars bluer than $g - r = 1.0$ and brighter than $r = 22$.

Figure 2.2 shows a 2D cumulative histogram of the 199,000 $\max(S)$ values over a range stellar densities. In low density fields, the distribution of pixel values becomes non-Gaussian so a simple, global threshold value is insufficient. The solid gray line shows the contour containing 99% of the 199,000 $\max(S)$ values at each density. If we simply used a value like this as our threshold, we would be biasing ourselves against detecting extended objects; large angular scale length systems may not have a peak pixel value above this value, for example because stars in the object itself increases the local running mean and sigma. However, such an overdensity may have some characteristic area larger than any random fluctuation.

We thus define a detection threshold based on both the peak density and a characteristic area of an overdensity. To define such an area we scale down the 99% contour from Figure 2.2 and define a threshold density $S_{th}(n_*)$ as a function of stellar number density (white line in Figure 2.2). Then, using the 199,000 random fields we examine the relationship between the peak density $\max(S)$ divided by $S_{th}(n_*)$ and “detection” area, i.e., the area of contiguous pixels of S that have values above $S_{th}(n_*)$ (the white line). Figure 2.3 shows this area versus $\max(S)/S_{th}(n_*)$ for the random fields. If we assume a purely random foreground, we would expect one false detection in the DR6 footprint above an area of $\sim 55 \text{ arcmin}^2$ or above a peak density of $\sim 1.6 \times S_{th}(n_*)$. These numbers are set by the factor by which we scale down the threshold function and are themselves arbitrary.

Based on the results of these simulations we set the area threshold to a more conservative 60.0 arcmin^2 and the density threshold to a more conservative $1.75 \times S_{th}(n_*)$ to eliminate false positive fluctuations while preserving all of the known objects within DR6, including Boötes II (Walsh et al., 2007) and the Kaposov 1 and 2 globular clusters (Koposov et al., 2007). Thus, a detection is defined as a region where

- the area of a group of contiguous pixels of S above $S_{th}(n_*)$ (white line, Figure 2.2) is greater than 60.0 square arcminutes
- or*
- any single pixel of S is greater than $1.75 \times S_{th}(n_*)$.

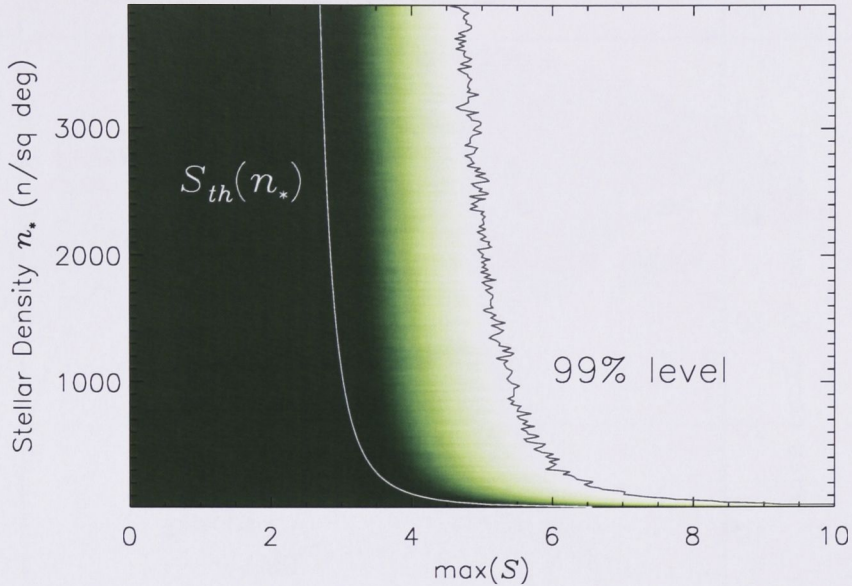


Fig. 2.2 — A 2D cumulative histogram showing the distribution of $\max(S)$ values for smoothed fields for a range of stellar densities n_* . The gray line bounds 99% of the $\max(S)$ values and the white line shows our threshold density, $S_{th} = f(n_*)$.

We implement these adaptive density thresholds as a function of local stellar density n_* , so that the algorithm may be run over large fields with varying density and allow direct comparison between fields of greatly different densities. The stellar density n_* is calculated for each pixel of the smoothed, normalized, spatial array S , as the $0\text{.}9 \times 0\text{.}9$ running average of the original spatial density array E .

To summarize our algorithm:

1. Apply CMD cuts, bin spatial positions of remaining stars into E .
2. Smooth E with Plummer profile to get A .
3. Calculate the $0\text{.}9 \times 0\text{.}9$ running mean \bar{A} and running standard deviation A_σ .
4. Define S as $S = (A - \bar{A})/A_\sigma$.
5. Calculate array of threshold values S_{th} as function of stellar density n_* (from $0\text{.}9 \times 0\text{.}9$ running mean of E).
6. Detections are where contiguous regions of pixels with $S > S_{th}(n_*)$ is greater than 60.0 arcmin^2 or any single pixel is greater than $1.75 \times S_{th}(n_*)$.

2.3.5 Identifying and Evaluating Detections

For each of our DR6 data strips defined in Section 2.3.1, the steps outlined in the previous sections are repeated in 0.5 mag distance modulus intervals, and these 16

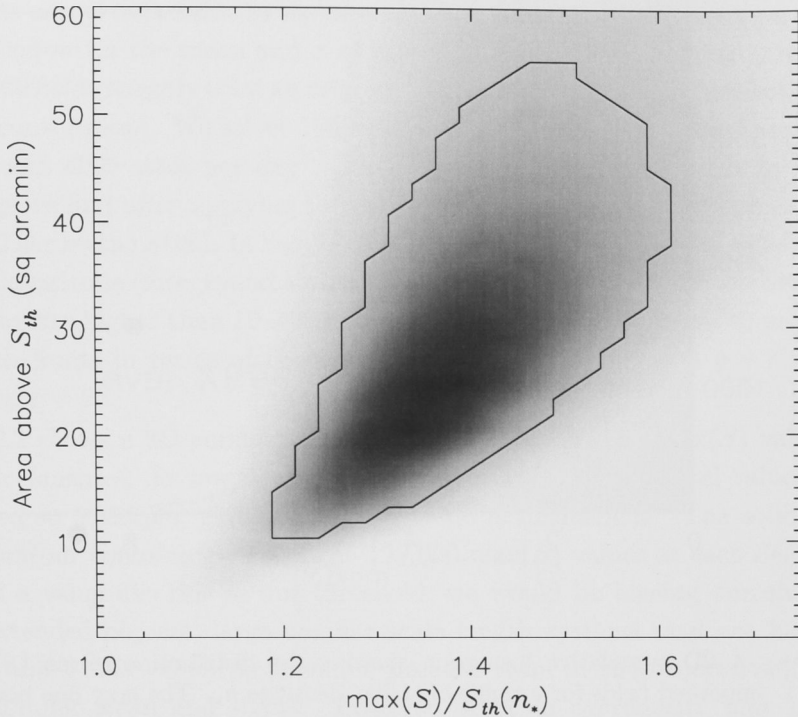


Fig. 2.3 — “Detection” area vs. $\max(S)/S_{th}(n_*)$ for the 199,000 random fields. The black contour shows the level at which purely random clustering would produce one false detection over the approximate area of DR6.

frames are layered to form a three-dimensional (3D) array. This 3D approach eliminates complications with multiple detections of a single object using selection criteria for different distance moduli, and selects out the strongest detection. The coordinates of stars within each detection and the CMD within the detection’s area are plotted for later visual inspection. Galaxy clusters and point sources around partially resolved background galaxies (such as their associated globular clusters) will contaminate the detections, but these can be identifiable based on their CMDs (see Section 2.4), leaving a list of potential new MW satellite galaxies and globular clusters. At this point, follow-up observations are typically necessary to confirm the existence and nature of these candidates.

2.4 Application to SDSS Data Release 6

We apply our search algorithm (as described in Section 2.3) to 21,439,777 sources with $r < 22.0$ and $g - r < 1.0$ in the 9500 deg² of imaging data in DR6 of the SDSS. The DR6 footprint is shown in Figure 2.4, along with previously known dSphs (open blue circles) and satellites discovered in SDSS (closed red circles).

The significance of our detections of known objects in terms of their peak density

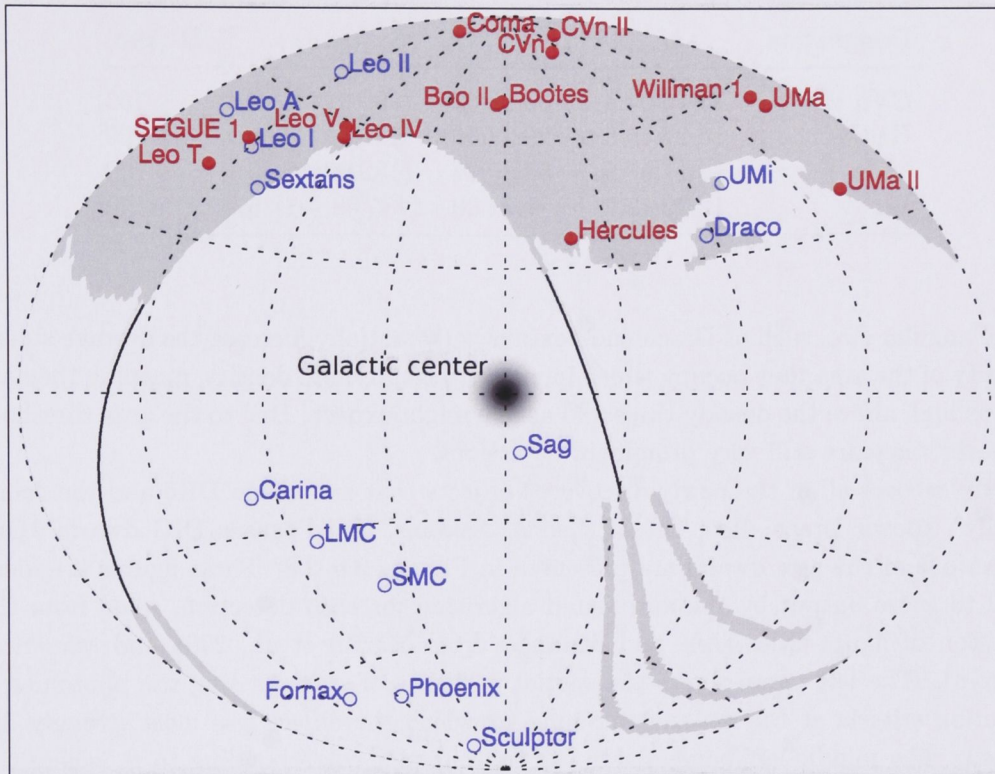


Fig. 2.4 — DR6 footprint in Galactic coordinates, centered on the Galactic center. Previously known dwarfs are marked with open blue circles, satellites discovered in SDSS are marked with filled red circles.

and area is shown in Figure 2.5. In the total area of DR6 analyzed, we find 100 unique detections above the thresholds, defined by the dotted lines of Figure 2.5. The positions of each of these detections are cross-referenced against the SIMBAD database² as well as visually inspected via the SDSS Finding Chart Tool³. Of our 100 detections, 19 are MW/Local Group dwarfs (counting Boötes II, Willman 1 and Segue 1), 17 are Galactic globular clusters (including Kopusov 1 and 2), two are known open clusters, 28 are clusterings of point sources associated with background galaxies such as unresolved distant globular clusters, and four are Abell galaxy clusters. The remaining 30 do not correspond to any cataloged objects, but CMDs of only a handful of these are consistent enough with a faint MW satellite to warrant follow-up. The remainder may be galaxy clusters whose detected center differs from its cataloged center by more than $\sim 0^{\circ}25$, or perhaps tidal debris. If the MW stellar halo is the result of accretion of dSph then evidence of this accretion is expected. It should be noted that objects with relatively

²<http://simbad.u-strasbg.fr/simbad/>

³<http://cas.sdss.org/astrodr6/en/tools/chart/chart.asp>

Table 2.2. Positions of Strongest MW Satellite Candidates

Designation	α	δ	(α, δ)	D (kpc)
CVn W	13:16:04.8	+33:15:00	(199.02, 33.25)	~ 160
Her X	16:27:45.6	+29:27:00	(246.94, 29.45)	~ 100
UMa Y	12:11:57.6	+53:35:24	(182.99, 53.59)	~ 100
Vir Z	12:20:19.2	-1:21:00	(185.08, -1.35)	~ 40

large angular size, such as Draco and Sextans, substantially increase the average stellar density of the area they occupy which increases the threshold density, meaning they are not as high above the density threshold as one might expect. Due to the area threshold however, they are still very prominent detections.

We recover all of the newly discovered objects that are within DR6 and the “classically” known Draco, Leo, Leo II, Leo A, Sextans, and Pegasus DIG dwarfs. Our detections of the new dwarfs are presented in Figures 2.6–2.8. These figures are identical to those output by the automated algorithm for each detection, aside from the addition of figure titles (M_V and distances from Martin et al., 2008 and references therein). The left panel shows the spatial positions of stars passing the photometric selection criteria at the distance modulus at which the object was most strongly detected. The middle-left panel shows the contour plot corresponding to S , where the contour levels are $S/S_{th}(n_*) = 1.0, 1.2, 1.4, 1.6, 1.8,$ and 2.0 . The middle-right panel is the CMD of the detection area and the right panel is the field-subtracted Hess diagram. The isochrone is that of a 13 Gyr, $[\text{Fe}/\text{H}] = -2.3$ from Girardi et al. (2004) at the distance specified. Besides demonstrating the effectiveness of our algorithm, these detections provide a benchmark with which to compare candidates and to determine which are consistent with being a new dwarf satellite.

To further illustrate the product of our algorithm we also show examples of undesired detections in Figure 2.9: the galaxy cluster Abell 1413 (top) and Virgo cluster galaxy NGC 4486 (bottom). These represent typical detections of background galaxies and galaxy clusters.

2.4.1 Candidate Milky Way Satellites

Figure 2.10 shows four unidentified overdensities that have CMDs qualitatively similar to that of a dSph. All show statistically significant spatial clustering and do not coincide with a visible overdensity of background galaxies. While several unknown detections have CMDs broadly consistent with old stellar populations, we present here four detections that are as strong as or stronger than the detections of UMa and PegDIG. We present their positions and distances estimated from the CMD in Table 2.2.

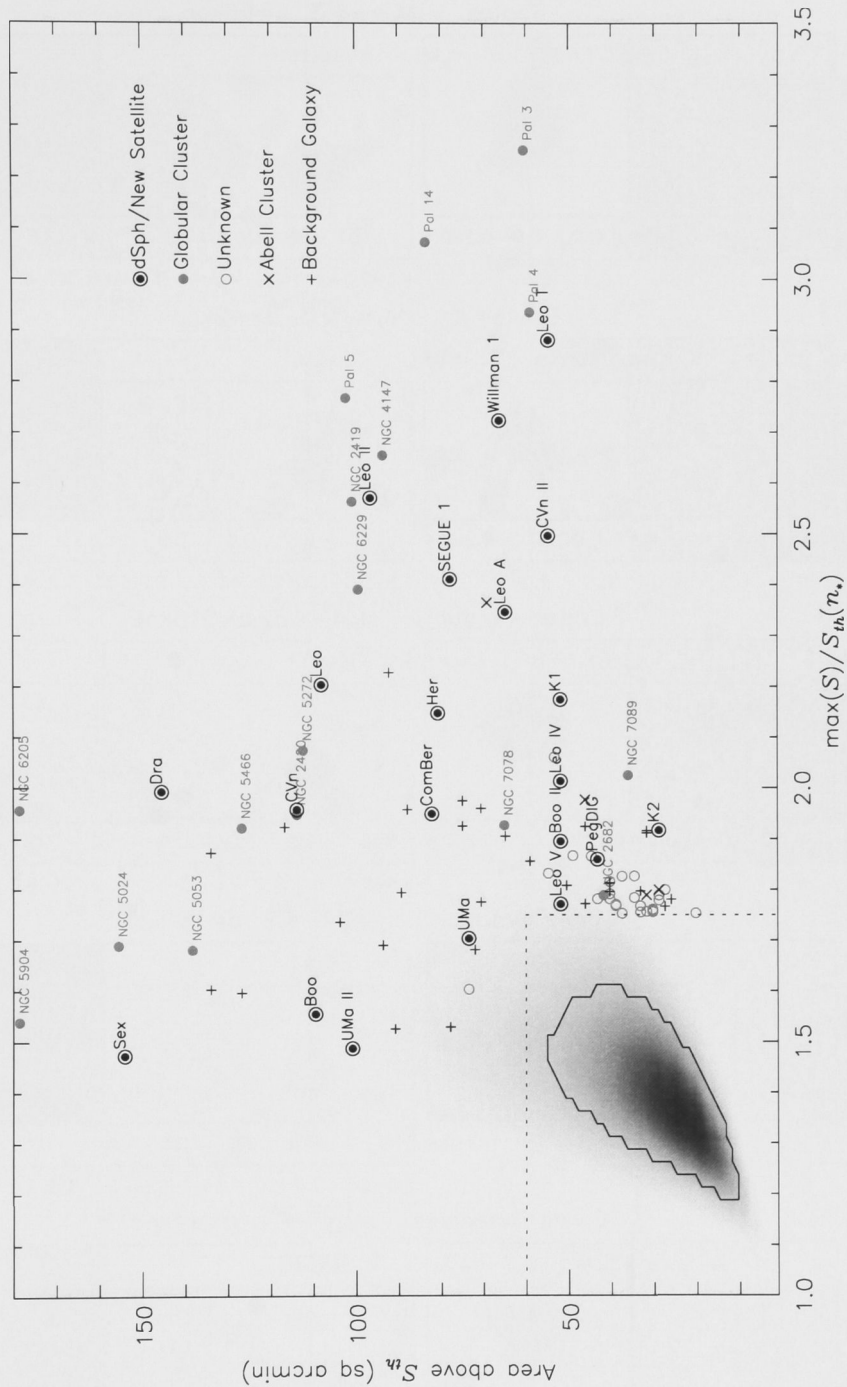


Fig. 2.5 — Same as Figure 2.3 but showing all detections in DR6. Dotted black lines show the adopted thresholds. Galactic/Local Group dSphs and Koysov 1 and 2 are shown as black filled circles. The brightest objects such as Draco and Sextans increase the average stellar density of the area they occupy, which increases $S_{th}(n_*)$ in their vicinity. This means that $\max(S)/S_{th}(n_*)$ is not as high as one might expect.

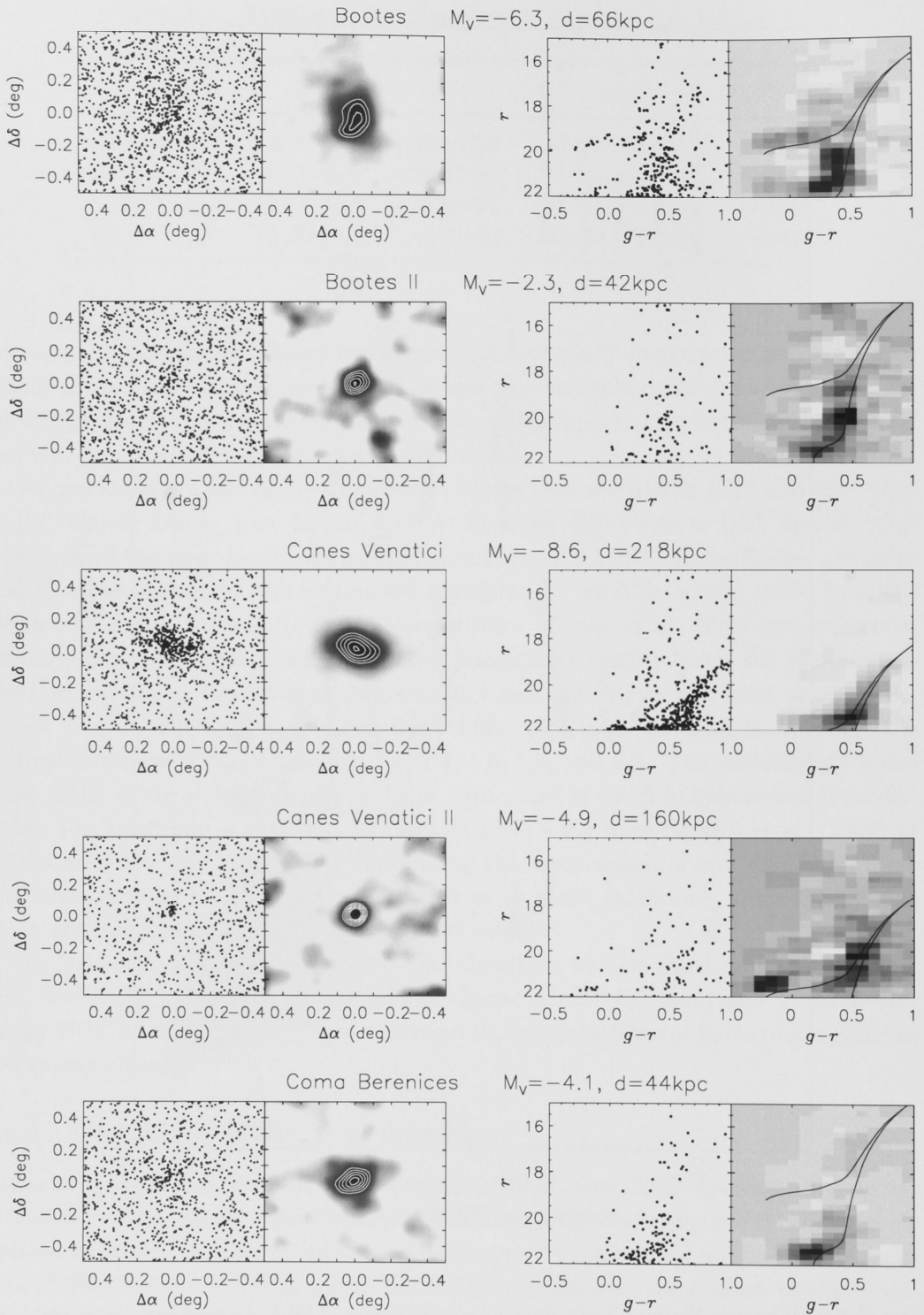


Fig. 2.6 — Our detections of recently discovered MW satellites. *Left*: spatial plot of sources passing selection cut. *Middle left*: contour of smoothed spatial plot. Contours show 1.0, 1.2, 1.4, 1.6, 1.8, and 2.0 times the density threshold. *Middle right*: CMD of region enclosed by contours. *Right*: Hess diagram of the same region, with 13 Gyr, $[\text{Fe}/\text{H}] = -2.3$ Girardi et al. (2004) isochrone at the object's distance overlotted.

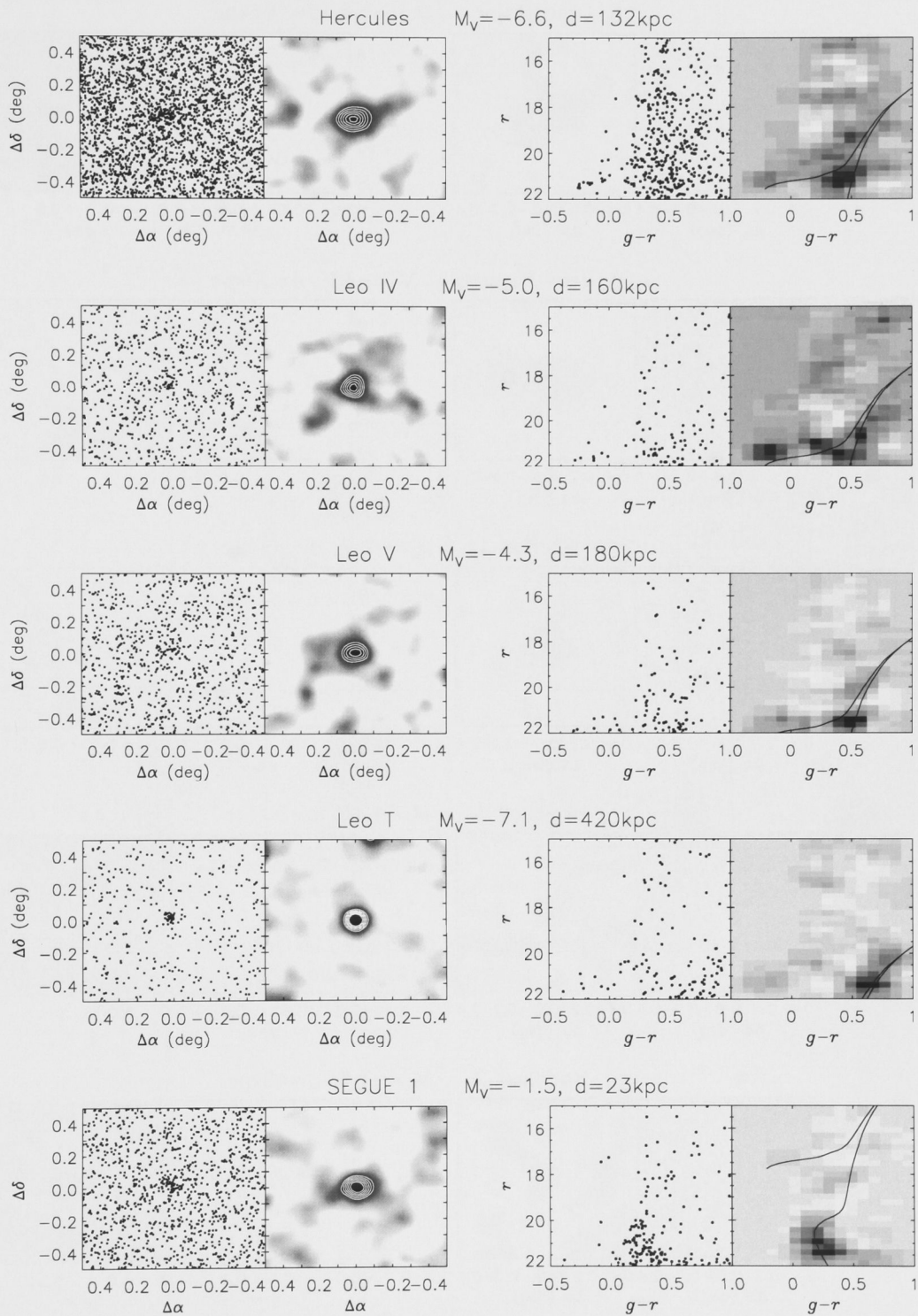


Fig. 2.7 — Detections of recently discovered MW satellites *cont.*

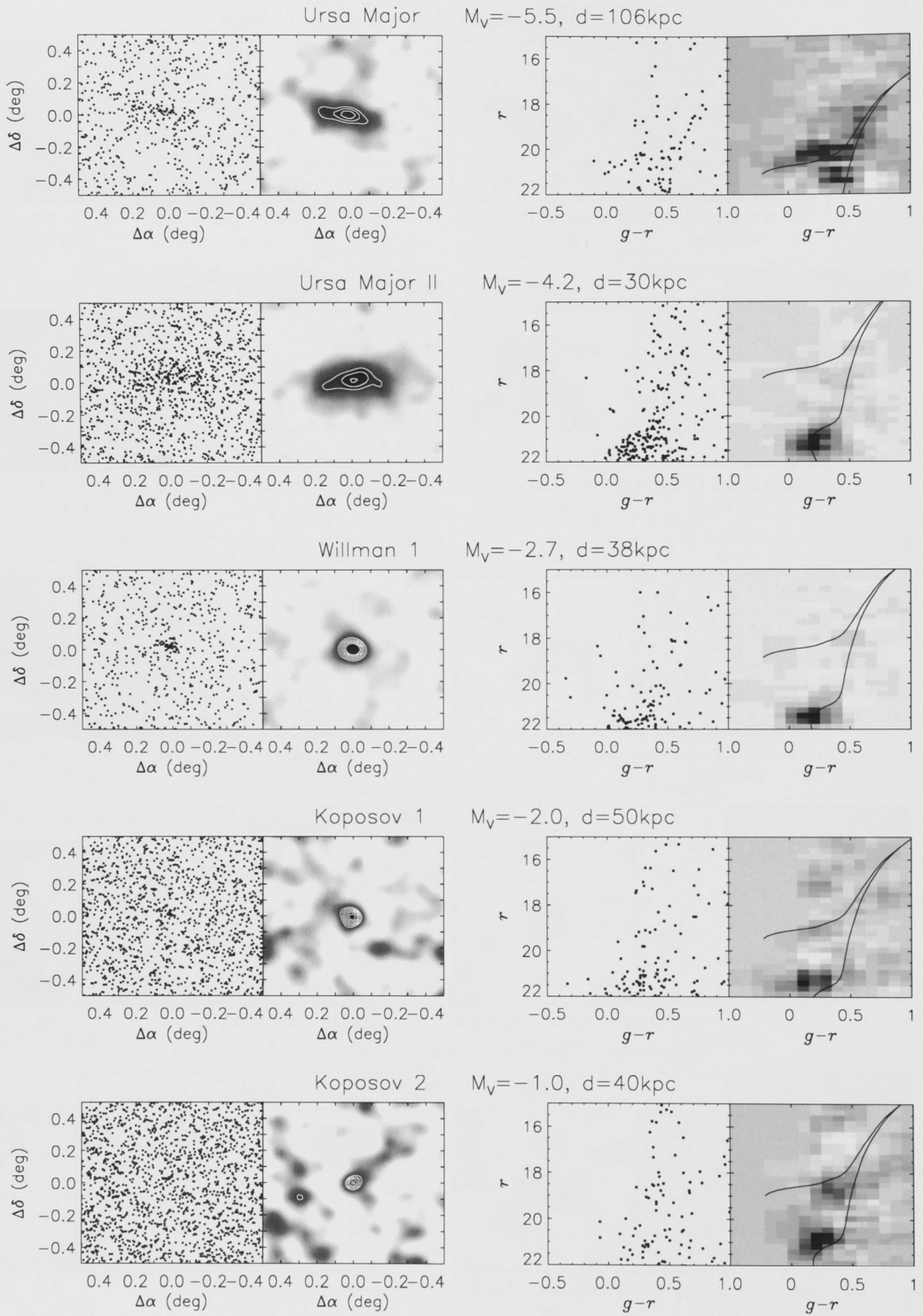


Fig. 2.8 — Detections of recently discovered MW satellites *cont.*

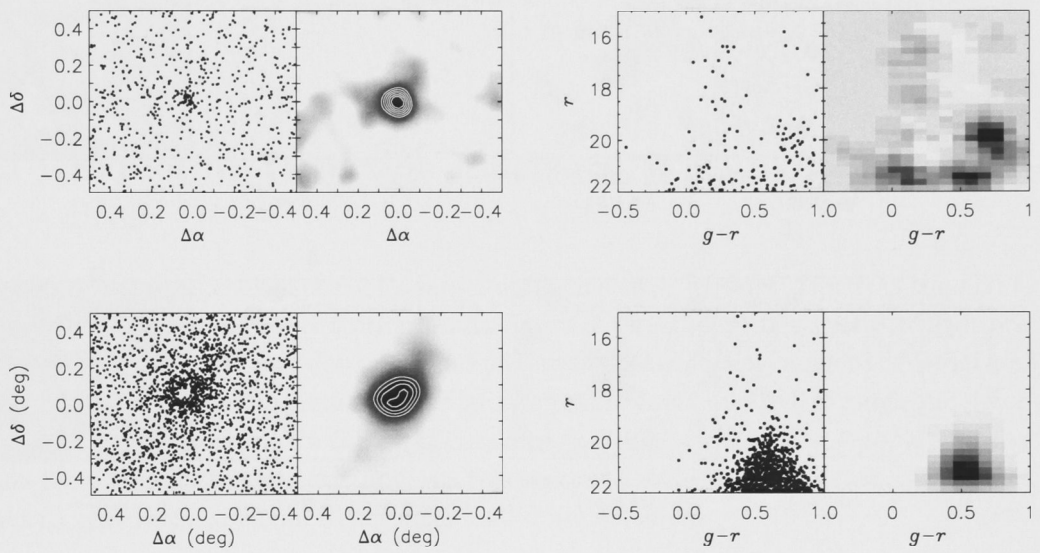


Fig. 2.9 — Detections of Abell 1413 (top) and NGC 4486 (bottom) as examples of galaxy cluster and background galaxy detections.

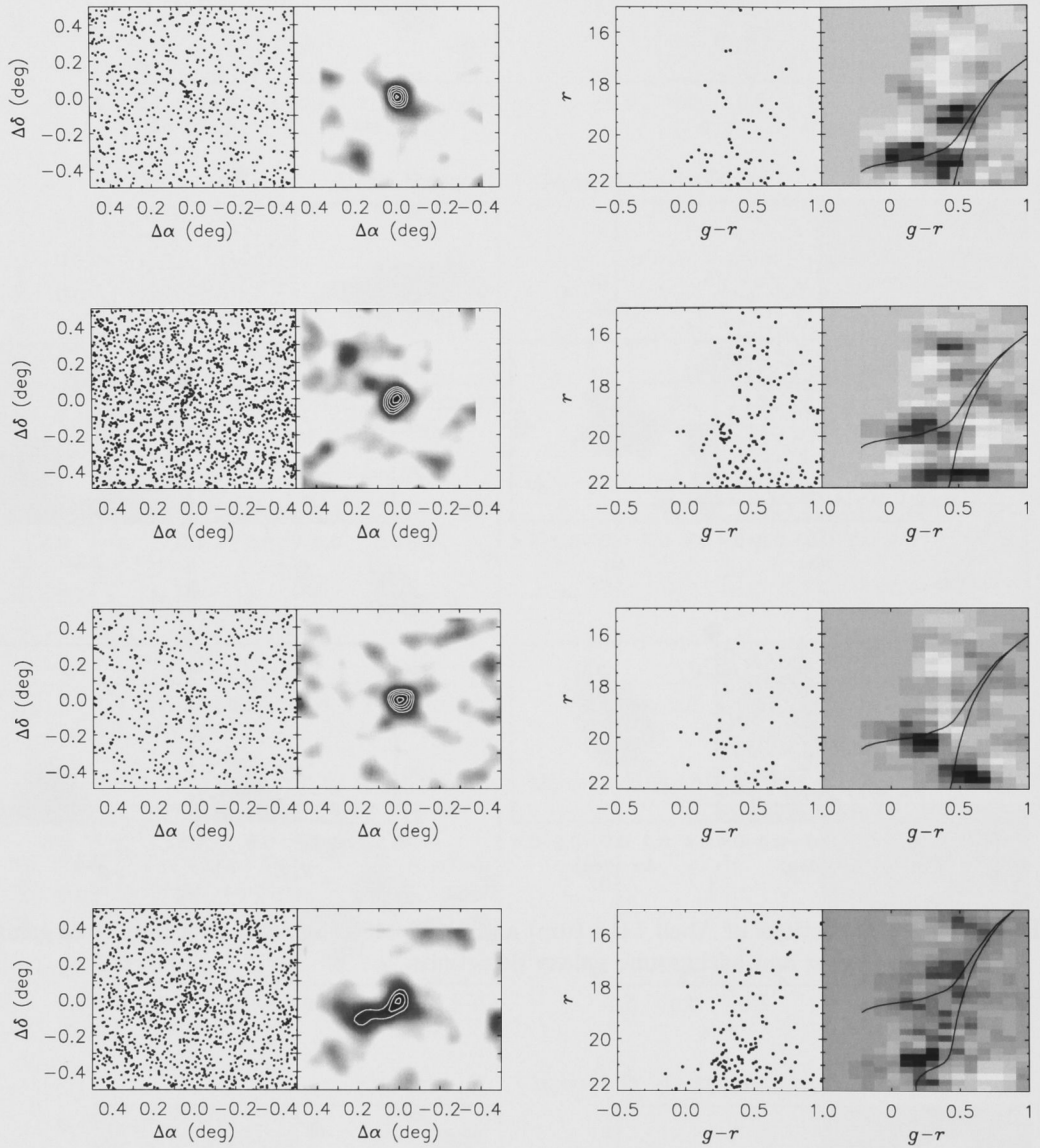


Fig. 2.10 — The four unknown detections with detection strength equal to or greater than known satellites (except Leo V). From top to bottom: Canes Venatici W, Hercules X, Ursa Major Y and Virgo Z. Isochrones show the distance interval at which these overdensities produced the strongest detections.

Chapter 3

Simulations

Please excuse the crudity of this model, I didn't have time to build it to scale or to paint it.

–Emmett Brown

3.1 Exploring Detection Efficiency With Synthetic Satellites

The most advantageous aspect of a large, uniform search for MW dwarfs is the ability to rigorously calculate its detection limits in order to compare observations with predictions. To calculate the detection completeness of our search, artificially generated galaxies are embedded in simulated stellar foreground fields and put through the detection algorithm to investigate the sensitivity as a function of galaxy distance, luminosity, scale length, and Galactic latitude. In this section, we describe in detail the method used to synthesize artificial SDSS fields and dSph satellites.

3.1.1 Sowing the Simulated Fields

When simulating fields in which to embed artificial galaxies, our goal is to create a large number of fields with the same point-source color, magnitude, and density distributions as observed in the SDSS DR6 footprint. The detectability of a dSph may change depending on its position in the sky. For example, those at low Galactic latitudes will be harder to detect than those at high latitudes, owing to the greater number of foreground stars. The relative proportions of the thin disk, thick disk, and stellar halo will also vary with latitude and longitude, changing what fraction of foreground stars will be included in the color–magnitude selection described in Section 2.3.

To conduct a controlled experiment to see how Galactic foreground affects detection efficiency over the DR6 footprint, we first select three fiducial latitudes to simulate: the median latitude of the DR6 footprint, and the latitudes above and below which 10% of the survey lies. Figure 3.1 shows the fraction of sky observed by SDSS DR6 as a function of latitude (dashed line). Weighting this fraction by $\cos b$ gives the relative area

on the celestial sphere that each observed latitude occupies (solid gray line), showing that the majority of the DR6 footprint by area is located between $b \approx 45^\circ$ and $b \approx 65^\circ$. The cumulative total (solid black line) allows us to choose the latitudes corresponding to 10%, 50%, and 90% levels of DR6, namely 31° , 53° , and 73° , respectively. These are the three values of latitude that we implement in our simulations.

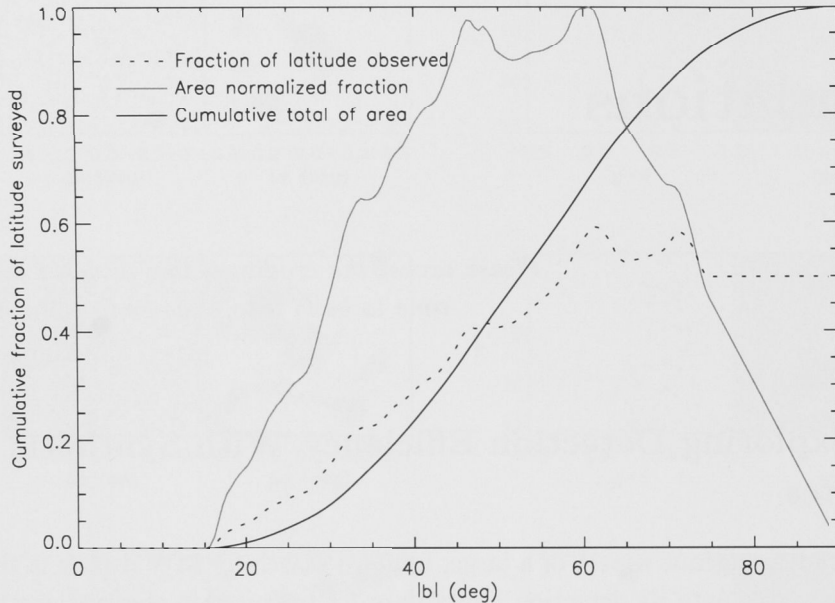


Fig. 3.1 — The fraction of sky as observed by SDSS DR6 at each latitude. The dotted line shows what fraction of the small circle on the celestial sphere traced by each latitude has been surveyed, and the gray line is this fraction weighted by the cosine of latitude, to give a relative sky area observed at each latitude. The largest area of DR6 observations occur at $b \simeq 60^\circ$. The solid black line is the cumulative total of the gray line.

Now that we have chosen what latitudes to simulate, we need to relate these to the stellar foreground density. Figure 3.2 presents a 2D histogram of latitude and foreground density, considering only stars brighter than $r = 22.0$ and bluer than $g - r = 1.0$. This figure shows a span in foreground levels at each latitude. The solid black line traces the median and our chosen latitudes are marked along the x -axis. For each of our latitudes, we take a slice through the 2D histogram and use this distribution of densities to randomly assign a density for each of our simulated fields. Each artificial star in our simulated fields is assigned photometric parameters from a star in DR6, chosen at random from all stars within ± 0.5 of the latitude in question. These stars are then randomly distributed in a $3^\circ \times 3^\circ$ field. Although the true distribution of point sources in the SDSS is certainly not random, this approach allows us to perform a well-controlled experiment to derive the detectability of dwarfs in the limit of a purely random point-source distribution, using many realizations of the data and of simulated galaxies. Willman (2003) showed that using real SDSS data rather than randomized

realizations of SDSS data to derive the detectability of dwarfs results in detection limits that are more conservative by 0.0–0.3 mag than those derived from randomized fields, for the 4.5 smoothing filter used in this paper. We may thus overestimate the detectability of dwarfs by a couple tenths of a dex in magnitude.

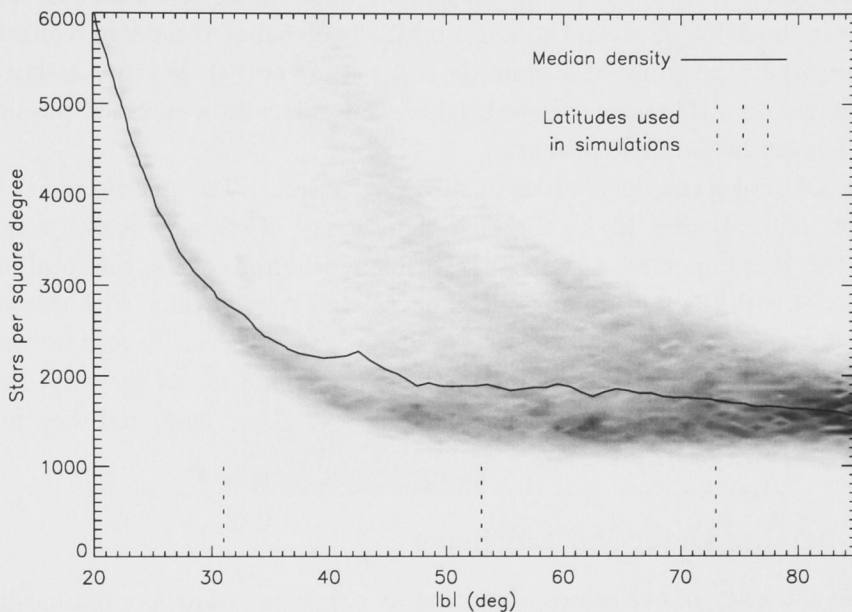


Fig. 3.2 — Gray-scale plot of the number of sources per deg^2 satisfying $r < 22.0$ and $g - r < 1.0$ vs. absolute Galactic latitude. The black line traces the median density at each latitude. The three latitudes we choose to simulate are marked along the x -axis.

3.1.2 Forging Virtual Dwarfs

To simulate a dSph galaxy CMD, we enlist *Hubble Space Telescope* (*HST*) observations of three MW satellites¹: Carina, Draco, and Ursa Minor (Holtzman et al., 2006). Figure 3.3 shows the combined CMD of these objects. We take this M_V and $V - I$ CMD and translate it in color and magnitude loosely to match the Girardi et al. (2004) isochrones in g and r . The reasonable agreement between the *HST* data after approximate transformation and Girardi et al. (2004) isochrones in g and r is sufficient to allow the use of *HST* data for our simulated objects.

We use these data to create a composite old stellar population catalog of stars brighter than $M_r = 6$ by combining sources from the three *HST* dwarfs. Carina, Draco, and Ursa Minor each contribute 5,548, 4,487, and 3,296 stars, respectively. Each time we simulate a dwarf galaxy of x stars, we select those x stars at random from this composite catalog. The luminosity is calculated from the integrated flux from

¹<http://astronomy.nmsu.edu/holtz/archival/html/lg.html>

all stars, and a correction added to account for stars below an absolute magnitude of $M_r = 6$. The cumulative luminosity functions in the right panel of Figure 3.3 show that typically $\sim 10\%$ of the total flux originates from stars below this cutoff. We then adjust the photometry of the stars to the correct distance modulus and add photometric scatter to reflect increasing measurement uncertainty with fainter magnitudes. We do this by finding the best fit for the 1σ magnitude uncertainty as a function of g and r magnitude in the SDSS data, and adding a normally distributed random realization δ of this value $\sigma(m)$ for the adjusted magnitude, $m_{\text{star}} = m + \delta\sigma(m)$. We then assign random positions based on a Plummer surface brightness profile with a specified physical scale length at a given heliocentric distance.

Figure 3.4 shows examples of three simulated dSphs. The middle panel shows a system not unlike Boötes II, highlighting the paucity of stars in the objects we are searching for. It is important to note that at these low luminosities, the total luminosities of galaxies with the same number of stars can vary dramatically, with this variation increasing for galaxies with fewer stars. A single RGB star can have a magnitude of $M_r = -3$ which is well in the regime of the total magnitude of recently discovered satellites. Each generated galaxy is embedded in a simulated field, and then processed as described in Sections 2.3.2–2.3.4.

3.1.3 Charting Detection Efficiency

To test the efficiency of our search algorithm as a function of galaxy luminosity, scale length, distance, and Galactic latitude, we generate a total of 3,825,000 galaxies spanning ranges in Galactic latitude, luminosity, physical size, and distance. We simulate systems at latitudes of 31° , 53° and 73° and with $2^x \times 100$ stars brighter than $M_V = 6$, where x is an integer between 0 and 11 (giving a range of 100–204,800 stars). These stellar totals correspond to mean total magnitudes of $M_V = -1.5, -2.3, -3.1, -3.9, -4.7, -5.5, -6.2, -7.0, -7.7, -8.5, -9.2$ and -10.0 . For each of the 36 combinations of latitude and magnitude, we simulate a large number of galaxies with distances and physical scale lengths randomly generated with the limits $1.3 < \log d/\text{kpc} < 3.0$ and $0.9 < \log r_h/\text{pc} < 3.0$. For the brightest and faintest systems we tailor these ranges to avoid redundant iterations; there is little to be gained by simulating an $M_V = -1.5$ system at 200 kpc, or an $M_V = -10.0$ system at 20 kpc. Hence, the total number of simulations for each magnitude/latitude combination varies, but is chosen such that there are typically 500 simulations in each $0.1 \log(d) \times 0.1 \log(r_h)$ bin of Figure 3.5.

3.2 Dissecting Efficiency Trends

Figure 3.5 shows the detection efficiency of simulated dwarf galaxies as a function of luminosity, scale length, and distance at the median SDSS Galactic latitude (53°). Each of the MW satellites detected in SDSS are overplotted, not including Koposov 1 and 2. Each panel contains a gray-scale map of the detection efficiency for simulated galaxies of the mean absolute magnitude specified in the panel. Because the total magnitude

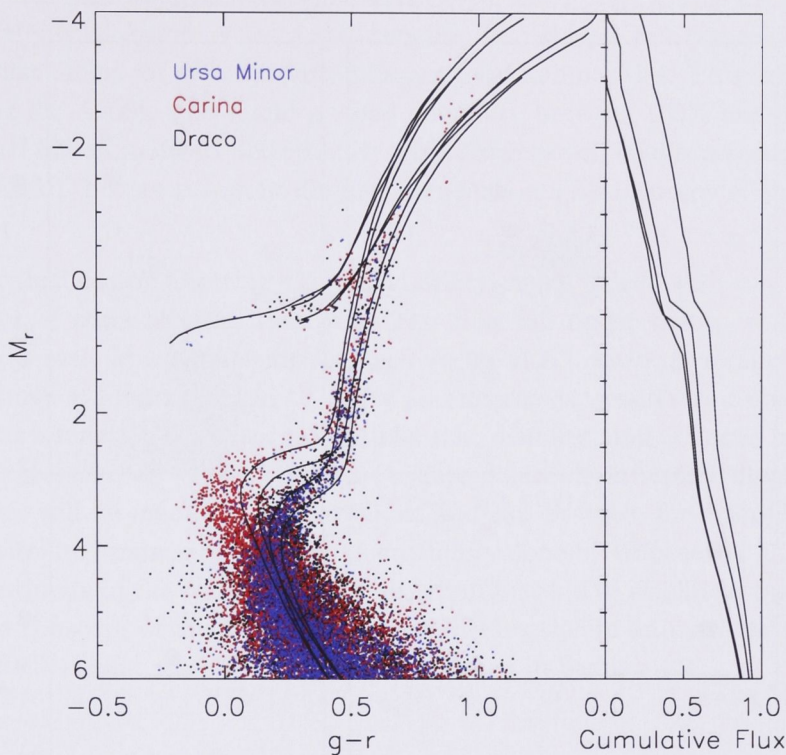


Fig. 3.3 — *HST* data of three MW satellite dSphs (Carina: red, Draco: black, and Ursa Minor: blue; Holtzman et al., 2006) with SDSS isochrones (Girardi et al., 2004) overlaid. The right panel shows the cumulative luminosity functions for the corresponding isochrones, using the four combinations of $[\text{Fe}/\text{H}] = -2.27, -1.5$ and age = 8, 14 Gyr. Data are corrected for distance and presented in absolute magnitude.

varies for systems with a constant number of stars, we quote both the mean magnitude and the standard deviation of magnitudes for each panel. White shows regions of 100% efficiency, while black shows 0%. The four contours, moving outward from 100% efficiency, show the 90%, 84.13%, 50%, and 15.86% levels. The 84.13% and 15.86% levels were chosen to illustrate the $\pm 1\sigma$ in detectability as a function of distance and size.

The greater the number of stars in a simulated galaxy, the less its absolute magnitude will vary between realizations, so the standard deviation in the integrated magnitudes of simulated galaxies contributing to each panel decreases with increasing luminosity. The $M_V = -7.7$ panel which shows a small increase in standard deviation marks a change in the way the galaxies are simulated; we are now simulating systems with more stars than are in our *HST* catalog so the simulated stars no longer have unique photometry drawn from this catalog. This amplifies the small number effect of single stars on the total magnitude for simulated galaxies with $M_V = -7.7$ and brighter.

Figure 3.5 illustrates the necessity for a large number of simulations as there are

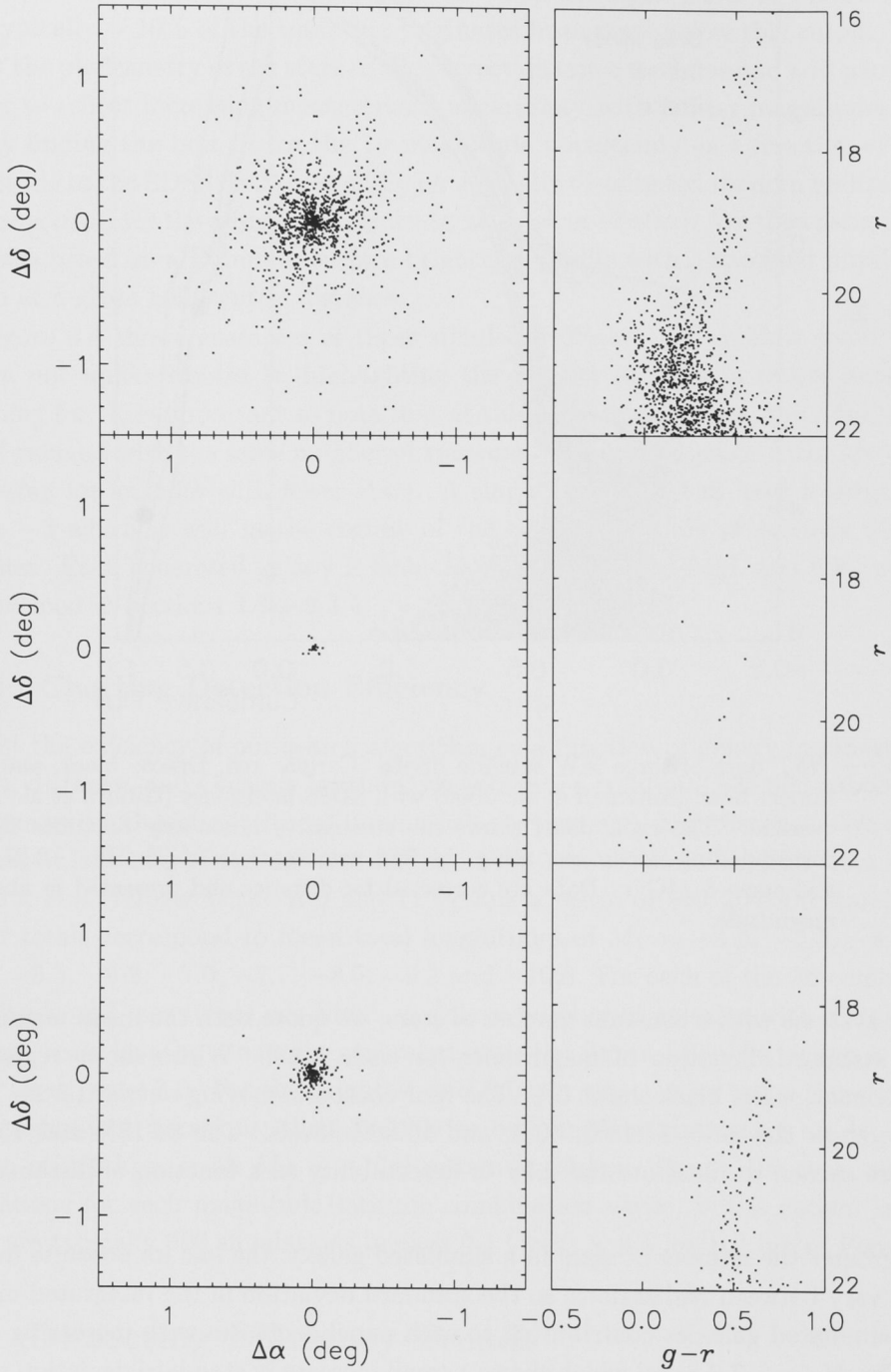


Fig. 3.4 — Simulated dSph systems. *Top:* $d = 25$ kpc, $r_h = 250$ pc, $M_V = -4.7$. *Middle:* $d = 45$ kpc, $r_h = 40$ pc, $M_V = -2.3$. *Bottom:* $d = 100$ kpc, $r_h = 250$ pc, $M_V = -5.6$.

subtle features that would otherwise be unresolved. For example, this figure shows that the detectability of dwarfs is not a step function in distance, but rather slowly falls off at a rate that differs for systems with different total luminosities. This is in contrast to Koposov et al. (2008), who found a steep boundary between 100% and 0% efficiency. The gradual fall-off in dwarf detectability with distance will be discussed in more detail in Section 3.2.1, but we postpone detailed comparison with Koposov et al. (2008) until Section 4.1.

The critical factor affecting the detectability of an object with our algorithm is the number of stars brighter than $r = 22.0$ that fall under the $r_h = 4.5$ Plummer smoothing kernel. In the following sections, we use this to gain physical understanding of the features of Figure 3.5 and to derive an analytic expression to describe detection efficiency as a function of galaxy magnitude, size, distance, and Galactic latitude. This analytic expression, as well as a routine to interpolate detectability directly from the simulations, will be made publicly available and can be used, for example, to correct the MW satellite luminosity function as previously done by Koposov et al. (2008) or to make an estimate of the corrected radial distribution of MW satellites. Such endeavors are beyond the scope of this paper, but we use the function to estimate the total number of MW satellites that remain undetected, presented in Section 4.2.

3.2.1 Efficiency Versus Distance

Figure 3.5 shows that the detectability of resolved dwarfs around the MW is not a step function in distance. As distance to a dwarf galaxy increases, the number of stars brighter than $r = 22.0$ ($N_{r<22}$) decreases. In an idealized scenario, the detectability of that dwarf would drop from 100% to 0% at a distance beyond which the number of resolved stars required to produce a detection is larger than $N_{r<22}$. As we have discussed in previous sections, random variations in the stellar luminosity function can be substantial in the faintest systems, hence $N_{r<22}$ will be affected by stochastic fluctuations. Moreover, the wide range in foreground densities at a given Galactic latitude (see Figure 3.2) impacts the detectability of two identical dwarfs. Therefore the transition from 1.0 to 0.0 detection efficiency is not expected to be a step function, but rather described by a Gaussian integral. Koposov et al. (2008) also modeled the detectability transition with a Gaussian integral, despite finding a steep decline. So detection efficiency (DE) as a function of $\log(\text{distance}/\text{kpc})$, which for brevity we denote ${}_L d$ can be described as

$$DE({}_L d) = \text{erf} \left(\frac{{}_L \bar{d} - {}_L d}{\sigma_{{}_L d}} \right)$$

where ${}_L d$ is the logarithm of distance, and ${}_L \bar{d}$ and $\sigma_{{}_L d}$ are the mean and standard deviation of $\log(\text{distance})$, respectively. The mean corresponds to the distance at which

a system would be detected with 50% efficiency. The error function erf is defined as:

$$erf(x) = \frac{2}{\sqrt{\pi}} \int_0^x e^{-t^2} dt.$$

Examination of Figure 3.5 shows that σ_{Ld} (how quickly efficiency transitions from unity to zero) changes depending on luminosity. We would naively expect σ_{Ld} to continue increasing with decreasing brightness as small number statistics becomes more dominant. Instead it shows a maximum at $M_V \approx -3.9$ before decreasing. This is a result of the stochastic fluctuations and the derivative of the luminosity function; since $N_{r<22}$ varies for systems with the same total number of stars, the individual distance that each of these systems could be detected at also varies. As the number of stars above the brightness limit is dependent on the LF, the slope of the LF determines how $N_{r<22}$ changes with distance. Hence σ_{Ld} is smaller for the faintest objects when the MSTO is required for a detection because the LF is at its steepest at the turnoff.

3.2.2 Efficiency Versus Scale-length

The fraction of a dwarf's stars within our 4'.5 spatial smoothing kernel decreases with increasing physical scale length and/or decreasing distance. A system of some luminosity and distance that is detectable when its angular size is $\lesssim 4'.5$ may thus be undetectable if those same stars are spread over a larger angular scale. As the concentration of stars increases we would expect detection efficiency to also increase. However, when the angular size of a dwarf is comparable with the smoothing kernel size, the detectability does not appreciably improve with further decrease in size since the number of stars within the kernel is not significantly changing. Hence objects of this angular size or smaller will be detected with the same efficiency.

Once the angular size becomes larger than the kernel size, the number of stars within the kernel declines. The relationship between size and detection distance is dependent on the stellar luminosity function of the system. Take for example an object with an angular size larger than the smoothing kernel, detected with 50% efficiency at some distance. To keep the object at 50% efficiency as we continue to increase the physical size, the drop in efficiency can be counteracted by decreasing the object's distance. As this object is moved closer the number of stars above $r = 22.0$ increases at a rate corresponding to the LF. At the distance when the MSTO becomes brighter than $r = 22.0$ (~ 65 kpc), the rapid increase in the number of stars corresponds to a sudden improvement in detection efficiency, evident in Figure 3.5 at $\log(d) \approx 1.8$ in the $M_V = -5.5$, -4.7 and -3.9 panels. As with distance, efficiency versus scale length can be modeled by a Gaussian integral, but with the mean and standard deviations as functions of distance; so

$$DE(Lr_h) = erf\left(\frac{\bar{L}r_h(\bar{L}d) - Lr_h}{\sigma_{Lr_h}(Ld)}\right).$$

3.2.3 Analytically Expressing Detection Efficiency

Combining the previous two results, we can analytically describe detectability with a Gaussian integral over $\log d$ multiplied by another Gaussian integral over $\log r_h$. To introduce magnitude M_V and latitude b , we set the means ($\bar{L}d$, $\bar{L}r_h$) and standard deviations (σ_{Ld} , σ_{Lr_h}) in the integrals to be functions of M_V and b . Therefore the detection efficiency DE can be expressed as

$$DE = \text{erf} \left(\frac{\bar{L}d(M_V, b) - L d}{\sigma_{Ld}(M_V, b)} \right) \times \text{erf} \left(\frac{\bar{L}r_h(\bar{L}d(M_V, b)) - L r_h}{\sigma_{Lr_h}(Ld(M_V, b))} \right)$$

The means and standard deviations can be found by fitting Gaussian integrals along the distance and scale length axes of the panels in Figure 3.5. The main source of uncertainty in this expression is the galaxy luminosity, which while correlated with the number of stars, can vary by over a magnitude for systems of equal detectability. The function does however give a good statistical approximation from which to estimate the properties of the true MW satellite population. In Figure 3.6 we compare the $M_V = -3.9$ panel of Figure 3.5 with the analytical function. There is good agreement between the empirical and analytical detection efficiencies with a 1σ deviation of only $\sim 8.7\%$ across the entire range of parameters. For reference the size of the 4.5 smoothing kernel and the distance at which the MSTO becomes resolved are shown in the center panel in red and blue respectively.

The analytical efficiency is compared in Table 3.1 with the interpolated efficiency from the grids in Figure 3.5 for real MW dwarfs. For all objects besides Boötes II, Leo V, and Leo T, the difference is within $\sim 1\%$. At first inspection, it may seem odd that all objects have a very high, almost 100%, efficiency, but given that most of the parameter space probed by our simulations yields either zero or unity efficiency, it is not unexpected that the handful of objects detected in this vast volume are detected with high efficiency.

3.2.4 Efficiency Versus Latitude

Unlike the other parameters which vary a dSph's signal strength, Galactic latitude affects detection efficiency by changing the foreground density, and therefore noise above which we must detect a signal. If latitude plays a significant role in the detectability of dwarfs, then it must be taken into account when making any corrections to the MW satellite census. Figure 3.7 shows the $M_V \approx -3.9$ panel of Figure 3.5 ($b = 53^\circ$) with the addition of the 50% detection efficiency (dashed) and 90% detection efficiency (dotted) contours of the $b = 31^\circ$ (orange) and 73° (blue) simulations overplotted. As expected, an object of given size and luminosity will not be detectable as far away at low latitudes as it would be closer to the Galactic pole. For example, an object with $r_h \approx 30$ pc and $M_V \approx -3.9$ at $b = 73^\circ$ can be detected with 90% efficiency as far as ~ 120 kpc, while the same object at $b = 31^\circ$ has a 90% efficiency at ~ 95 kpc.

To anticipate the effect that varying Galactic foreground will affect future dwarf

Table 3.1. Comparison of Interpolated and Analytical Detection Efficiencies

Object	Interp.	Analyt.	Diff.
Boo	99.84	99.98	-0.14
Boo II	90.39	95.96	-5.57
CVn	100.0	100.0	0.0
CVn II	98.26	99.07	-0.81
Com	99.71	100.0	-0.29
Dra	100.0	100.0	0.0
Her	99.82	99.83	-0.01
Leo	100.0	100.0	0.0
Leo II	100.0	100.0	0.0
Leo A	100.0	100.0	0.0
Leo IV	98.65	99.77	-1.12
Leo V	83.56	91.27	-7.71
Leo T	93.41	99.38	-5.97
Segue 1	100.0	100.0	0.0
Sex	100.0	100.0	0.0
UMa	99.97	99.86	0.11
UMa II	100.0	99.96	0.04
Will 1	98.56	99.30	-0.74

searches in data that go closer to the Galactic plane than SDSS, we also repeat the simulation of $M_V \approx -3.9$ galaxies at a foreground density of 10,000 stars per deg^2 , approximating a latitude of $\sim 15^\circ$. The 50% and 90% detection efficiency contours (red) for these simulations are also shown in Figure 3.7. This further reduces the 90% detection distance of our example object to ~ 80 kpc but demonstrates that future surveys should still detect dwarfs at relatively low Galactic latitudes, barring extinction effects.

To check that latitude has the same lack of effect over different magnitudes, we calculate the 50%, 90%, and 99% detection efficiency distances for a $r_h = 100$ pc object over the magnitude range $-1.5 > M_V > -7.0$ at $b = 31^\circ, 53^\circ, \text{ and } 73^\circ$ (Figure 3.8, note that in this figure the distance scale is linear). The 53° and 73° curves are indistinguishable and the $b = 31^\circ$ curve is typically less than ~ 20 kpc lower. This demonstrates that over the DR6 footprint, latitude does not play an important role on average in the detectability of objects. However, if we are unlucky, then individual objects could by chance lie in the directions of unusually high foreground counts.

3.2.5 Comparing R_{99} , R_{90} and R_{50}

We use the analytical expression derived in Section 3.2.3 to estimate the distance at which each of the MW dwarfs would be detected with 50% efficiency, R_{50} (Figure 3.9, gray dots). Because R_{50} depends on r_h , as well as luminosity, we also for reference show R_{50} for objects with $r_h = 250$ pc (red) and $r_h = 50$ pc (blue). These lines show that the detectability of the lowest luminosity dwarfs is severely reduced for large scale sizes. Objects with Segue 1-, Boötes II-, or Willman 1-like luminosities would not have been detectable with scale sizes of 100 pc or larger, even at very nearby distances. This size bias is important to bear in mind, particularly given that the three M31 satellites discovered by McConnachie et al. (2008) highlight regions of dwarf galaxy parameter space that have not previously been observed.

Assuming the size–luminosity distribution of known satellites is representative of all satellites we can ignore size and approximate R_{50} as a function of M_V by linear fit to the R_{50} of actual dwarfs:

$$\log R_{50} = -0.187M_V + 1.420.$$

For comparison, the Koposov et al. (2008) equivalent of R_{50} is shown in Figure 3.9 (dotted line) obtained from Table 3 in their paper, and discussed further in Section 4.1. For reference, the actual distances to the MW dwarfs are shown as black dots.

A more useful quantity might be $R_{complete}$, the maximum distance at which objects can be detected. Although we choose to use “complete” to refer to 90% detectability, complete could be defined as, say 90% or 99% efficiency. This can also be approximated by a linear fit to the results for the actual MW dwarfs:

$$\log R_{90} = -0.204M_V + 1.164$$

or

$$\log R_{99} = -0.217M_V + 1.005.$$

These relationships again assume that the known satellites are typical of the MW satellite population as a whole, i.e., objects with luminosities comparable with Segue 1 are similar in size to Segue 1 and not significantly larger.

Returning to Figure 3.8 we see the distance range over which detectability changes from 99% to 50%. R_{90} is typically ~ 20 kpc closer than R_{50} , and R_{99} is ~ 20 kpc closer still. From this figure we can also see that objects brighter than $M_V \approx -6.5$ ($M_V \approx -5.9$) are detected with 99% (90%) efficiency out to 300 kpc. We can infer from this that all dwarfs within the MW virial radius brighter than $M_V \approx -6.5$ are known, and any satellites still undetected are likely to be comparable with objects such as Coma Berenices, Boötes II, or Segue 1, at distances greater than ~ 40 kpc. An ultra-faint satellite such as Segue 1 can only be detected with 50% efficiency out to ~ 40 kpc; there may be many more such objects beyond this distance.

The code for interpolating detection efficiency from our simulations as well as the analytical function will be made available for download at the *Astronomical Journal* Web site. Interpolation will give more accurate results, but the analytical function will provide flexibility for customization to suit individual needs and implementation of any future improvements.

3.2.6 Caveats

An underlying assumption of our simulations is that the DR6 point-source catalog is consistently 100% complete to $r = 22.0$. This assumption may result in optimistic detection efficiency estimates for the faintest and furthest systems. These faintest and more distant systems would also be subject to the human element; a real object may be detected by the algorithm but on visual inspection be disregarded as background galaxy cluster or other contaminant. Finally, sources in our simulated dSphs are distributed circularly symmetrically. Martin et al. (2008) find that the ultra-faint satellites are in fact quite elliptical, which due to our circular Plummer smoothing kernel, possibly results in overestimated efficiencies for objects such as Hercules, UMa and UMa II with ellipticities of 0.68, 0.80, and 0.63, respectively.

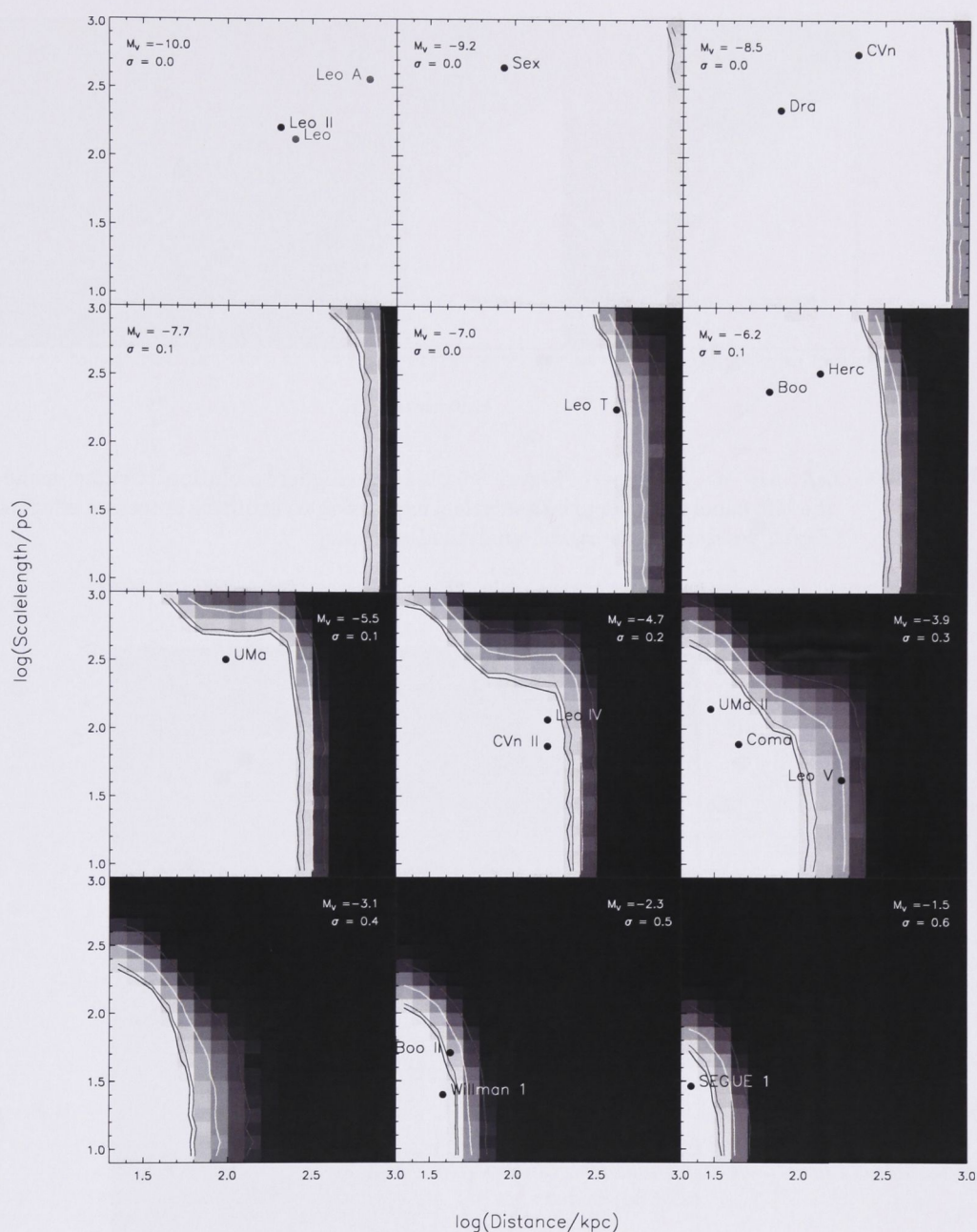


Fig. 3.5 — Detection efficiency for specific galaxy parameters. Each panel shows the detection efficiency as a function of distance and scale length for a particular number of galaxy stars. The average total absolute magnitude for each of these sets of galaxies is shown along with the standard deviation in magnitudes. Contours show the 90%, 84.13%, 50%, and 15.86% levels. Sizes and distances of known MW dSphs are shown in the best-matching magnitude panel. Leo and Leo A are shown in gray as they are significantly brighter than $M_V = -10.0$. Values for newly discovered objects plus Draco are taken from Martin et al. (2008) except for Leo V (Belokurov et al., 2008). Values for Leo, Leo II, Leo A, and Sextans are taken from Mateo (1998).

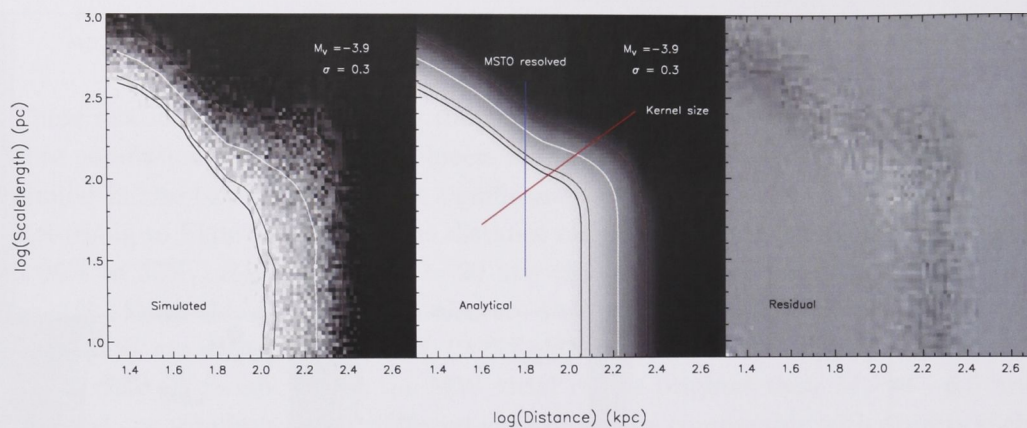


Fig. 3.6 — *Left*: $M_V = -3.9$ panel of Figure 3.5 binned to higher resolution. *Center*: same as the left panel but using the analytical expression to estimate detection efficiency. *Right*: residual of the model-analytical efficiency.

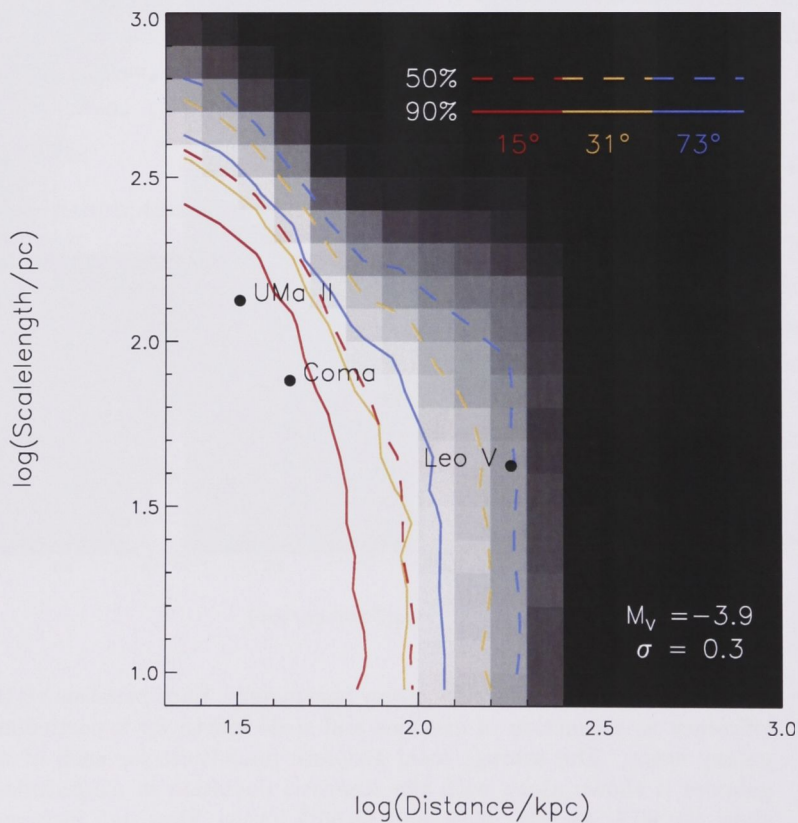


Fig. 3.7 — The same as the $M_V = -3.9$ panel of Figure 3.5, but showing the 50% and 90% contours of the simulations at $b = 73^\circ$ (blue), 31° (orange), and $\sim 15^\circ$ (red).

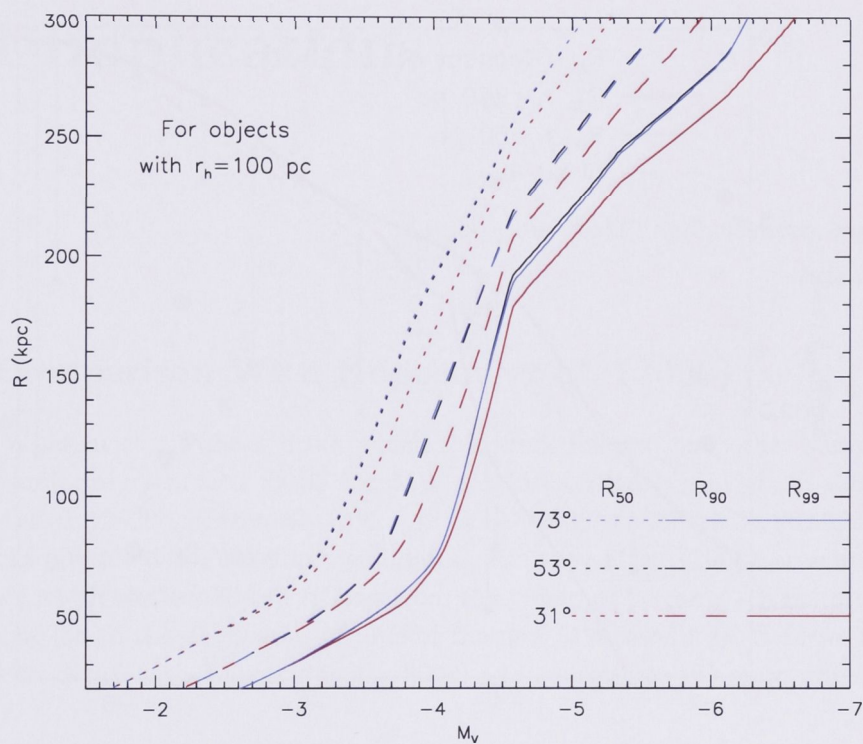


Fig. 3.8 — 50%, 90%, and 99% completeness distances for a $r_h = 100$ pc object as a function of magnitude at three Galactic latitudes: 31° , 53° and 73° . The 53° and 73° curves are virtually indistinguishable showing that latitude does not significantly impact satellite detection over latitude ranges of DR6.

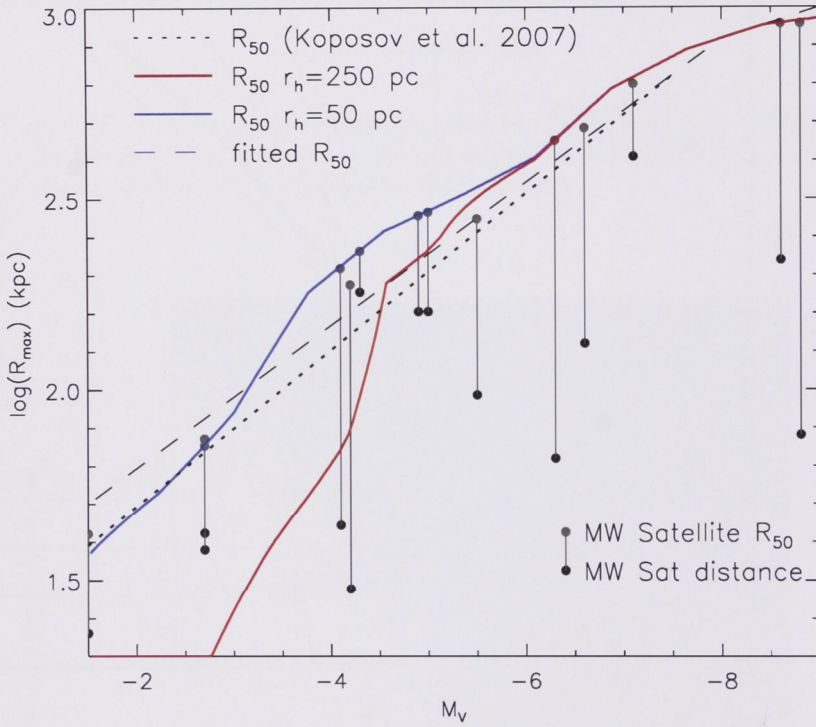


Fig. 3.9 — Comparison of the 50% detection distance as a function of magnitude for K08 (dotted) and for our analytical efficiency using $r_h = 250$ pc (red) and $r_h = 50$ pc (blue). MW dwarfs are shown as filled circles.

Chapter 4

Survey Punchline: Discussion and Implications

I reject your reality and substitute my own.

–Adam Savage

4.1 Comparison With Koposov et al. (2008)

Besides Willman et al. (2002) from which this work follows, two other surveys have recently uniformly searched SDSS for MW satellites, namely Liu et al. (2008) and Koposov et al. (2008), henceforth K08. Liu et al. (2008) conducted a straightforward search and presented five satellite candidates. Koposov et al. (2008) present a study comparable with this work, and follows from the “Field of Streams” (Belokurov et al., 2006a) that led to the discoveries of nine of the new MW satellites. Here we compare our work in detail with Koposov et al. (2008) and summarize the main differences in Table 4.1.

The aim of Koposov et al. (2008) was to present a luminosity function of the MW satellites corrected for a luminosity bias. Their analysis discovered two new extremely faint globular clusters, Koposov 1 and 2 (Koposov et al., 2007). In principle, our analysis is quite similar to Koposov et al. (2008) in that they apply a color cut, smooth the stellar counts and look for statistically significant overdensities. There are several distinctions however that we detail below.

K08 employed a $g - r < 1.2$ color cut to remove a substantial fraction of MW foreground stars and a $r < 22.5$ cut to limit the influence of background galaxies and increasing uncertainties/incompleteness. Our color–magnitude cuts are tailored to old stellar populations at 16 different distances which serve to eliminate more foreground stars than the looser K08 cut. The looser K08 cut leaves enough stars that a complicated set of detection thresholds is unnecessary, whereas we must consider the effects of non-Gaussianity in low densities (see Section 2.3.4). K08 deals with background galaxy clusters, a major source of contaminant overdensities, by producing a galaxy clustering

significance in the same manner as the stellar clustering; anywhere that a stellar overdensity occurs without a corresponding galaxy overdensity is much more likely to be a true stellar overdensity. Our algorithm only includes stars as faint as $r = 22.0$ and as such we have fewer galaxy cluster contaminant detections.

The most substantial difference between our work and K08 is how we derive the detection limits of our algorithms. Like our work, K08 simulated artificial galaxies to explore the detection efficiency as a function of size, distance and luminosity. K08 simulated 8000 galaxies over a similar range of parameters as our study, but with only \sim eight objects per $0.3 \log(d) \times 0.3 \log(r_h) \times 0.8$ mag bin. There is considerable noise evident in the detection limits (their Figure 6), and all of the new satellites appear to lie on the edge of detectability. K08 observed a steep, but finite, transition from unity to zero detection efficiency which they attributed to the large range of distances that fall within each size–luminosity bin. However, as discussed in our §3.1.2, a large number of simulated galaxies is essential for each permutation of dwarf galaxy parameters to effectively map their detectability. Our high-resolution detection maps (~ 500 objects per $0.1 \log(d) \times 0.1 \log(r_h) \times 0.8$ mag bin, $\times 3$ latitudes) show that the detectability of a dwarf drops off slowly with size and distance, and that only Leo T, Leo IV, Leo V, Boötes II and Willman 1 lie close to the edge of detectability. The difference between 90% and 10% efficiency typically occurs over 0.2 dex in distance (kpc) and 0.3 dex in size (pc; see Figure 3.5).

Both the K08 and our detection limit calculations suffer from the implicit assumptions that the SDSS point-source catalog is complete to the photometry limit and that dwarfs are circularly symmetric. These two assumptions yield detection limits that may be optimistic. The K08 study includes stars to a limiting magnitude of $r = 22.5$, a half-magnitude fainter than our limit of $r = 22.0$. We thus expect that the completeness assumption may impact their calculated limits more than ours.

To directly compare the effectiveness of both algorithms we return to Figure 3.9, showing the distance at which an object is detected with 50% efficiency, R_{50} as a function of magnitude. The dotted line shows the K08 R_{50} which was determined by fitting a limiting magnitude and surface brightness to the seven distance panels in their Figure 10. The gray dots show our R_{50} derived from the analytical efficiency function for each of the MW dwarfs in DR6, and the dashed line shows the best linear fit to these points. The red and blue curves show R_{50} calculated for objects of $r_h = 250$ pc and $r_h = 50$ pc respectively.

Although this comparison indicates that we have comparable limits, our calculated detection efficiencies of each dwarf are all greater than 90% while Table 2 of K08 lists efficiencies as low as 47% (neglecting Boötes II). While Boötes II is not detected with the standard algorithm of K08, it is a comparatively strong detection in our algorithm. We note that the tabulated K08 efficiencies for the known MW dwarfs appear inconsistent with their fitted R_{50} , which places some dwarfs much closer than R_{50} than their actual efficiencies would indicate. The increased dwarf detectability of our survey is owing to a combination of different techniques and our less stringent detection threshold. We set our thresholds to strictly eliminate truly random false

Table 4.1. Summary of Comparison with Koposov et al. (2008).

	This work	Koposov et al. (2008)
Survey area	DR6 - 9500 deg ²	DR5 - 8000 deg ²
Source cuts	Isochrone template at 16 distance intervals	$g - r < 1.2$ and $r < 22.5$
Smoothing kernel	4'5 Plummer profile	$\sigma = 2', 4', 8' - \sigma = 60'$ Gaussians
Threshold	Multiple, function of foreground density	Fixed, considers background galaxies
Modeled detection limits	<i>HST</i> obs of 3 MW dSphs	M92 locus
Number of simulations	3,825,000	8000 for general simulation + 1000 each for known dwarfs within DR5
Efficiency map bin size ($\log(r_h) \times \log(d) \times M_V$)	$0.1 \times 0.1 \times 0.8$	$0.3 \times 0.3 \times 0.8$
Simulation density (n per $0.3 \times 0.3 \times 0.8$ bin)	~ 4500 ($\times 3$ latitudes)	~ 8

positives expected while still yielding new candidates, and hence have ~ 30 unknown detections above our thresholds. Although upon visual inspection of their CMDs many of these detections appear unlikely to be new dSph satellites, they may also be tidal debris or distant galaxy clusters. However, K08 set their detection thresholds just loose enough to retain all known objects; Uma is their weakest detection and there are only three unknown detections above this threshold.

4.2 The Still Missing Satellites

A substantial driving force of this work is the missing satellite problem, which the discovery of so many new objects in the span of three years has shown is far from being observationally exhausted. There are still large regions of parameter space where objects are undetectable, so there can easily exist more objects within the DR6 coverage that remain hidden. Future surveys such as the Stromlo Missing Satellites (SMS) Survey and Pan-STARRS may be able to detect some of these objects, and we can use our model of detectability to estimate how many there may be.

We use a simplified version of the approach used in Tollerud et al. (2008). We first assume that the radial distribution of dwarf galaxies matches that of all well-resolved subhalos of the Via Lactea simulation (Diemand et al., 2007). Tollerud et al. (2008) discusses this assumption in detail; we realize this may not reflect the true MW dwarf distribution, but our qualitative results are fairly robust to the assumed profile. For each satellite detected in DR6, we then determine R_{90} (or R_{99}), the maximum distance to which a satellite of similar properties would be detected with 90% (99%) efficiency. For each value of R_{90} (R_{99}), we determine from the Via Lactea subhalo radial profile what fraction of satellites should be within this distance, and weight each satellite accordingly.

Using all DM subhalos with more than 1000 particles within $r_{vir} = 289$ kpc, and adopting a MW virial radius of 258 kpc (Klypin et al., 2002), we estimate ~ 13 (~ 24) satellites within the MW virial radius in the DR6 footprint. Twelve of these would be the known objects Boötes, Draco, Canes Venatici I and II, Coma Berenices, Leo I, Leo II, Leo IV, Leo V, Hercules, Ursa Major, and Ursa Major II, leaving one (12) possible missing satellite(s). From our simulations, objects brighter than $M_V = -6.5$ are detectable with $> 99\%$ efficiency out to the virial radius, so we would expect that a relatively small number of the faintest systems are missing. These missing satellites may be amongst our candidates, or be either like Coma Berenices or fainter objects in the outer halo. Whether or not future searches reveal such objects may validate the assumed radial distribution. If we assume an isotropic sky distribution of satellites, ~ 13 (~ 24) objects within DR6 equates to ~ 52 (~ 96) across the whole sky.

If we include the ambiguous objects Segue 1, Willman 1, and Boötes II in the calculation, then the R_{90} (R_{99}) DR6 estimate would be ~ 56 (~ 85) satellites only 15 of which are known, or ~ 224 (~ 340) across the sky. The ambiguity of Segue 1, Willman 1, and Boötes II has considerable effect on the extrapolated MW census, underscoring the need for an understanding of these extremely faint systems.

These estimates assume that the sizes and luminosities of the known satellites in DR6 are representative of the MW satellite population as a whole. Based on our detection limits we cannot make any statements regarding extremely diffuse, low luminosity systems that are undetectable by SDSS. The results also depend on the radial distribution assumed. If we instead assume that the MW’s dwarf population follows the radial distribution of the MW dSphs known prior to 2004, then our R_{90} inferred total number of dwarfs (with size–luminosities similar to those known) within DR6 is 12, or 25 including Segue 1, Willman 1 and Boötes II. This implies that all or most satellites within DR6 would be known.

Tollerud et al. (2008) use the detection limits of Koposov et al. (2008) to similarly estimate the true number of satellites within DR5 for a number of scenarios. The most comparable scenario to our assumptions (a limiting distance of 300 kpc, including all satellites except Segue 1 which is not in DR5) gives a result of 322_{-75}^{+144} satellites, consistent with our results of 232 for R_{90} and 344 for R_{99} .

4.3 Allowing a Little Latitude

Substantial effort has gone into the observation and interpretation of the spatial distribution of the satellites of disk galaxies, in particular that of the MW satellites. However, there is neither agreement on whether the Milky Way satellites have a truly anisotropic spatial distribution, nor whether we expect them to. Pre-SDSS, Kroupa et al. (2005) found that the distribution of known MW satellites could be described by a disk of finite width, aligned almost perpendicularly to the MW disk. This was in agreement with the “Holmberg” effect (Holmberg, 1969), that the closest satellites to a host galaxy were observed to be preferentially aligned with the minor axis of the host. This disk-

like distribution seemed incompatible with Λ CDM, but Kang et al. (2005) reasoned that if satellites follow the distribution of the host DM profile rather than that of the substructure then the dozen observed MW satellites could statistically lie in a disklike structure, although the orientation of this disk is arbitrary. Piatek et al. (2007) used proper motions derived from *HST* observations to show that this “Great Disk of MW Satellites” was not a persistent structure; the orbits of the dwarfs would not contain them within this disk. Metz et al. (2008) refute this conclusion, finding instead that the orbital poles of most MW satellites place them in a rotationally supported disk of satellites. Studies on the satellites of other galaxies from SDSS also yield conflicting results. Bailin et al. (2008) affirm the Holmberg effect while Brainerd (2005) find that satellites lie preferentially along the major, not minor, axis of the host. Zentner et al. (2005) re-examine the problem from a theoretical point of view, stating that DM substructure is not completely isotropic and that the MW satellite distribution can, albeit with a very low probability, be drawn from a DM subhalo distribution.

Within the standard Λ CDM structure formation scenario, satellite galaxies without DM could be formed in gas-rich tidal tails during vigorous early galaxy–galaxy interactions (Okazaki & Taniguchi, 2000). Families of such tidal dwarfs would have correlated orbital angular momenta and may appear as disklike arrangements about some hosts. This would support the apparent disk of satellites (Kroupa et al. 2005; Metz et al. 2007) and its correlated orbital angular momenta (Metz et al. 2008). It is therefore crucial to further constrain the spatial and orbital angular momentum properties of the satellites to reveal their true nature which is intimately related to the formation of the MW.

A caveat of past studies of the MW dwarf distribution is that the sky had not been uniformly searched for satellites and the effect of Galactic latitude on the observability of dwarfs had not been thoroughly quantified. In their detailed study, Kleyana et al. (1997) showed that latitude strongly affected the detectability of MW satellites with their technique. Our uniform study of SDSS DR6 takes their approach a step further and provides a detailed quantitative description of dwarf detectability over the footprint of our survey. We established in Section 3.2.4 that the average detectability of the known satellites does not significantly vary over the DR6 footprint. We can thus compare the latitude and longitude distributions of the MW satellites within the DR6 footprint with that expected if they are randomly distributed. We perform a Kolmogorov-Smirnov (K–S) test to determine whether the satellites detected in DR6 show statistically significant spatial anisotropy. Figure 4.1 shows the cumulative distributions (black lines) of latitude (top) and longitude (bottom) by area of the DR6 footprint. Overplotted on both panels are the cumulative distributions of MW satellites, both ignoring the ambiguous objects Boötes II, Willman 1 and Segue 1 (blue) and including them (red). A K–S test on these distributions with the entire DR6 area yields probabilities of isotropic distribution of 0.16 over longitude and 0.72 over latitude, or 0.06 and 0.79 if we include Segue 1, Willman 1, and Boötes II. We also randomly pick 12 (or 15) points from DR6 coverage, weighted by area, and repeat the K–S test 1000 times. The mean resulting probabilities of isotropic distributions are 0.45 ± 0.29 over

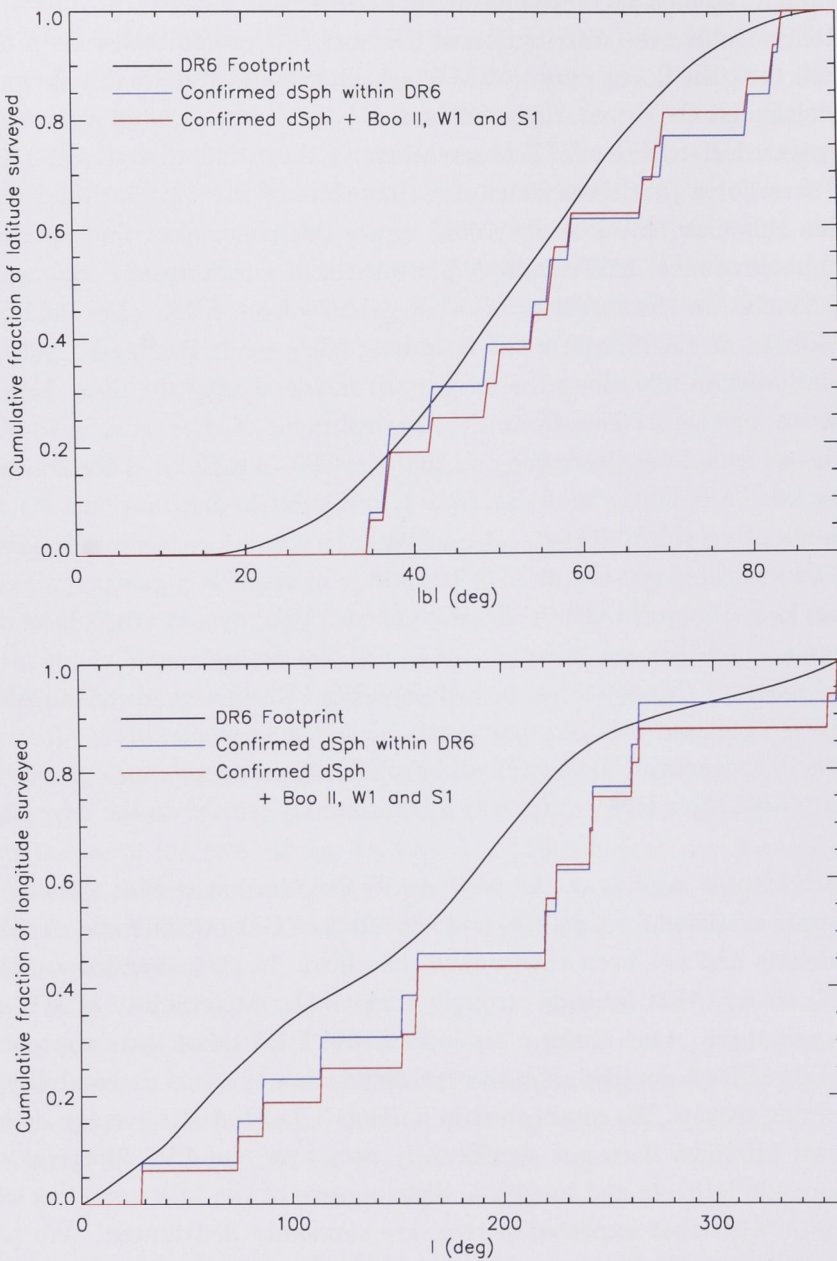


Fig. 4.1 — *Top*: cumulative histogram of the Galactic latitude of the DR6 footprint weighted by area (black). Blue shows the cumulative histogram of the latitudes of confirmed dSph within DR6 and the MW virial radius (Boo, Dra, CVn, CVn II, ComBer, Leo I, Leo II, Leo IV, Her, UMa, and UMa II). Red shows the same but including Boo II, Willman 1, and Segue 1. *Bottom*: same as the top panel, but for Galactic longitude.

longitude and 0.62 ± 0.27 over latitude, or 0.34 ± 0.28 and 0.55 ± 0.28 with Segue 1, Willman 1, and Boötes II. Hence, a conclusive result on the isotropy of the MW satellites

awaits further data as our test shows that by considering DR6 alone either scenario is plausible.

4.4 Conclusion

The dwarf galaxy satellites of the MW provide excellent opportunities to further our understanding of galaxy formation and near-field cosmology. They can be resolved into individual stars allowing detailed studies of their structure, kinematics and composition. They have also been cause for concern regarding their interpretation as the luminous components of DM substructure; it has been argued that the number and spatial distribution of these satellites are inconsistent with Λ CDM structure formation scenarios. The commencement of the SDSS triggered a cascade of discoveries, with 14 new satellites discovered. The limited spatial coverage and photometric depth of SDSS suggests that many, if not most, MW satellites are still yet to be discovered. The coming years are likely to bring the MW satellite census toward completeness as new survey telescopes such as SkyMapper, Pan-STARRS and LSST come online.

We present here the method used to search the SDSS DR6 for ultra-faint MW satellite galaxies. By screening for stars consistent with an old population at a fixed distance, we enhance the signal of a dSph over the Milky Way foreground. Smoothing with a kernel corresponding to the expected surface density profile further elevates the dSph above the foreground, and our comprehensive thresholds account for varying stellar density and more diffuse objects.

Applying our algorithm to SDSS DR6, we recover the “classical” and recently discovered dSphs, as well as 17 globular clusters and two open clusters. We also have 30 unidentified detections, some of which may be new satellites. The discovery of Leo V demonstrates the difficulty in following-up dwarf candidates; while we detect Leo V, there are several unknown detections of greater significance that may prove to be something. However, observing these weakest candidates is a rather hit and miss affair, as pointed out by Belokurov et al. (2008).

To compare the known dwarf galaxy population of the MW with predictions, it is essential to have a very well-defined dwarf selection function. To do this, we thoroughly model the detection efficiency of systems covering a wide range in parameter space by simulating more than 3,000,000 galaxies. We fit various functions to the resulting detection efficiency contours to semianalytically describe efficiency as a function of magnitude, size, distance and Galactic latitude. Using the results of our detailed investigation of dwarf detectability, we show that

1. Assuming a Via Lactea subhalo radial distribution and that $R_{complete} = R_{90}$, there should be ~ 13 satellites within DR6, 12 of which are known. If we include Segue 1, Willman 1, and Boötes II in this calculation, this estimate jumps to ~ 56 , only 15 of which are known.
2. Dwarf detectability shows a smooth transition from 100% to 0% over size and

distance. For example, the distance at which a CVn II-like object is detected with 90% efficiency is 200 kpc, compared to 316 kpc for 10% efficiency.

3. Galactic latitude does not significantly impact the detection of satellites over the DR6 footprint, and surveys of similar quality should still detect dwarfs as low as $b \approx 15^\circ$. All of the satellites discovered in SDSS would have been detected at any latitude.
4. The census of MW satellites brighter than $M_V = -6.5$ should be complete out to 300 kpc, and all objects brighter than $M_V = -5$ would be detected with at least 50% efficiency out to this distance.
5. Given the present data, the spatial anisotropy of the MW satellites within DR6 can neither be confirmed nor ruled out.

We provide several different parameterizations of our detection limits to facilitate comparisons between the known MW dwarf galaxy population and predictions. We provide software that returns the detection efficiency of a dwarf galaxy as a function of its luminosity, scale size, distance, and latitude. There are two different codes provided for this; one is based on an analytic description of our detection limits and the other provides a direct interpolation from our 3,825,000 simulated galaxies. We also provide a linear fit as a function of M_V of the distance out to which dwarfs are detected with each of 50%, 90%, and 99% efficiency. These fits assume an underlying dwarf galaxy population with combinations of sizes and luminosities similar to those known.

2009 will bring about the beginning of the Southern Sky Survey with the ANU SkyMapper telescope, and with it a way to uniformly search a further $\sim 20,000 \text{ deg}^2$ of sky for new MW dwarfs. We can naively expect to find around twenty-five new Milky Way satellites. With a detailed, systematic search covering around three quarters of the sky, we will for the first time be able to conclusively compare the MW satellite galaxy population with theoretical predictions. The apparent anisotropy of the satellites will be conclusively confirmed or ruled out and we will continue to discover the most dark matter dominated stellar systems nature produced. We may also implement improvements to the algorithm to optimize for stellar streams or young stellar populations. McConnachie et al. (2008) have shown that M31 satellites occupy as yet unexplored size-luminosity space around the Milky Way. Surveys beyond SDSS and SkyMapper, such as Pan-STARRS and LSST, will be needed to carefully search for such systems. Even with our carefully characterized detection limits the true number of MW satellites remains highly uncertain.

ACKNOWLEDGEMENTS

Thanks to the anonymous referee, Tony Martin-Jones, Patrick Tisserand, Pavel Kroupa, Iskren Georgiev, Jose Robles and Charley Lineweaver for helpful comments and discussion. We thank Bill Wyatt and the Telescope Data Center at SAO for maintaining a copy of SDSS at the Harvard-Smithsonian Center for Astrophysics. S.W. thanks

the Institute for Theory & Computation (ITC) at Harvard for support and hospitality and the Smithsonian Astrophysical Observatory for financial support during the final stages of this work. H.J. and S.W. further acknowledge financial support from the Go8/DAAD - Australia Germany Joint Research Cooperative Scheme and through the Australian Research Council Discovery Project Grant DP0451426.

Chapter 5

A Pair of Boötes: A New Milky Way Satellite

Relevant quotes, like the stars of Boötes II, are few and far between.

– Shane Walsh

ABSTRACT

As part of preparations for a southern sky search for faint Milky Way dwarf galaxy satellites, we report the discovery of a stellar overdensity in the Sloan Digital Sky Survey Data Release 5, lying at an angular distance of only 1.5 degrees from the recently discovered Boötes dwarf. The overdensity was detected well above statistical noise by employing a sophisticated data mining algorithm and does not correspond to any catalogued object. Overlaid isochrones using stellar population synthesis models show that the color-magnitude diagram of that region has the signature of an old (12 Gyr), metal-poor ($\text{Fe}/\text{H} \approx -2.0$) stellar population at a tentative distance of 60 kpc, evidently the same heliocentric distance as the Boötes dwarf. We estimate the new object to have a total magnitude of $M_V \sim -3.1 \pm 1.1$ mag and a half-light radius of $r_h = 4'.1 \pm 1'.6$ (72 ± 28 pc) placing it in the $40 < r_h < 100$ pc void occupied by another recently discovered Milky Way Satellite, Coma Berenices.

5.1 Introduction

The last three years have seen a torrent of new Milky Way (MW) satellites being discovered in the Northern hemisphere, almost doubling the number known prior to 2005: Boötes (Belokurov et al. 2006a), Canes Venatici (Zucker et al. 2006a), Willman 1 (Willman et al. 2005a), Ursa Major (Willman et al. 2005b), Ursa Major II (Zucker et al. 2006a), Hercules, Coma Berenices, SEGUE 1, Canes Venatici II, Leo IV (Belokurov et al. 2006b), and Leo T (Irwin et al. 2007). Eight of these new objects are consistent in size and luminosity with dwarf spheroidal satellites while Willman 1 and Segue

1 straddle the intersection of dwarfs and globular clusters. Coma Berenices falls in an apparent void of objects spanning the 40 – 100 pc range (see Fig 1. Gilmore et al. 2007). These objects were all initially detected as overdensities of resolved stars in the photometric data of Sloan Digital Sky Survey (SDSS, York et al. 2000) and, with the exception of Leo IV, subsequently confirmed with follow-up observations. The numerous discoveries of extremely low surface brightness dwarf spheroidals (dSphs) in the 1/4 of the sky covered by SDSS strongly suggests that there are many more yet undiscovered. A significant new population of dwarf satellite galaxies would go a long way to reconcile the current discrepancy between Lambda Cold Dark Matter theory predictions (Klypin et al. 1999; Moore et al. 1999) and actual observed dSph numbers.

The next few years will see the advent of digital surveys that will enable all-sky searches for Milky Way satellites (e.g. PanSTARRS, Kaiser et al. 2005). We intend to blindly scan the entire Southern sky (20,000 square degrees) for new MW dwarf satellites with the upcoming Southern Sky Survey performed with the 1.3 meter ANU SkyMapper telescope at Siding Spring (Keller et al. 2007). The final combined ~ 25 TB catalog of the survey is estimated to reach a signal-to-noise of 5 at $r = 22.6$, 1.0 mag deeper than SDSS. In preparation for this survey we are testing sensitive data mining algorithms and search strategies using the freely available SDSS Data Release 5 (DR5, Adelman-McCarthy et al. 2006). A full overview, results and a detailed discussion will be presented in a subsequent paper (Walsh et al. in prep). Our software test on SDSS data has yielded several promising candidates, the most prominent of which we present here. While follow-up observations will reveal the candidate’s true nature in more detail, its size and luminosity are consistent with those of the other recent detections that have been labeled dwarfs spheroidals. We thus follow convention and designate it Boötes II.

5.2 Data and Discovery

DR5 includes a five color photometric catalogue covering 8000 square degrees around the north Galactic pole (Adelman-McCarthy et al. 2006). We have searched this publicly available data for concentrations of old stars at various distance intervals out to the Galactic virial radius of 250 kpc. We use a method similar to that described in Willman et al. (2002) and Willman (2003), and described in full in Walsh et al. (in preparation). We use a complicated set of cuts to identify all stellar sources in fields of 3° height in Declination and of arbitrary width in Right Ascension that are consistent in $(g - r, r)$ parameter space with that of a dSph at a desired distance (Red Giant Branch, Blue Horizontal Branch and Main-Sequence Turnoff). We then convolve the binned spatial positions of these sources with an exponential surface brightness profile and subtract the $0.9^\circ \times 0.9^\circ$ running mean from each $0.02^\circ \times 0.02^\circ$ pixel. A density threshold in standard deviations above the local mean is defined as a function of the background stellar density for each pixel, allowing us to search over fields with stellar density gradients. The process is repeated for different magnitude bins to change

sensitivity with distance.

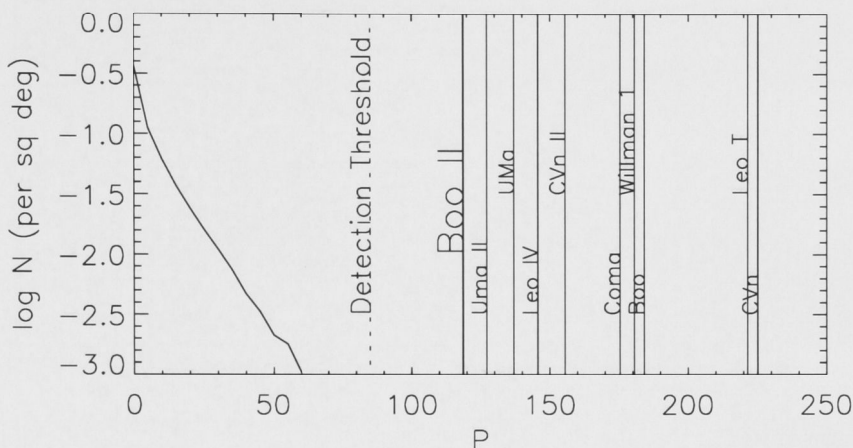


Fig. 5.1 — Curve of false positive detections (black line) as a function of the detection parameter P provided by our data mining algorithm. The detection threshold (vertical dashed line) is located at $P = 85$ above which our detection algorithm statistically yields less than one false detection over the entire 8800 square degrees of SDSS-DR5. Overplotted are the detection levels for the faintest known dSphs as well as the Boötes II object. With $P = 119$, the Boötes II overdensity is detected just below the UMa II ($P = 128$) and UMa ($P = 137$) dwarfs.

Applying this method to DR5 we recovered all of the recently reported dSphs, as well as many previously known objects such as globular clusters and background galaxy clusters. The detection significance of the faintest dwarfs, quantified by the parameter P (maximum level above threshold density times area above threshold), are shown in Fig. 5.1, along with the result for the new object. The solid line shows the number of “detections” in thirty-nine 1000 square degree randomized stellar fields each of varying stellar density to determine foreground contamination from random clustering. The newly discovered satellites (minus SEGUE 1 which fell outside the analyzed area) as well as the Boötes II overdensity are all well above the threshold $P = 85$ above which our detection algorithm statistically yields less than one false positive detection over the entire area of DR5. The Boötes II overdensity is not associated with any known Galactic or extragalactic object and is consistent in $(g - r, r)$ and size-luminosity space with a new dwarf. Figure 5.2 shows the position of Boötes II relative to Boötes.

Fig 5.3 shows our detections of Coma Berenices, Boötes II and Boötes. The contours represent the level above the threshold density, which is then multiplied by the detection area to give P . Coma Berenices and Boötes II peak at higher densities because they are more concentrated than Boötes, but the latter’s spatial extent means that it is still a stronger detection. The detection of Boötes II is consistent in all respects with the detections of the other Galactic satellites, albeit much fainter.

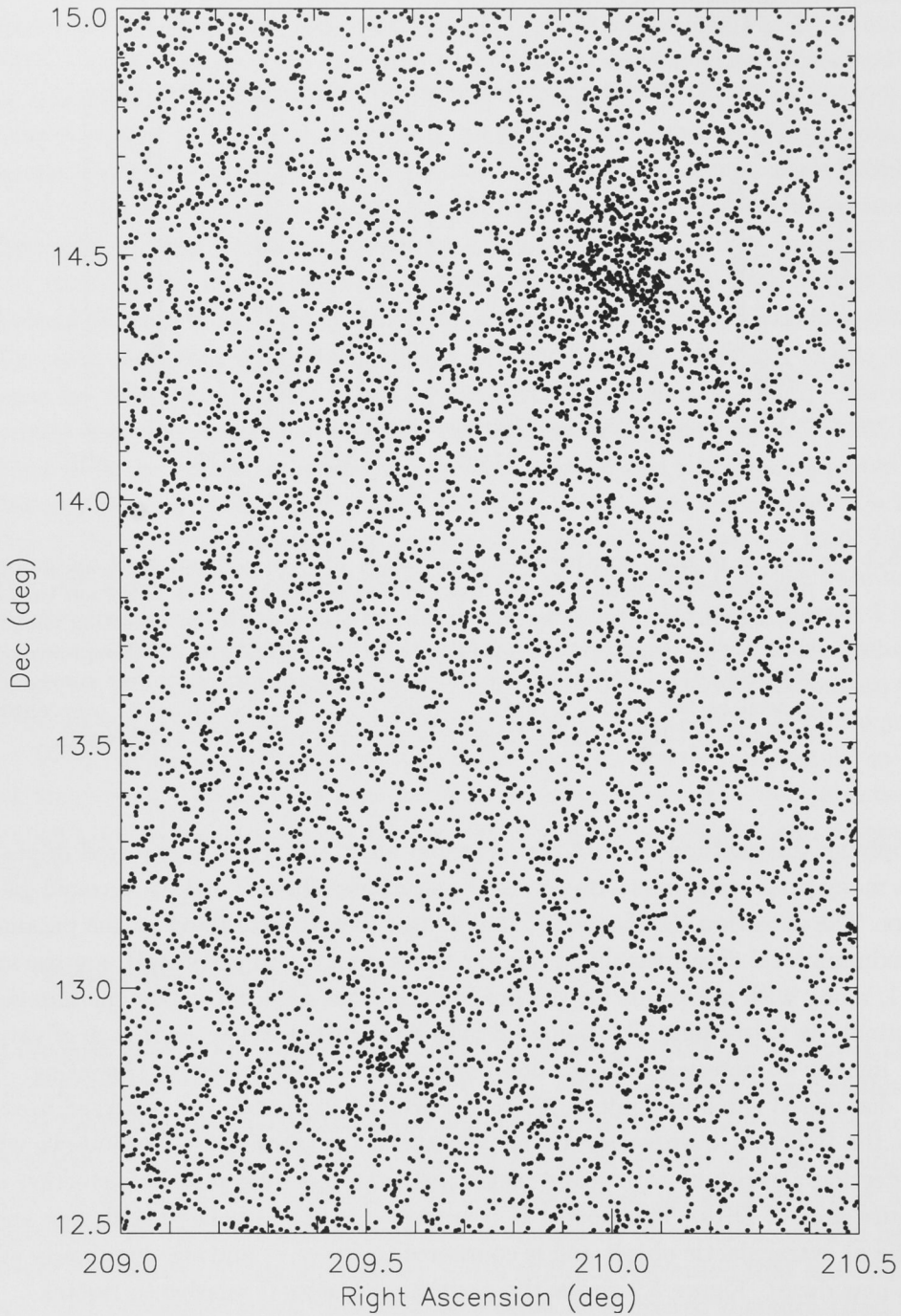


Fig. 5.2 — Positions of all SDSS stars with $17 < r < 23$ mag and $g - r < 0.65$. The Boötes dwarf is clearly visible (210.05d +14.50) as is our candidate 1.5 degrees to the south-west at 209.55d +12.85.

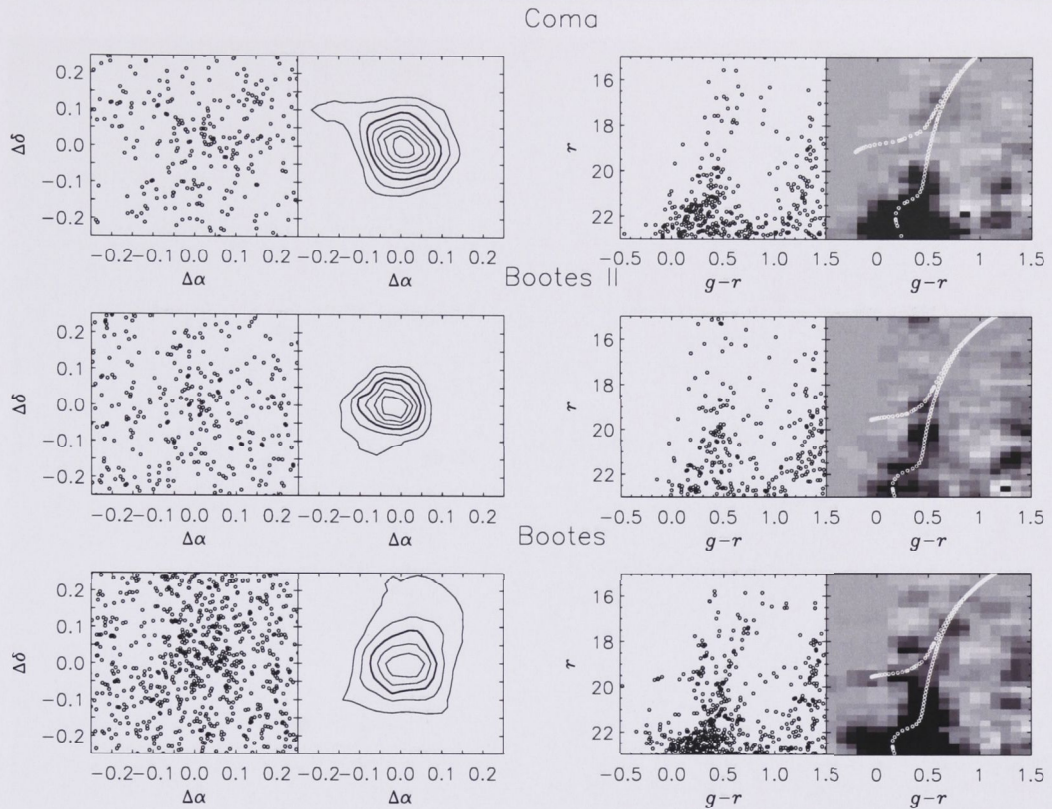


Fig. 5.3 — From top to bottom: Coma Berenices, Boötes II, Boötes. *Left Panels:* positions of SDSS stars passing the photometric selection criteria. *Middle Left:* Smoothed positions with contours at 0.5, 0.75, 1.0 (thick line), 1.2, 1.4, 1.6 and 1.8 multiples of threshold density. *Middle Right:* CMD of region within the 1.0 contour. *Right Panels:* field subtracted Hess diagrams of same regions with overlaid stellar isochrone.

5.3 Candidate Properties

We use SDSS data to extract as much information as possible and estimate preliminary parameters for Boötes II. The overdensity is visible even before smoothing and the lack of a concentration of background galaxies (Figure 5.4) allows to exclude a galaxy cluster as an origin. Looking at the CMD in Figure 5.3 reveals a weak red giant branch and blue horizontal branch (or red clump) at a distance modulus apparently identical to that of Boötes, and similar to the Coma Berenices dwarf ($m - M = 18.2$, Belokurov et al. 2006b). The CMD features become even more prominent in the associated area-normalized field-subtracted Hess diagram. Overplotted is the isochrone of a metal-poor ($[\text{Fe}/\text{H}] = -2.0$), old (12 Gyr) stellar population (Girardi et al. 2004) to illustrate the consistency of our object with an old stellar population. Using the assumed distance modulus of $(m - M) = 18.9$ (60 kpc) which is the same heliocentric distance of the Boötes dwarf, Boötes II would lie at a spatial distance of only ~ 1.6 kpc from Boötes. This hints at a physical connection between the two systems, although a further discussion of this idea is beyond the scope of this letter.

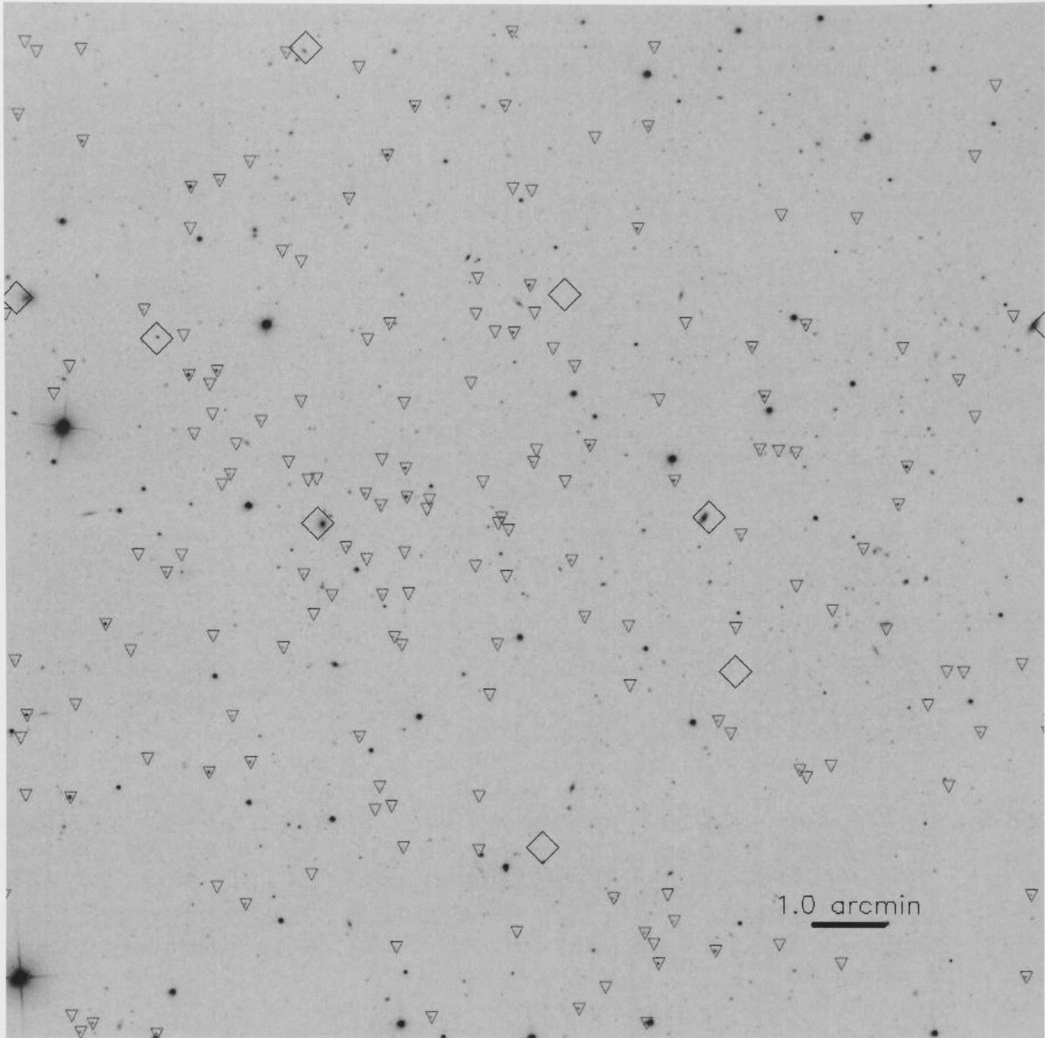


Fig. 5.4 — SDSS image ($15' \times 15'$) centered on the detection of Boötes II with SDSS galaxies overlaid (triangles). Left is East and Up is North.

Figure 5.5 presents the azimuthally averaged stellar density profile generated from all stars with $(g - r) < 0.65$ and $17.0 < r < 22.5$ centered on Boötes II. These data were then fitted with a Plummer profile (dotted line) plus a constant (dashed line), the latter to account for the foreground screen of Galactic stars. The best-fitting profile has a half-light radius of 4.1 ± 1.6 arcmin, approximately one third of the physical size of Boötes. Alternatively, fitting an exponential profile to the data gives a half-light radius of 4.0 ± 1.9 arcmin.

We use two methods to empirically derive the total magnitude of our object. Firstly we use SDSS coverage of the Draco dSph to calculate the flux ratio of the integrated luminosity functions. We derive a flux ratio $f_{Draco}/f_{BooII} \simeq 172 \pm 38$. This converts into a magnitude difference of 2.1 ± 0.3 mag and a total absolute magnitude of $M_V \sim -3.8 \pm 0.6$ mag for Boötes II, adopting $M_V = -9.4$ mag for Draco (Gebel et

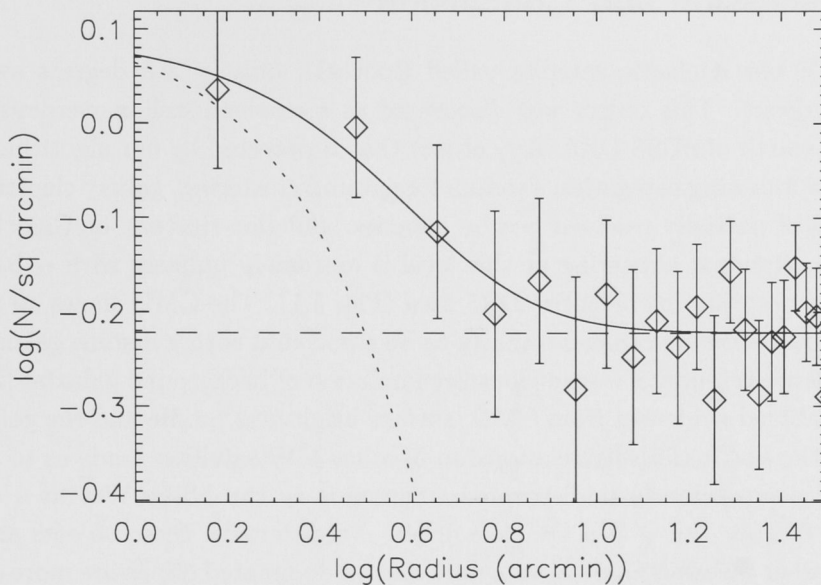


Fig. 5.5 — Radial stellar density profile generated from all stars with $(g - r) < 0.65$ and $17.0 < r < 22.5$ centered on the new object (diamonds). The dotted line is a Plummer profile with a scale parameter $a = 5.3$ arcsec and the dashed line is the contribution of foreground stars. The solid line is the combined fit.

al. (2003)). The same analysis yields $M_V \sim -6.0 \pm 0.6$ for Boötes, 0.7 mag brighter than $M_V \sim -5.3 \pm 0.6$ given by Belokurov et al. (2006a). Secondly, we use the integrated surface brightness profiles of Boötes and Boötes II. The flux ratio from this method gives $f_{Boo}/f_{BooII} \simeq 15$. Using $M_V \sim -5.3 \pm 0.6$ for Boötes gives $M_V \sim -2.4 \pm 0.6$. We therefore adopt a result of $M_V \sim -3.1 \pm 1.1$.

Table 5.1. Properties of Boötes II

Parameter	Boötes II		
RA (h m s)	13 58 00	[Fe/H]	-2.0
Dec (d m s)	+12 51 00	Age (Gyr)	12
(l, b)	(353.7, 68.9)	$\mu_{0,V}$ (Plummer)	29.8 ± 0.8
$(m - M)$	18.9 ± 0.5	r_h (Plummer)	$4'1 \pm 1'6$
Distance (kpc)	60 ± 10	$\mu_{0,V}$ (Exponential)	29.6 ± 0.8
M_V (mag)	-3.1 ± 1.1	r_h (Exponential)	$4'0 \pm 1'9$

5.4 Discussion and Conclusion

We report a new Galactic satellite called Boötes II, only ~ 1.5 degrees away from the Boötes dwarf. This object was discovered as a resolved stellar overdensity in an automated search of SDSS DR5. Any object that is detected by our algorithm will fall in one of the following categories: random foreground clustering, galaxy clusters, stellar associations of partially resolved nearby galaxies, globular clusters, or Galactic dwarf spheroidals. Random clustering at this level is extremely unlikely with ~ 0.008 such false objects occurring in the entire DR5 area (Fig. 5.1). The CMD shows an apparent MST and RGB structure that is unlikely to be associated with a distant galaxy cluster and no evidence is found of a suspicious accumulation of background galaxies (Fig. 5.4).

The combined evidences from CMD, surface brightness profile and the good agreement with the size-luminosity relationship of other MW satellites leads us to conclude this object is a previously undiscovered companion to the Milky Way at a tentative distance of 60 kpc. But is it a GC or a dSph? Traditionally, these objects are distinguished by their differing physical size; dark matter dominated dSphs are more extended than a purely stellar system of equal luminosity. Equipped with the two parameters $\log(r_h/\text{pc}) = 1.8^{+0.2}_{-0.3}$ and $M_V = -3.1 \pm 1.1$ mag for Boötes II we add our object to the other recently discovered dwarfs in the size-luminosity plot (Fig. 5.6). The distinction between dSphs and GCs is blurred in the low luminosity regime as was emphasized by the discovery of Willman 1 (Willman et al. 2005a). Boötes II falls alongside Coma Berenices in the 40–100 pc region devoid of other objects, between globular clusters and dwarfs. Boötes II is of comparable luminosity to SEGUE 1, but is a factor of ~ 2 larger.

With a physical half-light size that is an order of mag larger than most GCs but similar to those of dSphs, we are inclined to designate Boötes II a dwarf galaxy. However, without kinematic data, it is not possible to say for certain whether or not Boötes II formed inside of a dark matter halo, which would confirm it as such. It is also not possible with the current data to determine the extent to which tidal effects may have shaped the observed size and luminosity of Boötes II. A combination of follow-up spectroscopy and deep imaging will not only enable a more robust evaluation of the dark matter content of this object, but will also enable an evaluation of a possible physical relationship between Boötes and Boötes II.

ACKNOWLEDGEMENTS

We thank Pavel Kroupa, Manuel Metz and Jose Robles for useful discussions and comments in preparation of the manuscript. Funding for the SDSS and SDSS-II has been provided by the Alfred P. Sloan Foundation, the Participating Institutions, the National Science Foundation, the U.S. Department of Energy, the National Aeronautics and Space Administration, the Japanese Monbukagakusho, the Max Planck Society, and the Higher Education Funding Council for England.

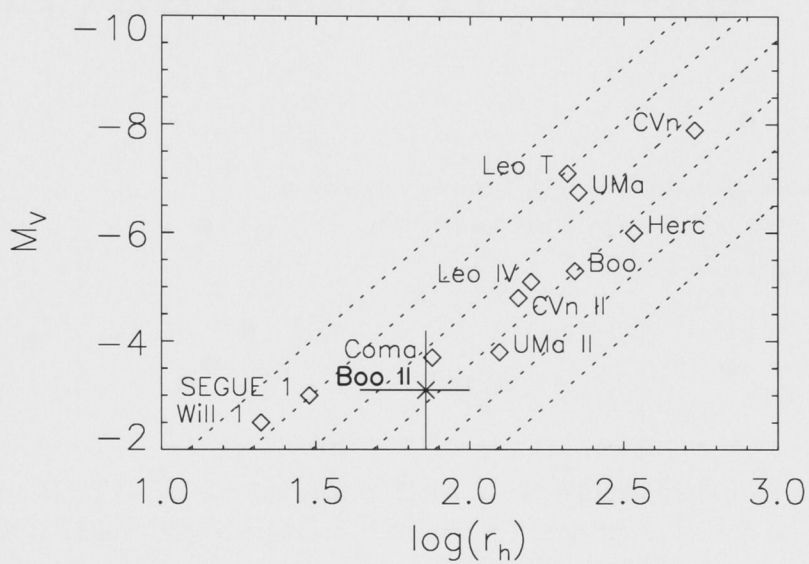


Fig. 5.6 — Absolute magnitude (M_V) versus half-light radius (r_h in pc) for all Galactic companions discovered in SDSS. Boötes II is shown as an asterisk, with associated error bars. Lines of constant central surface brightness are shown with $\mu_V = 27, 28, 29, 30, 31$ and $32 \text{ mag arcsec}^{-2}$ from left to right.

Chapter 6

Boötes II ReBoöted: MMT/Megacam Follow-up

*You can use statistics to prove just about anything.
Fourteen percent of all people know that.*

–Homer Simpson

ABSTRACT

We present MMT/Megacam imaging in Sloan g and r of the extremely low luminosity Boötes II Milky Way companion. We use a bootstrap approach to perform robust measurements of, and uncertainties on, Boötes II's distance, luminosity, size, and morphology. Comparisons with theoretical isochrones and empirical globular cluster fiducials show that Boötes II's stellar population is old and metal-poor ($[\text{Fe}/\text{H}] < -2$). Assuming a stellar population like that of M92, Boötes II is at a distance of 42 ± 8 kpc, closer than the initial published estimate of 60 ± 10 kpc. This distance revision, combined with a more robust measurement of Boötes II's structure with a Plummer model (exponential model) results in a more compact inferred physical half-light size of $r_h \simeq 36(33) \pm 9(10)$ pc and lower inferred luminosity of $M_V \simeq -2.4(-2.2) \pm 0.7(0.7)$ mag. The revised size and luminosity we calculate move Boötes II into a region of size-luminosity space not previously known to be occupied by old stellar populations, but also occupied by the recently discovered Milky Way satellites Willman 1 and SEGUE 1. We show that the apparently distorted morphology of Boötes II is not statistically significant given the present data. We use a tidal argument to support a scenario where Boötes II is a dwarf galaxy (dark matter dominated) rather than a globular cluster (not dark matter dominated), although the uncertainty on the M/L we infer for Boötes II is substantial. Moreover, we can not rule out that Boötes II is a star cluster on the verge of disruption, such as Palomar 5.

6.1 Introduction

Over the last 5 years, the Sloan Digital Sky Survey has been extensively searched for extremely low surface brightness dwarf spheroidal galaxies. These searches use the catalog of stellar sources to identify spatial overdensities of the old, metal-poor stars characteristic of these dwarfs. To date, these searches (e.g Willman et al., 2002; Kopolov et al., 2008) have resulted in the discoveries of fourteen new Milky Way satellites.

Most of these new objects have total luminosities less than the median luminosity of the Milky Way’s globular clusters ($M_V \sim -7$), but have sizes characteristic of known dwarf spheroidals ($r_{half} \gtrsim 100$ pc), complicating their classifications as either star clusters or dwarf galaxies. In this paper, we assert that the physical distinction between a globular cluster and a dwarf galaxy is that a dwarf galaxy is, or was at some point, the primary baryonic component of a dark matter halo whereas a globular cluster was not. Nine of the 14 new satellites were originally classified as dwarf spheroidals because they had scale sizes $\gtrsim 100$ pc (Boötes, Canes Venatici, Canes Venatici II, Coma Berenices, Hercules, Leo IV, Leo T, Ursa Major and Ursa Major II; Belokurov et al., 2006b; Zucker et al., 2006b; Sakamoto & Hasegawa, 2006; Belokurov et al., 2007; Willman et al., 2005b; Zucker et al., 2006a). Follow-up spectroscopic studies demonstrated that they indeed appear to require dark matter to explain their kinematics, securing their classification as dwarf galaxies (Simon & Geha, 2007; Martin et al., 2007; Strigari et al., 2007a; Walker et al., 2007). Kopolov 1 and 2 (Kopolov et al., 2007) have scale sizes of only 3 pc, and have thus been classified as new globular clusters.

The classification of the other three new satellites, Segue 1, Willman 1, and Boötes II ($M_V \sim -2.5$; Belokurov et al., 2007; Willman et al., 2005a; Walsh et al., 2007), has been less straightforward. They are old stellar populations with sizes intermediate between known Milky Way globular clusters and dwarf spheroidals, but have fewer stars than nearly any known galaxy or globular cluster. Although initial estimates based purely on SDSS data placed Boötes II close to Coma Berenices in size-luminosity space at $(\log(r_h/pc), M_V) = (1.85, -3.1)$, in this paper we present estimates based on a more robust algorithm and on deeper, MMT/MegaCam imaging in g and r that shift Boötes II’s size and luminosity closer those of Willman 1 and Segue 1.

Despite its tiny luminosity, spectroscopic [Fe/H] estimates and kinematic studies of Willman 1 have provided support that it may require dark matter to explain its properties, thus classifying it as a dwarf galaxy (Martin et al., 2007; Strigari et al., 2007b). Whether or not these three Milky Way companions with only $\sim 1000L_\odot$ are galaxies or globular clusters is of fundamental import to both our understanding of galaxy formation at the smallest scales and to our understanding of the size and mass scale of dark matter clustering. Although the extent to which tides have effected Willman 1’s present-day luminosity is uncertain, this object raises the questions: Are we for the first time seeing the low luminosity and mass limit of galaxy formation? If so, what properties can we infer for the dark matter halos that host such galaxies? Segue I and Boötes II presently lack their own published spectroscopic studies with which to evaluate these scenarios. However, rigorous derivations of the detection limits of the

most recent SDSS searches for such objects (Koposov et al., 2008; Walsh, Willman & Jerjen *in prep*) show that many similar objects could remain yet undiscovered around the Galaxy, underscoring the importance of understanding their physical properties.

With the study presented in this paper, we aim to provide the first robust measurements of the basic properties (distance, luminosity, structure) of Boötes II and its stellar population, and to evaluate the present evidence for its classification. In §6.2, we describe MMT/MegaCam observations of Boötes II, data reduction, and artificial star tests. In §6.3, we use these data to derive revised estimates of Boötes II's properties, to verify that its stellar population is old and metal-poor, and to investigate whether it has a distorted morphology. We discuss these results and evaluate evidence for a dwarf galaxy versus globular cluster classification of Boötes II in §6.4.

6.2 Data

We observed Boötes II on June 05 2007 with MegaCam (McLeod et al., 2000) on the MMT. These data were obtained as part of a larger survey program to image with MMT/Megacam ultra-faint Milky Way satellites. MMT/MegaCam has 36 chips with 2048x4608 pixels of 0.08"/pixel, for a total field-of-view (FOV) of 24'. We obtained 5 180s dithered exposures in Sloan g , and 5 240s dithered exposures in Sloan r in grey conditions with 1.0 – 1.2" image quality in the g and 0.9 – 1.0" image quality in the r images. We reduced the data based on the method described in Matt Ashby's Megacam Reduction Guide*. Our reduction relied in part on software written specifically for MMT/MegaCam data reduction by Brian McLeod. We used the Sloan Digital Sky Survey Data Release 6 (SDSS DR6; York et al., 2000b; Adelman-McCarthy et al., 2008) stellar catalog to derive precise astrometric solutions for each science exposure. We also used the SDSS catalog to derive an illumination correction in g and r to divide out the variation in zero-point across MegaCam's FOV. We use local copies of the SDSS dataset, maintained at the Harvard-Smithsonian Center for Astrophysics.

We did a weighted co-addition of the reduced images using SWARP[†] and then used the DAOPHOTII/Allstar package (Stetson, 1994) to do point source photometry on the resulting images. We visually verified the integrity of the shape and full-width half-max of the PSFs in the stacked images across the 24' FOV. Photometry was carried out using a method similar to that of Harris (2007), with the exception that we used the command-line versions of DAOPHOT and Allstar rather than the IRAF versions.

To derive the photometric calibration for our data, we first matched the SDSS stellar catalog to the Allstar catalog for these new observations. We used the 91 SDSS stars within our field-of-view (FOV) with $18 < r < 21$ and $0.1 < g - r < 0.8$ to perform the photometric calibration. We limited the calibration to stars fainter than $r = 18$ mag to avoid the saturation limit of the MegaCam data. We limited the calibration to stars with colors between $0.1 < g - r < 0.8$ because the Boötes II member stars resolved in

*http://www.cfa.harvard.edu/~mashby/megacam/megacam_frames.html

[†]<http://terapix.iap.fr/soft/swarp>

this study (with the exception of a few possible blue horizontal branch stars) all have $0.1 < g - r < 0.6$. There were insufficient SDSS stars in our FOV bluer than 0.2 mag to determine whether our derived calibration is appropriate for very blue stars.

We then did a linear least-squares fit for the zero-points and color-terms, including uncertainties in color and magnitudes on each star and throwing out 3 sigma outliers.

$$g = g_{instr} + 7.27(\pm 0.029) + 0.091(\pm 0.068) \times (g - r) \quad (6.1)$$

$$r = r_{instr} + 7.33(\pm 0.025) + 0.074(\pm 0.054) \times (g - r) \quad (6.2)$$

Uncertainties were derived from a 1000 iteration bootstrap of the data. In addition, there is uncertainty in the SDSS zero-points themselves of about 0.01 mag (Padmanabhan et al., 2008).

Throughout this paper, we adopt SDSS photometry, rather than MegaCam photometry, for stars brighter than $r = 18.0$ mag. All magnitudes in this paper have been extinction corrected with the values from the Schlegel et al. (1998b) dust maps provided in the SDSS catalog; the median $E(g - r)$ along the line-of-sight to Boötes II is 0.02 mag.

We use artificial star tests to measure the photometric errors and completeness as a function of position in the $g - r$ color-magnitude diagram (CMD). Artificial stars are constructed from the g and r point spread functions (PSFs) measured during the data-reduction process, and are injected into the co-added g and r images using a uniform grid with spacing in X and Y equal to ten times the full-width half-max (FWHM) of the PSF (so that artificial stars overlap only beyond their 10σ radii). This fixed geometry imposes a limit on the number of artificial stars that can be added to the image of about 18,500. To build up our number statistics, we inject artificial stars into twenty copies of the g and r images, randomly offsetting the grid's zero-point position in X and Y for each iteration. This results in a total sample of 370,000 artificial stars. The r photometry of the artificial stars is drawn randomly from ~ 18 to 28 mag, with an exponentially increasing probability toward fainter magnitudes. To properly characterize the tail of the completeness function and the impact of blends on the photometric errors of faint objects, we simulate stars up to three magnitudes fainter than the nominal faint limit. The $g - r$ color is then drawn randomly over the range -0.5 to 1.5 mag to determine the g magnitude. We photometer the artificial-star images with the same photometry pipeline as we used on the science frames.

If an input artificial star is not present in both the g and r Allstar files, then it is flagged as a non-detection for calculation of the completeness rate. We applied a strict cut of DAOPHOT sharpness parameter of $-1 < sharp < 1$ for a star to be included our analysis, both for the actual Boo II data and for the artificial star tests. Although this strict sharpness cut yields completeness limits that are brighter than if we use no cut at all, we found it necessary to eliminate many galaxy interlopers and provide an improved measurement of Boötes II's stellar population while not sacrificing much

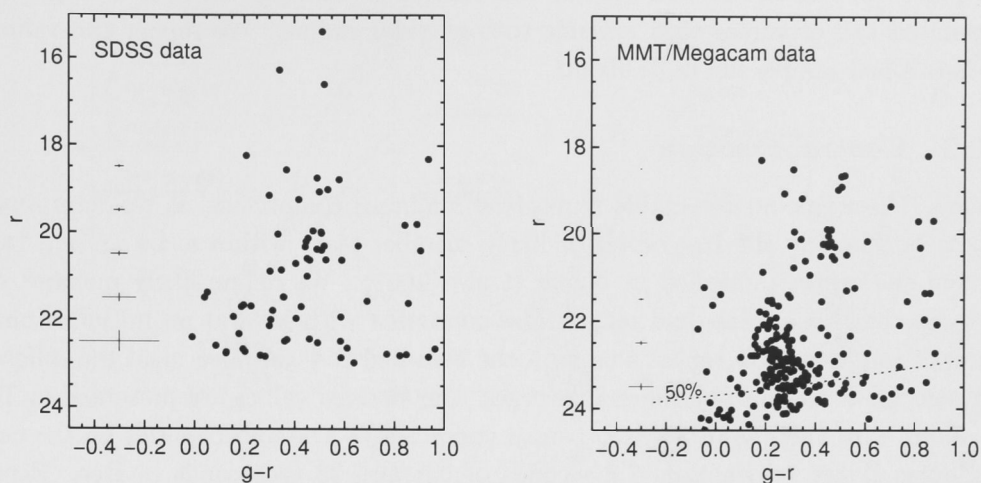


Fig. 6.1 — Color-Magnitude Diagrams of stars within 4.5 arcmin ($\sim 1.5\times$ Plummer half-light radii) of the center of Boötes II based on MMT/Megacam observations. The left CMD shows data from the SDSS DR6 and the right panel shows the MMT/Megacam data. Error bars showing the color and magnitude uncertainties as a function of r are overplotted.

precision in our quantitative results. At a $g - r$ color of 0.25 mag, the 50% and 90% completeness limits of these data are $r = 23.5$ and 22.9 mag.

Figure 6.1 shows the CMDs of stars within 4.4 arcminutes of the center of Boötes II from the SDSS DR6 data and from the MMT/Megacam data. The 50% completeness, as a function of color, is overplotted on the Megacam CMD.

6.3 Boötes II Properties

6.3.1 Bootstrap Analysis

With only ~ 100 object stars resolved in this study, small number statistics will constitute a substantial, if not dominant, source of uncertainty in the derived quantities. For the ambiguous ultra-faint satellites such as Boötes II, a rigorous examination of the uncertainties is essential to measure any of their properties. We use a 10,000 iteration bootstrap analysis to determine both the most likely values of Boötes II's properties, and the uncertainties associated with each measurement as detailed in the following sections. For each iteration, the data are randomly re-sampled with replacement and then analyzed to derive as described in the remainder of §6.3: central RA and Dec, distance modulus, Plummer and exponential half-light radii and total absolute magnitudes, King core and tidal radius, position angle, ellipticity, and asymmetry. Aside from King tidal radius, the bootstrapped distributions of the derived parameters are well described by a Gaussian. All quoted values and uncertainties are thus the peaks and standard deviations of the bootstrap distributions. For the King tidal radius,

we quote the half-width, half-max as the uncertainty because there is a long, poorly populated tail of values that extends to high tidal radius. We report the values of bootstrapped sample fits in Table 6.1.

6.3.2 Central Position

Boötes II contains no detectable unresolved luminous component, so we determine its center by locating the barycenter of likely member stars within a 4.5 arcmin radius around the center published in Walsh et al. (2007). We define likely member stars as those that have colors and magnitudes consistent with M92 at an initial estimated distance modulus. We repeat this with the returned RA and Dec until the difference between input and output values converges. Our derived values are presented in Table 6.1 along with their associated bootstrap uncertainty. The uncertainties on the center of Boötes II are substantial: 7.2 seconds of RA and 23 arcseconds in Dec. Because all parameters are derived for each of the bootstrapped samples, these uncertainties on the center are automatically propagated through to the uncertainties in Boötes II's structural parameters.

6.3.3 Distance

To investigate the distance to Boötes II's stellar population, we first compare its CMD to empirical globular cluster fiducials (M92, M3, M13, and M71) with $-2.4 < [Fe/H] < -0.7$. We use $m - M = 14.60, 15.14, 14.42$ and 13.71 for the four clusters (Paust et al., 2007; Kraft & Ivans, 2003; Cho et al., 2005; Grundahl et al., 2002). We choose to rely on fiducials, rather than theoretical isochrones, because these well studied globular clusters have photometry in the exact photometric system we have calibrated our data to. The fiducials we use are based on those of Clem et al. (2007) in Sloan $g' - r'$. They were converted into $g - r$ using the transformation of Rider et al. (2004) and checked by comparing the transformed fiducials directly to the SDSS imaging of the clusters in the SDSS DR6 (J. Strader, private communication). The robustness of our comparison depends on Boötes II having an old stellar population, like those in these four comparison clusters. We address and confirm this with theoretical isochrones in §6.3.4.

For each fiducial, we find the distance modulus that provides the best fit to the stars in the CMD shown in the right panel of Figure 6.2. This CMD includes all stars within 4.5 arcmin of Boötes II. To determine this distance modulus, we step each fiducial through 0.05 magnitude intervals in $(m - M)$ from 17.5 to 19.5 mag and find the number of stars brighter than $r = 23.5$ that, considering color uncertainties, have colors within 0.05 magnitudes of the fiducial. To eliminate the contribution of stars belonging to the thick disk and halo, we then do the same for stars exterior to 9.0 arcmin and subtract this value normalized to an area of $\pi(4.5')^2$. We take the best fit for each fiducial as the distance modulus that maximizes this number of stars. The best fit distance moduli for the M92, M3, M13 and M71 fiducials are 18.1, 18.1, 18.1 and 18.85 with 96, 77, 87 and 43 stars respectively.

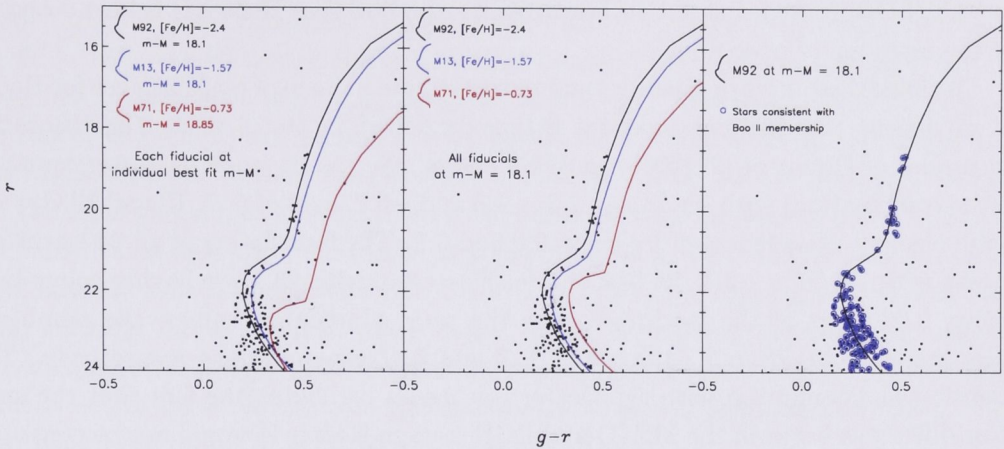


Fig. 6.2 — Color-Magnitude Diagrams of stars within 4.5 arcmin of the center of Boötes II *Left*: Globular cluster fiducials overplotted at their own best fit distance modulus. *Center*: GC fiducials overplotted at M92 best fit distance modulus of $m - M = 18.1$ *Right*: M92 fiducial at $m - M = 18.1$ with probable Boötes II member stars highlighted.

The left panel of Figure 6.2 shows the M92, M13 and M71 fiducials overplotted on the MMT CMD at their individual best fit distances. For simplicity we include M13 and not M3, because they have similar $[\text{Fe}/\text{H}]$ and M13 provides a better match both quantitatively and qualitatively. In the central panel of Figure 6.2 we overplot the empirical M92, M13 and M71 fiducials, all projected to the M92 best fit distance modulus of $m - M = 18.1$ (42 kpc). These confirm that it is reasonable to infer that the stellar population of Boötes II is like that of M92. We therefore use the M92 fiducial in our bootstrap analysis to derive the best-fit distance, which yields a distance modulus of $m - M = 18.1 \pm 0.06$, only including the formal bootstrap uncertainty, stemming from small number statistics. We add in quadrature the distance modulus uncertainty of M92 (0.09 mag, Paust et al., 2007) and the r zero-point uncertainty (0.025 mag, §6.2) to derive $m - M = 18.1 \pm 0.06$, or $d = 42 \pm 2$ kpc. If Boötes II has a stellar population different from M92, then the uncertainty in the distance is larger.

6.3.4 Stellar Population

M92 has a very low $[\text{Fe}/\text{H}]$ of -2.4 and is α -element enhanced relative to solar ($[\text{Ca}/\text{Fe}] = 0.3$, Sneden et al., 2000). The match between M92 and Boötes II's stellar populations thus supports $[\text{Fe}/\text{H}]_{\text{BooII}} < -2$, even if Boötes II is α -depleted relative to M92 (typical of the contrast between dSph and globular cluster populations, Pritzl et al., 2005). Figure 6.2 shows that M13's fiducial sequence is only 0.04 mag redder in $(g-r)$ than that of M92 below the main-sequence turnoff. The uncertainties in the g and r zero-points of the MegaCam data in Figure 6.2 result in a $(g-r)$ calibration that is uncertain at 0.038 mag. These Boötes II data are thus also consistent with having a more moderate

abundance ($[\text{Fe}/\text{H}] \sim -1.6$). However, using independent V and I observations obtained on VLT/FORS2, Jerjen et al. (in preparation) also find that Boötes II is best described by the most metal-poor fiducials.

To check these empirical results and to investigate a range of possible ages for Boötes II, we repeat the distance modulus fitting described in §6.3.3 using the theoretical isochrones of Dotter et al. (2008) in SDSS colors. We use 24 isochrones corresponding to the combinations with $[\text{Fe}/\text{H}] = -2.3, -1.5$ and -0.7 , ages of 5, 7, 10 and 13 Gyr and alpha-element abundances of $[\alpha/\text{Fe}] = 0.0$ and 0.2 . The best fitting of all 24 isochrones is that with $[\text{Fe}/\text{H}] = -2.3$, 13 Gyr and $[\alpha/\text{Fe}] = 0.2$, with 98 stars having colors lying within 0.05 mags of the isochrone. For the same abundance values, the number of stars drops to 86, 78 and 72 for the 10, 7 and 5 Gyr populations respectively. This quantitative comparison with the Dotter isochrones highlights the fact that the small color difference between the MSTO and RGB stars in Boötes II would not be consistent with a stellar population much younger than 13 Gyr.

6.3.5 Structural Parameters

The surface density profiles of globular clusters and dwarf spheroidal galaxies (dSphs) are commonly parameterized by King (King, 1966), Plummer (Plummer, 1911) and exponential profiles. To facilitate comparison with other observational studies, we fit all three profiles to the stellar distribution of Boötes II:

$$\Sigma_{King}(r) = \Sigma_{0,K} \left(\left(1 + \frac{r^2}{r_c^2} \right)^{-\frac{1}{2}} - \left(1 + \frac{r_t^2}{r_c^2} \right)^{-\frac{1}{2}} \right)^2 \quad (6.3)$$

$$\Sigma_{Plummer}(r) = \Sigma_{0,P} \left(1 + \frac{r^2}{r_P^2} \right)^{-2} \quad (6.4)$$

$$\Sigma_{exp}(r) = \Sigma_{0,E} \exp \left(-\frac{r}{\alpha} \right) \quad (6.5)$$

where r_P and α are the scalelengths for the Plummer and exponential profiles and r_c and r_t are the King core and tidal radii, respectively. For the Plummer profile, r_P equals the half-light radius r_h , while for the exponential profile $r_h \approx 1.668\alpha$. The circled stars in the right panel of Figure 6.2 show the color-magnitude criteria we use to select probable Boötes II member stars for calculating its center and for investigating its structure. Figure 6.3 shows the spatial distribution of stars that pass these cuts, and the location of their derived center. Figure 6.4 shows the surface density profile of Boötes II around this center, where the error bars were derived assuming Poisson statistics. Using a non-linear least squares method, we fit Plummer and exponential models plus a constant field contamination to this surface density profile. The surface density profile fits are only constrained to be physically possible systems (i.e. field contributions must be positive). In the case of the King profile, the tidal radius is present in a constant term, hence there is a degeneracy between the field value and the tidal radius. To circumvent this we first fix the King field value using the mean of the

fitted Plummer and exponential field values.

All three fits yield consistent characteristic radii; Assuming a distance modulus of $m - M = 18.1$, the Plummer and exponential profiles yield physical half-light radii of $r_{h,Plummer} \simeq 36 \pm 9$ pc and $r_{h,exponential} \simeq 33 \pm 10$ pc. The King model fit yields a core radius of $r_c \simeq 25 \pm 9$ pc and a tidal radius of $r_t \simeq 155 \pm 35$ pc. Although this tidal radius lies just outside the extent of the radial profile we can measure, we find that the inner radial bins constrain the core radius and central density while fixing the field value leaves only the tidal radius as a free parameter. In the event that the outer radial bins are contaminated with Boo II stars, and therefore higher than the true field value, the tidal radius could be much larger. As an example, if the true field value is an overestimate of 25% by the Plummer and exponential models, then the best fit tidal radius is ~ 215 pc while the core radius remains relatively constant at ~ 22 pc. The fitted King tidal radius of $r_t \simeq 155 \pm 35$ is a lower limit.

Figure 6.5 shows in greyscale the distribution of King core and tidal radii derived from the bootstrap of Boötes II stars. Overplotted are the measured core and tidal radii of Galactic globular clusters. We have overplotted lines of constant concentration (r_{tidal}/r_{core}) and the concentrations of known globular clusters calculated with the tidal and core radii in the catalog of Harris (1996). Only a handful of known globulars have $r_h \geq 10$ pc and the only one larger than $r_h \sim 20$ pc is known to be tidally disrupting (Pal 5). However, this figure shows several known globular clusters with a King concentration as low as Boötes II. The King concentrations of the Milky Way's dwarf spheroidals range from 0.48 – 1.12 (Mateo, 1998), similar to the range of GCs in this figure. We do not overplot the King parameters of the classical Milky Way dwarf galaxies, because their relaxation times are \sim a Hubble time. Their King profile fits thus contain less physical meaning than those of objects with shorter relaxation times, such as globular clusters and Boötes II (see §6.4 for discussion).

6.3.6 Luminosity

To estimate the total luminosity of Boötes II we integrate the model components of the surface density profile, corrected for incompleteness, to derive the number of Boötes II stars within the CMD selection cuts. Using this to normalize the theoretical luminosity function gives estimates of $M_r = -2.6$ ($M_V = -2.4$) for the Plummer profile and $M_r = -2.4$ ($M_V = -2.2$) for the exponential profile (using $V - r = 0.16$, adapted from Girardi et al., 2004 for a 13 Gyr, $[\text{Fe}/\text{H}] = -2.27$ stellar population). We obtain these magnitudes after correcting for the missing flux from stars fainter than $r = 23.5$ by integrating the theoretical luminosity function taken from Girardi et al. (2004) for a $[\text{Fe}/\text{H}] = -2.27$, 13 Gyr population. This method counts the number of stars without regard to their individual magnitudes, which in systems of such low luminosity could strongly be affected by the addition or subtraction of a single RGB star. Such a star's individual magnitude could be much brighter than $M_V = -2$, rendering a more traditional summing of fluxes method unreliable. As the total luminosity of a stellar system becomes comparable to the luminosity of individual stars, the summed luminosity be-

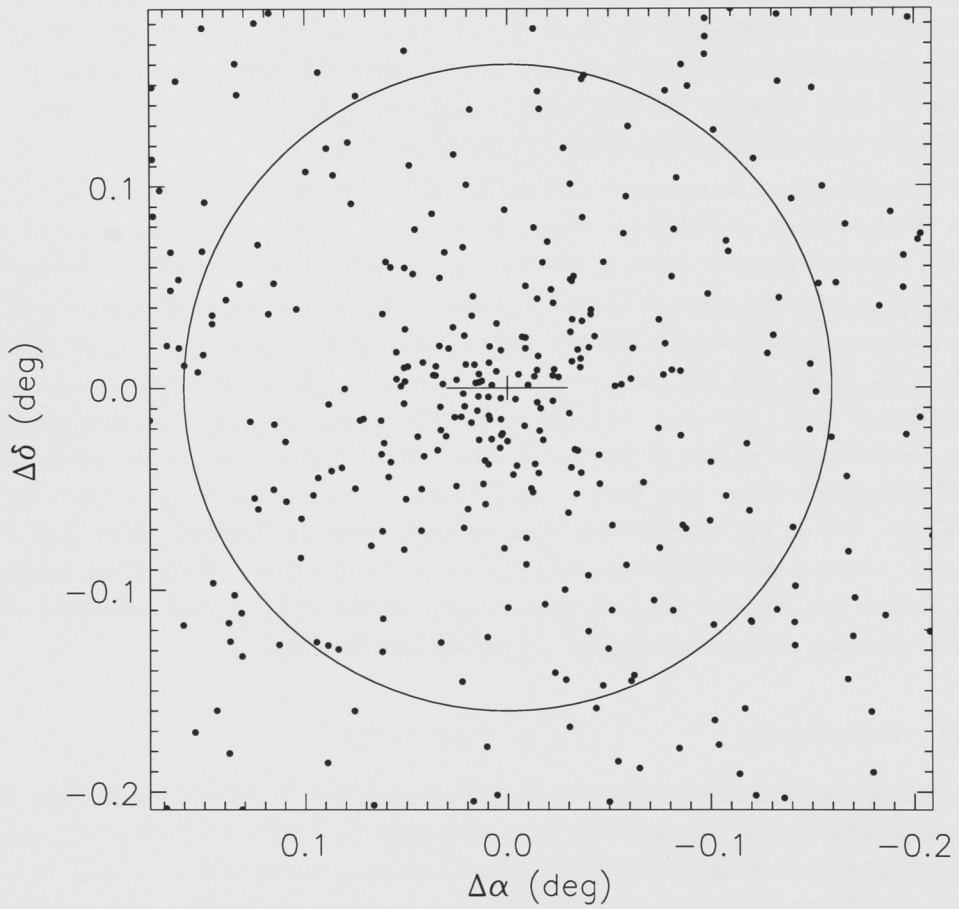


Fig. 6.3 — Positions of stars passing selection cuts. The calculated center of Boötes II is highlighted by the crosshair, which spans the RA and Dec uncertainties. The large circle shows the maximum radius of the surface density profile fit.

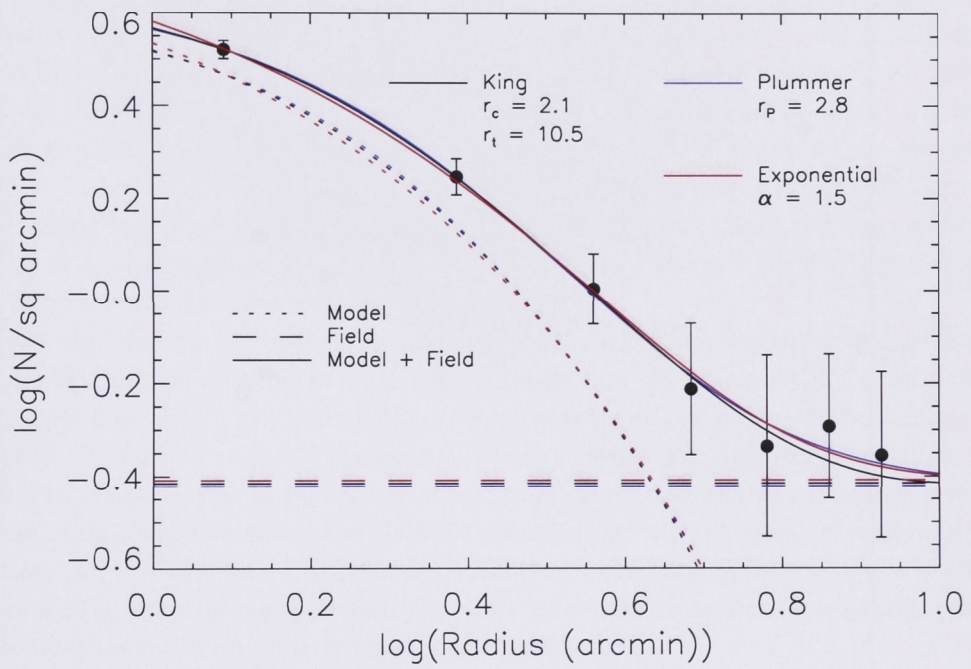


Fig. 6.4 — Fitted surface density profile of Boötes II consisting of a Plummer (blue), Exponential (red) or King (black) profile combined with a constant field contribution.

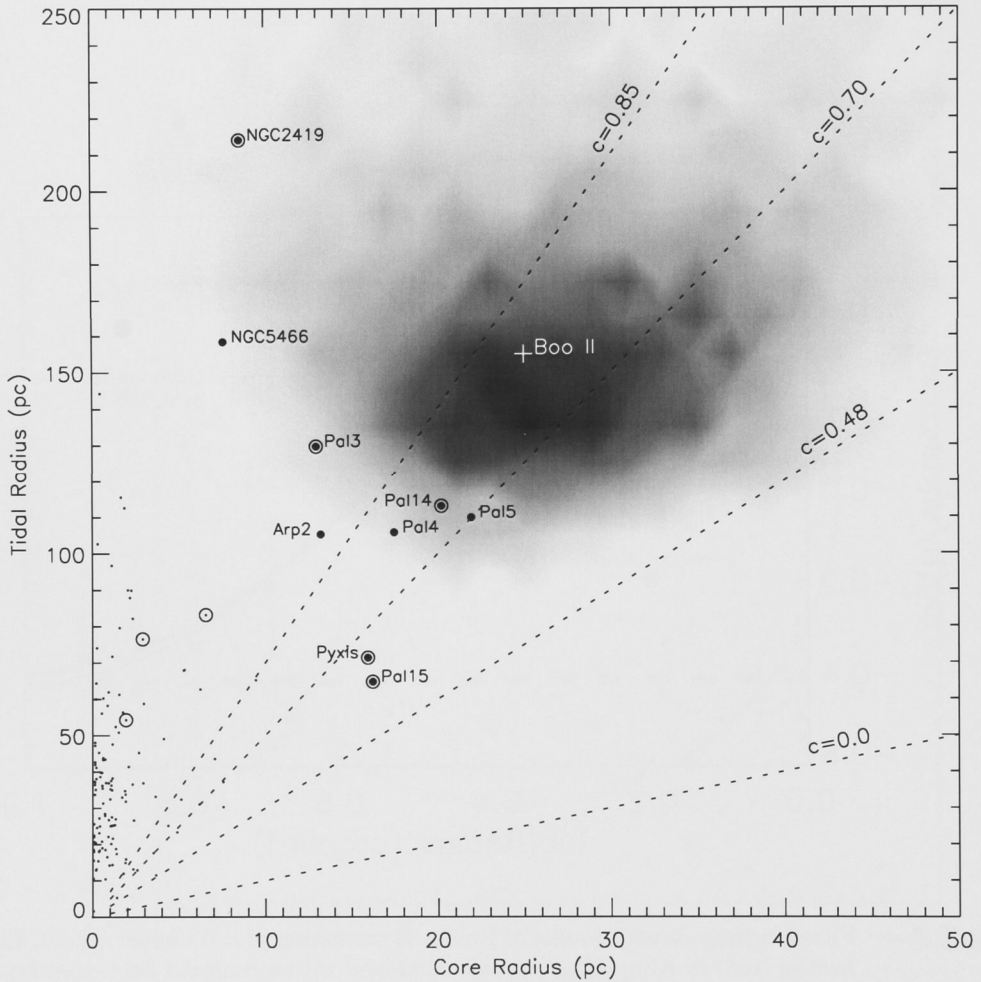


Fig. 6.5 — 2D Histogram of bootstrap results for Boötes II's King core radius and tidal radius with Galactic globular clusters (GGCs). GGCs having $r_c > 10pc$ or $r_t > 100pc$ are shown with larger points. Dashed lines show contours of constant concentration, defined as $c = \log(r_t/r_c)$. The open circles show the 8 globulars with $35 < d < 100$ kpc for which we calculate M/L in §6.4.3.

comes dominated by the brightest stars which may or may not be present simply from small number statistics. Hence, a group of stellar systems with an identical number of stars in each will have a spread in luminosity independent of any measurement uncertainty (see also Martin et al. (2008)). Using simulated dwarf galaxies from Walsh, Willman & Jerjen (*in prep*) we find that for an object such as Boötes II as observed by MMT/Megacam, this spread has a standard deviation of 0.6 magnitudes. We therefore combine this effect with the bootstrap uncertainty by summing in quadrature to derive the values presented in Table 6.1.

6.3.7 Morphology

We look for evidence of tidal disturbance based on the morphology of Boötes II's isodensity contours. Binning the positions of stars in Figure 6.3 into $0.01^\circ \times 0.01^\circ$ bins and spatially smoothing with a Gaussian of 1.5 arcmin FWHM scale length reveals an apparent distorted morphology to Boötes II, including substructure at the 3 - 5 σ level and an elongation directed along the gradient of the Galactic potential, as shown in Figure 6.6. Although tidal tails trace an object's orbit, tidal debris is stripped from an object along the gradient of the gravitational potential such that tidal stars near an object are expected to lie along this gradient. The elongation of Boötes II could thus be a feature resulting from tidal interaction.

However, due to the meager number of stars in Boo II, any observed irregular morphology may be an effect of small number statistics. To evaluate the significance of the morphology shown in Figure 6.6, we generate contour plots of bootstrap resamples of Boötes II stars. Figure 6.7 shows nine such randomly selected isodensity contours defined the same way as in Figure 6.6. This figure shows that the irregular morphology and apparent distortion along the Galactic potential are not persistent features. While this does not rule out tidal disturbance to Boötes II, the varying morphologies of these resampled objects demonstrates that the shape of Boötes II does not necessarily reflect a true irregularity in its underlying spatial distribution.

In order to quantify any asymmetry in the morphology of Boötes II, we first derive the position angle θ and ellipticity e . We calculate these from the standard SExtractor definitions (Bertin & Arnouts, 1996), using the smoothed images assuming that all pixels greater than 3σ above the mean are part of Boötes II. We then count the number of stars on either side of the major and minor axes, within $1.5r_h$. If the positions of these stars are drawn from an axisymmetric distribution, then the numbers on either side of an axis should be within $\sqrt{2\langle N \rangle}$ of each other. We define an asymmetry parameter A :

$$A = \frac{N_1 - N_2}{\sqrt{2\langle N \rangle}} \quad (6.6)$$

where N_1 and N_2 are the counts on either side of the axis and $\langle N \rangle$ is their average. Hence, for each bootstrap iteration we have two values of A , one for the major and one for the minor axis. Doing this for simulated Boo II-like objects drawn from a pure Plummer density profile expectedly yields a distribution of A with a mean of 0.0 and a

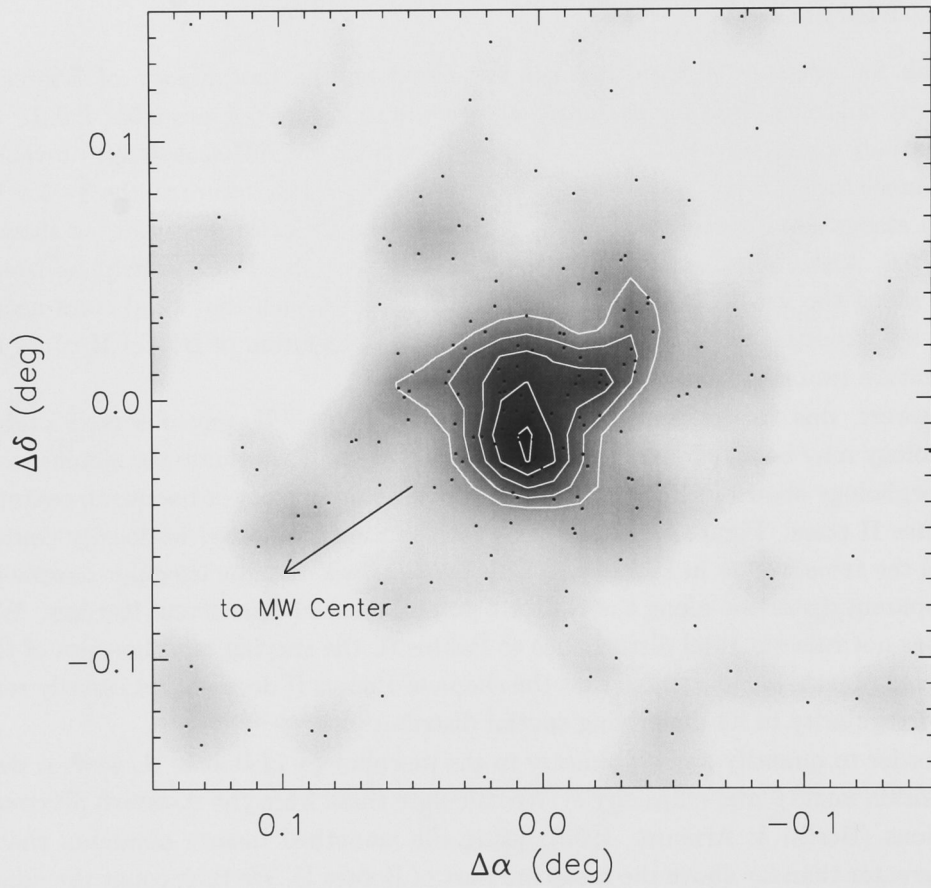


Fig. 6.6 — Smoothed contour plot of Boötes II showing an apparent distortion along the direction towards the Galactic Center. The contours show the 3,4,5 and 6 sigma levels above the mean.

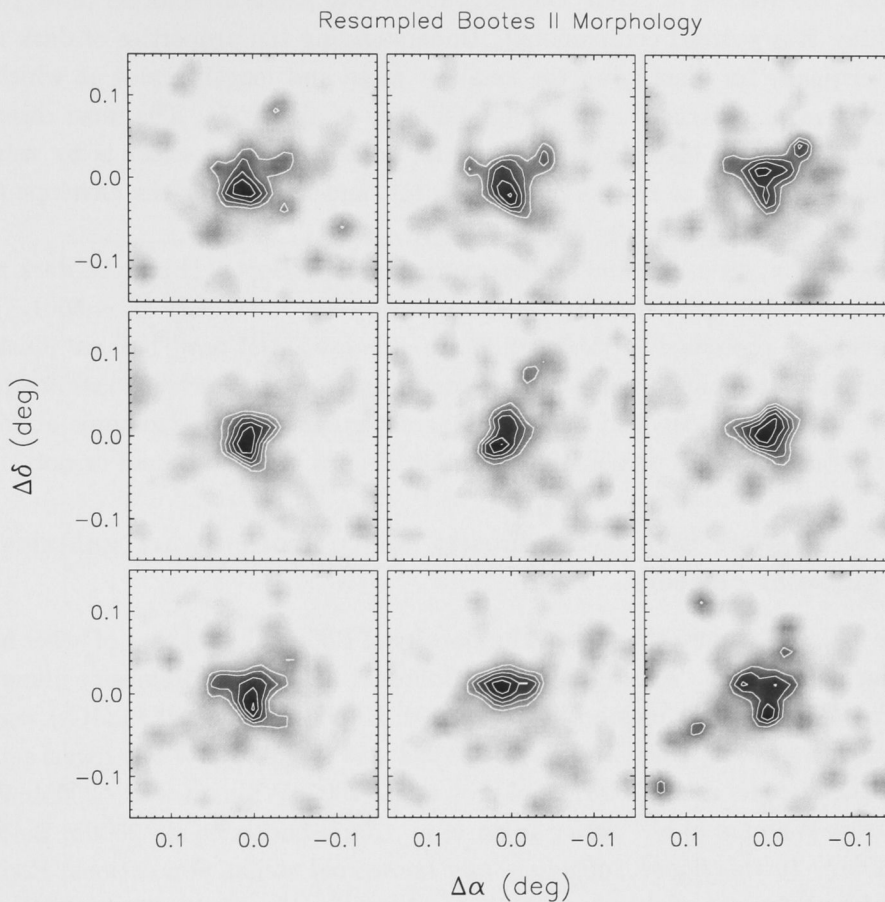


Fig. 6.7 — Smoothed contour plot of 9 randomly selected resamples of Boötes II stars, showing varying morphology for each iteration. The contours show the 3,4,5,6 and 7 sigma levels above the mean.

standard deviation of $\sigma_{sims} = 1.01$. The bootstrap yields two distributions with means of $A_{minor} = -0.23$ and $A_{major} = -0.18$ and standard deviations of $\sigma_{minor} = 1.03$ and $\sigma_{major} = 1.01$. The asymmetry of Boötes II is therefore not statistically significant.

These results imply that any apparent asymmetry in the distribution of Boötes II stars is well within that expected from a symmetric system, and is probably due to small number statistics. Deeper and wider-field imaging may provide the signal necessary to definitively measure whether Boötes II has extended, tidal structure.

6.4 Is Boötes II dark matter dominated?

As discussed in the Introduction, one motivation for studying an individual ultra-low luminosity object such as Boötes II in great detail is to determine whether it is a galaxy or a star cluster. Using our definition of a dwarf spheroidal galaxy, this boils down to determining whether or not the object is dark-matter dominated. (However,

for example, see Metz et al., 2007; Dabringhausen et al., 2008 for another interpretation of the Milky Way’s dwarf companions). Understanding the properties of dark matter depends critically on identifying the smallest mass and length scales at which dark matter clusters (e.g. Strigari et al., 2008; Gilmore et al., 2007). The most direct way we have at present to investigate dark matter on the smallest scales is by using the least luminous galaxies as tracers of dark matter, and by pushing the envelope to find the smallest galaxies possible to form.

In this section, we use a tidal argument to show why Boötes II may be dark matter dominated, and thus a dwarf galaxy, despite its very low luminosity ($L \sim 500L_{\odot}$). The lines of evidence presented in this section are circumstantial now, but are illustrative of arguments that could provide strong constraints on the correct classification for Boötes II, if deeper, wider-field imaging, kinematics, and/or spectroscopic abundance measurements are able to demonstrate whether Boötes II is self-bound or not.

6.4.1 Separation in size-luminosity space from dwarf galaxies and globular clusters

In Figure 6.8, we compare the size and luminosity of Boötes II with that of other nearby, old, stellar populations. This figure shows Boötes II in the size-luminosity plane along with Milky Way globular clusters (Harris, 1996; Koposov et al., 2007, GCs) and M31 (McConnachie & Irwin, 2006; Zucker et al., 2004, 2007) and Milky Way dwarf satellites (Mateo, 1998; Grebel et al., 2003; Belokurov et al., 2007; Willman et al., 2005b; Zucker et al., 2006a; Willman et al., 2005a; Irwin et al., 2007; Zucker et al., 2006b; Belokurov et al., 2006b). In this figure, including only known old stellar populations, Boötes II, Willman 1 and Segue 1 occupy a somewhat unique place in size-luminosity space. The apparent lack of objects with half-light radii larger than those of Boötes II, Willman 1 and Segue 1 but smaller than the apparent minimum size of confirmed dwarf galaxies (~ 100 pc) is quite possibly an observational selection effect due to the faint central surface brightnesses of objects in that region of the size-luminosity plane.

Conversely, Boötes II, Willman 1, and Segue 1 have half-light radii (20 – 40 pc) an order of magnitude larger than the half-light size characteristic of similarly low luminosity globular clusters ($-4 < M_V < -1$.) Low luminosity Milky Way clusters in that size gap could have been detected by the SDSS searches of Koposov et al. (2008) or Walsh, Willman & Jerjen (*in prep*). This gap between Boötes II, Willman 1 and Segue 1 and the known globular clusters is thus real and not a selection effect, suggesting that these objects are a distinct population from Milky Way GCs. However, if such diffuse old clusters do exist outside of the Milky Way, they would not yet have been discovered owing to their low surface brightnesses. It thus remains possible that old star clusters with properties bridging the gap between Boötes II and known GCs do exist in abundance in other environments.

Based on the compilation of Dias et al. (2002)*, only 2 of the 1076 Milky Way open clusters in that catalog with both distance and diameter measurements have apparent

*<http://www.astro.iag.usp.br/wilton/>

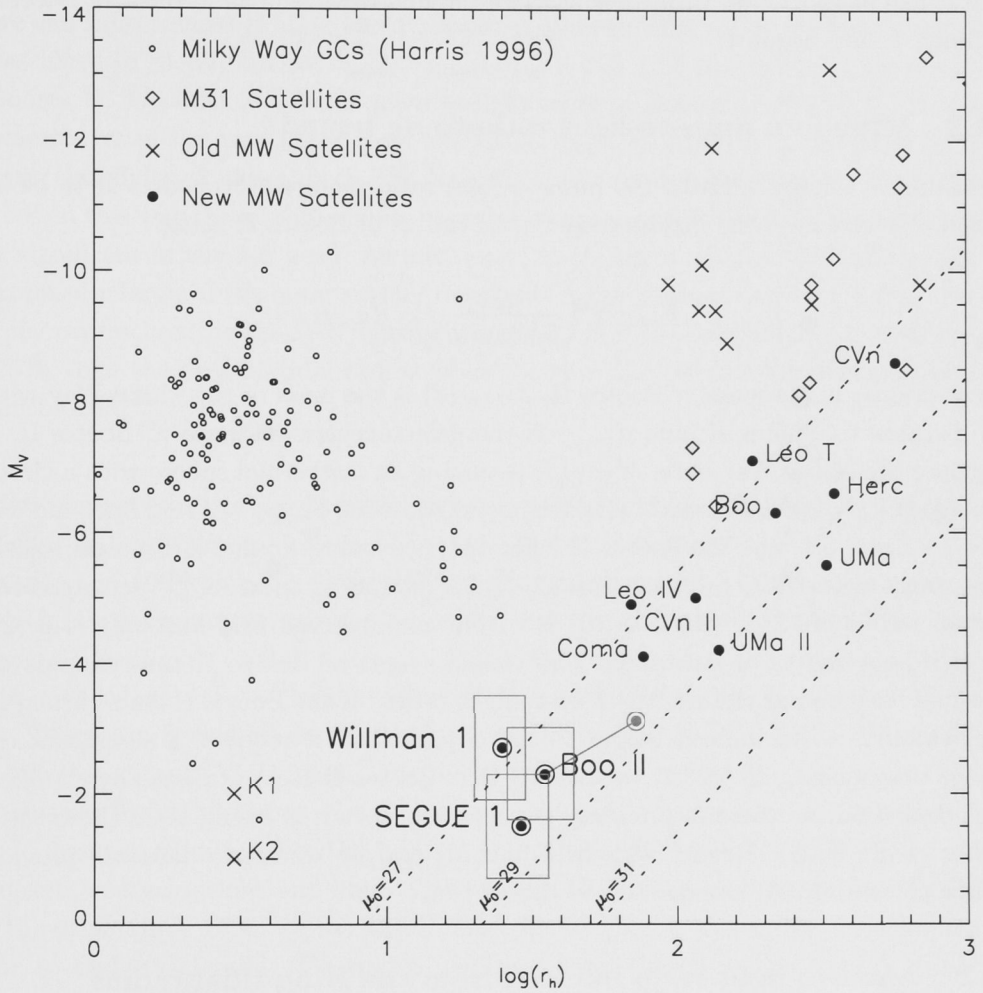


Fig. 6.8 — Size-luminosity plot of known Galactic satellites. The previous position of Boötes II is shown in grey along with the region bounded by the uncertainties in r_h and M_V . Values for the new Milky Way satellites are taken from Martin et al. (2008). Globular cluster properties are from Harris (1996). Dotted lines show lines of constant surface brightness.

radii larger than 20 pc. Young stellar associations in environments other than the Milky Way have been observed to have characteristic sizes of up to 100 pc (e.g. OB associations in the LMC observed by Gouliermis et al., 2003). Although the majority of these clusters appear to be unbound, some fraction of them could survive as self-bound entities for 10 Gyr if subject only to very weak tidal forces. We will show in §6.4.2 and 6.4.3, that tidal effects limit the survivability of objects at Boötes II distances with star cluster-like mass-to-light ratios and sizes and luminosities similar to those of Boötes II, Willman 1, and Segue 1.

6.4.2 Minimum mass-to-light ratio to be bound

We estimate a lower limit to the mass-to-light ratio required for Boötes II to be self-bound. We calculate the instantaneous tidal radius of Boötes II using:

$$r_{\text{tidal}} \propto \left(\frac{m_{\text{BooII}}}{3M_{\text{MW}}(d)} \right)^{\frac{1}{3}} d_{\text{BooII}}, \quad (6.7)$$

where m_{BooII} is the mass of Boötes II, $M_{\text{MW}}(d)$ is the mass of the Milky Way within the distance to Boötes II, and d_{BooII} is the galactocentric distance to Boötes II. We calculate the Milky Way mass $M_{\text{MW}}(d)$ assuming an isothermal sphere with a circular velocity of $V_c = 220 \pm 40 \text{ km s}^{-1}$ (Bellazzini, 2004), using $d_{\text{BooII}} = 42 \pm 2 \text{ kpc}$, and using $M_V = -2.4 \pm 0.7 \text{ mag}$ for Boötes II. For $(M/L)_V$ values of 2, 10, 100 and 1000 kpc the corresponding tidal radii are thus 42^{+19}_{-13} , 72^{+33}_{-21} , 156^{+70}_{-46} and 336^{+151}_{-99} pc respectively. A tidal radius of 72 pc ($M/L = 10$) is within our observed field and only ~ 2 times the half-light radius of Boötes II. The visible extent of Boötes II thus exceeds that expected for globular cluster-like mass-to-light ratios. If the Boötes II stars throughout our field-of-view are indeed bound to the object, then it requires a significant dark matter component. In §6.3.7, we showed that Boötes II lacks statistically significant tidal distortion, so there is presently no evidence that it is losing stars (however see Muñoz et al., 2008). Deeper wide-field imaging and/or kinematic data will provide a clearer picture of the boundedness of this object.

6.4.3 Mass-to-light ratio inferred from the King tidal radius

Using the same physical principle as in the previous section, we now calculate the mass-to-light ratio of Boötes II assuming that the King tidal radius derived in §6.3.5 is the true tidal radius of Boötes II, owing to the tidal field of the Milky Way. The King model (King, 1966) is physically motivated and expected for a relaxed, single mass component, spherical system in equilibrium that is tidally limited by the gravitational field of the Milky Way. For velocity dispersions greater than 0.1 km/sec, the relaxation time of Boötes II is less than a Hubble time (unlike the classical Milky Way dSphs). Based on a Dotter et al. (2008) stellar luminosity function for a 13 Gyr, $[\text{Fe}/\text{H}] = -2$ system normalized to have $M_V = -2.4 \text{ mag}$, Boötes II has 3700 stars more massive than $0.1 M_{\text{Sun}}$. Its relaxation time ($t_{\text{relax}} \sim N/8 \ln(N) * t_{\text{cross}}$; Binney & Tremaine, 1987) at

its Plummer half-light radius of 36 pc is thus $\sim 1.1 \text{ Gyr}/\sigma_v$, where σ is its 1D velocity dispersion. Although the presence of a significant dark component of matter would complicate the expected relaxation time of Boötes II, we are testing the hypothesis that it does not contain dark matter.

If we take the King “tidal radius” to be the instantaneous tidal radius of Boötes II, we can infer a mass m_{BooII} and therefore a mass-to-light ratio. We use Equation 7 as described in §6.4.2, but set $r_{tidal} = r_{tidal,King} = 155 \pm 35$ pc, and solve for the mass of Boötes II. We infer a V-band mass-to-light ratio of Boötes II of 98_{-84}^{+420} . If this is representative of the true $(M/L)_V$ of Boötes II, its mass would be dominated by dark matter, classifying it as a galaxy. We note the substantial uncertainty on the $(M/L)_V$ derived in this way. Even if the input assumptions are robust, the dark matter signal is only significant at the $1\text{-}\sigma$ level. As mentioned in §6.3.5, the King tidal radius may be substantially larger if the outer surface density bins are contaminated with Boo II stars thereby overestimating the field density. As in §6.3.5, if the field value is overestimated by 25%, then the best fit tidal radius would be $r_t = 215$ pc and the inferred $(M/L)_V$ would be 263_{-216}^{+991} .

For comparison, we use these same assumptions and same technique to calculate the mass-to-light ratios of known Milky Way globular clusters in the distance range of $35 \leq R_{GC} \leq 100$ kpc. We chose this distance range because i) these halo globulars reside in an environment and are on orbits that are the most comparable to Boötes II, and ii) Bellazzini (2004) states the Milky Way mass profile is consistent with an isothermal sphere with a circular velocity of $V_c = 220 \pm 40 \text{ kms}^{-1}$ between 35 – 100 kpc. There are 8 clusters in that range: Eridanus, Pal 2, NGC 2419, Pyxis, Pal 3, Pal 14, Pal 15 and NGC 7006. For all of these clusters, we use the distances and luminosities from the Harris (1996) catalog, and assign a distance uncertainty of 0.1 mag in distance modulus. For Pal 2, NGC 2419, Pal 3, Pal 14 and NGC 7006 we use the core radii, concentrations and uncertainties from McLaughlin & van der Marel (2005). For the other three GCs, we use values from Harris (1996) and assign uncertainties of 10 pc to their tidal radii. We find a median (mean) $(M/L)_V$ of $0.36_{-0.12}^{+0.98}$ ($0.5_{-0.38}^{+1.85}$) for these eight clusters. The single outlier with a calculated $(M/L)_V > 1$ is Pal 14 with $(M/L)_V = 2.4_{-1.9}^{+10.4}$. Although the true $(M/L)_V$ of most (all) of these eight halo globulars is within 1σ (2σ) of the calculated values, we find that this technique systematically underestimates of the $(M/L)_V$ of these relaxed systems by up to an order of magnitude (3 of the eight GCs have inferred $M/L < 0.1$). This systematic underestimate is not surprising, because the tidal forces experienced by these halo globulars at this snapshot in time are smaller than the maximum tidal force that they have experienced in their past. Using their present distance in this M/L calculation will thus provide a lower limit on the masses required to yield the observed King tidal radii. Regardless, this calculation shows that Boötes II is an outlier from globular clusters with this metric of measurement.

6.5 Conclusion

In this paper, we use MMT/MegaCam imaging in g and r to present the first robust estimates of the fundamental properties of the ultra-low luminosity Milky Way satellite Boötes II ($d \sim 42$ kpc). This object is old and its stellar population appears very similar to that of M92, showing that it is metal-poor ($[\text{Fe}/\text{H}] < -2$). With a total luminosity of only ~ 500 solar luminosities ($M_V \sim -2.4 \pm 0.7$ mag) and a half-light size of $\sim 36 \pm 9$ pc (assuming a Plummer profile), Boötes II lies away from globular clusters and dwarf spheroidals, but near Willman 1 and Segue 1, in size-luminosity space. We showed that although the morphology of Boötes II appears irregular and elongated along the direction of the Galactic potential, that this distortion of its isodensity contours is not statistically significant in our dataset.

The revised values we present for the distance, luminosity, and physical size of Boötes II differ from those originally estimated in the Walsh et al. (2007) discovery paper. The primary factor in these differences is the new distance estimate is 42 kpc rather than 60 kpc. The SDSS discovery data was more than two magnitudes shallower than the data presented in this paper. VLT photometry of Boötes II will be presented in Jerjen et al. (*in prep.*) along with a more detailed discussion of its stellar population and of the possible association, or lack thereof, with the Sagittarius Stream.

Our bootstrap analysis demonstrated the impact of small number statistics on the derived parameters for this ultra-faint class of objects, but showed that despite large uncertainties Boötes II has a size that makes it distinct from Milky Way GCs, although its King concentration is similar to that of Milky Way dwarf galaxies as well as to some diffuse GCs.

The gap between Boötes II, Willman 1, and Segue 1 and Milky Way globular clusters in size-luminosity space is not a selection effect because existing surveys would have been sensitive to such objects. However, the apparent separation in half-light size at 100 pc between dSphs and Boötes II, Willman 1, and Segue 1 could be a selection effect, making it more likely that these three objects are fundamentally connected with the dwarf galaxy population. We pointed out that old star clusters filling in that apparent gap may exist in environments other than the Milky Way, but would have escaped detection owing to their low surface brightnesses.

If Boötes II is a self-bound system in equilibrium, it could represent the continuation of the dwarf galaxy population into the extreme low luminosity regime. We showed that it is reasonable to believe that Boötes II is a relaxed system, and used its King tidal radius to infer a lower limit M/L of $\sim 98_{-84}^{+420}$. Dropping the assumption that the King tidal radius is physically meaningful for Boötes II, its spatial extent is larger than that naively expected for globular cluster-like mass-to-light ratios, if it is self-bound. However, we cannot rule out that it is a low M/L star cluster that is undergoing tidal disruption or disturbance, much like the Pal 5 cluster.

Regardless of whether or not Boötes II is dark matter dominated, it can provide a unique laboratory with which to investigate the low surface density limit of star formation and the tidal field of our Galaxy. The study in this paper also provides a partial

Table 6.1. Boötes II Properties from MMT/Megacam

Parameter	Measured	Uncertainty	bootstrap median
RA (h m s)	13 58 05.1	± 7.2 s	13 58 04.3
Dec (d m s)	+12 51 31	± 23 ''	+12 51 09
(l, b)	(353.75, 68.86)	-	-
($m - M$)	18.1	± 0.06	18.1
Distance	42 kpc	± 1.6 kpc	42 kpc
r_h (Pl)	2.8 arcmin	± 0.7	2.8 arcmin
r_h (ex)	2.5 arcmin	± 0.8	2.6 arcmin
r_h (Pl)	35 pc	± 9	36 pc
r_h (ex)	31 pc	± 10	33 pc
M_V (Pl)	-2.3	± 0.7	-2.4
M_V (ex)	-2.2	± 0.7	-2.2
$\mu_{0,V}$ (Pl)	27.76 mag arcsec ⁻²	± 0.31	27.93 mag arcsec ⁻²
$\mu_{0,V}$ (ex)	27.70 mag arcsec ⁻²	± 0.33	27.90 mag arcsec ⁻²
r_c	25 pc	± 9	25 pc
r_t	127 pc	± 35	155 pc
θ	-33°	± 57 °	-28.5°
e	0.27	± 0.15	0.34
A_{major}	-	± 1.01	-0.26
A_{minor}	-	± 1.03	-0.33

road map for the future study of numerous similar objects that may be discovered in upcoming surveys for Galactic satellites to greater depth (e.g. PanSTARRS, Kaiser, 2004) or in previously unsearched sky (e.g. Skymapper, Keller et al., 2007 and Walsh et al. *in prep.*). Ultimately, determining the boundedness of its stars will be needed to definitively pin down the nature of the peculiar Boötes II object.

ACKNOWLEDGEMENTS

We thank the anonymous referee for improving this manuscript. We thank Bill Wyatt for maintaining a local copy of the SDSS data products at the Harvard-Smithsonian Center for Astrophysics. Jay Strader shared his transformations of the Clem (2007) isochrones used in this paper, as well as provided helpful conversations. We thank Brian McLeod for providing guidance and troubleshooting during our observing runs, writing software that our reduction relied on, and advising our MegaCam reduction. We thank Matt Ashby for creating the MegaCam reduction manual and for advising our reduction. We thank Maureen Conroy for troubleshooting during our observing runs, and for helping to create weight maps and performing a preliminary co-addition of our Boötes II images. Mike Alegria, John McAfee, and Ale Milone provided observational support during our observing runs. Observations reported here were obtained at the

MMT Observatory, a joint facility of the Smithsonian Institution and the University of Arizona. SW acknowledges partial financial support from the Australian Research Council Discovery Project Grant DP0451426.

Chapter 7

Conclusion and Future Directions

*So to borrow a phrase from the ancient
philosopher Clarksonius, 4th Century BC;
“how hard can it be?”*

–James May

In the three year duration of this thesis, 13 dwarf spheroidal satellites of the Milky Way were discovered in the Sloan Digital Sky Survey, almost doubling the number known to science prior to 2005. The spatial distribution of these satellites and their luminosity/mass function are critical tests to the success of Λ CDM and galaxy formation in general. The sky beyond SDSS almost certainly contains many more to be discovered, and a search of the entire southern sky is the overarching goal of the work presented in this thesis.

An algorithm was developed to search photometric catalogs for statistically significant overdensities of old, metal poor stars at fixed distances. The long term goal of the project is the Stromlo Missing Satellites Survey using the SkyMapper telescope (Keller et al., 2007). The data product of this telescope will be a multi-band, multi-epoch photometric catalog of comparable depth and design as SDSS. As such, the algorithm presented here was developed using, and tested on, the publicly available Data Release 6 of SDSS (Adelman-McCarthy et al., 2008).

Stars within the catalog are subject to a color-magnitude selection cut in r and $g-r$, dependent upon the distance range being probed. The sky position of stars remaining after this cut are smoothed using a kernel defined by a Plummer surface density profile, with a fixed 4.5 arcmin scale-length chosen to maximise sensitivity to both compact and extended angular dwarf sizes. To cope with stellar gradients across a field, and non-gaussianity in regions of very low density, thresholds are defined as functions of the average density of the post-selection cut sources over a $0.9^\circ \times 0.9^\circ$ window. Any regions of the spatially smoothed positions that have a single pixel value above 1.75 times above the corresponding threshold pixel, or spatially smoothed regions larger than 60.0 square arcmin that are contiguously greater than 1.0 times the corresponding pixels constitutes a detection.

Applying this technique to DR6 yields detections of 21 Milky Way/Local Group dwarfs: The “classical” dwarfs Draco, Leo, Leo II, Leo A, Sextans and Peg DIG, and the 15 new satellites discovered in SDSS using similar techniques. One of these 15 new satellites is Boötes II, discovered during the course of development of this algorithm. The discovery letter of Boötes II is presented in Chapter 5. In addition the desired detections of dwarf galaxies, the algorithm also detected 17 globular clusters, 2 open clusters, 28 giant galaxies external to the Local Group and 4 galaxy clusters. The remaining 30 detections do not correspond to catalog objects and may be new dwarfs. Deep imaging will be required to confirm or rule out these candidates.

The biggest benefit of conducting a search using a uniform photometric survey such as SDSS is that the detection limits can be carefully quantified in order to be able to draw conclusions from the number of detections. To accomplish this more than 3,800,000 model galaxies were simulated, embedded in randomly generated fields and put through the detection algorithm. The photometry of these model satellites was generated from sampling a composite catalog of HST photometry of the Draco, Carina, and Ursa Minor dwarfs, and positions were taken from a Plummer surface density profile. Field photometry was taken from stars randomly drawn from the desired galactic latitude in DR6, and their positions distributed randomly. Each galaxy was assigned a luminosity, size, distance, and galactic latitude to model the detection limits as functions of these parameters.

While the resulting detection efficiency maps are complicated, they illustrate several important points. Within 300 kpc, all satellites brighter than $M_V \approx -6.5$ in the DR6 footprint should have been detected. Galactic latitude was also expected to play an important role in the detectability of dwarfs, but results show that this is not the case and dwarfs could have been detected in SDSS quality catalogs as low as $b \approx 15^\circ$. Several simplified parameterizations of detection limits were presented to facilitate comparison with theory. Using the results of the detectability of known dwarfs and assuming a Via Lactea subhalo radial profile, the total number of MW satellites was estimated to be between 52 and 340, meaning at least a substantial fraction remain to be discovered.

The final chapters of this thesis detail the discovery of Boötes II and how its properties were estimated from the initial SDSS data, as well as with follow up observations using MMT/Megacam. The new satellites discovered in SDSS are resolved into stars, and the total luminosity of the faintest of these satellites is comparable to that of a single red giant. Given the sparsity of stars, small number statistics is a huge influence and needs to be accounted for when inferring properties from the observations. This is of particular importance to Boötes II, which lies in an uncertain region of size-luminosity space, confusing its classification as either a dwarf spheroidal or globular cluster. Several arguments are presented in Chapter 6 that sway interpretation in favor of dSph, although the possibility of a massively disrupting globular cluster cannot be ruled out. The nature of Boötes II, along with Segue 1 and Willman 1, has profound implications on the extrapolated census of MW satellites. If these objects are not embedded in dark matter halos, then virtually all satellites within DR6 have been discovered. If they are indeed dark matter dominated, then many more of these objects may lie undetectable

beyond 50 kpc, substantially increasing the inferred total number of MW satellites. Understanding these objects is therefore critical to the comparison of Λ CDM simulations with observations.

7.1 The Future

The application of the detection algorithm to SDSS DR6 yielded 30 unidentified detections of significant point source overdensities. While some of these may be due to the misclassification of faint cluster galaxies as stars, some may be new MW dwarfs. By stacking the SDSS images in the u , g , r and i bands the signal to noise of the sources can be increased, and better star/galaxy identification achieved using Source Extractor. For 28 of the 30 detections, when sources with $< 80\%$ probability of being a star are removed, the overdensity remains, meaning that they are most likely real stellar overdensities. The varied CMDs of these regions are not all consistent with that of a dSph, and these may be the result of open clusters, clumps within stellar streams, or unbound tidal debris. Identifying the nature of these detections will be important for the expectations of future surveys, as well being in the interest of reducing unnecessary observations in the event of re-detection by independent studies.

Proposals for follow up imaging and spectroscopy are being prepared and will be submitted to various Northern hemisphere telescopes. The confirmation of Leo V (Belokurov et al., 2008) shows that DR6 may not yet have run dry, and the nature of these unidentified detections needs to be accounted for, dSph or not. As was demonstrated with Boötes II, estimating even the most basic parameters of these extremely faint systems can be challenging, and this will only worsen with weaker detections.

The number of discoveries using SDSS shows that SkyMapper is almost guaranteed to once again double the number of known MW satellites once it has observed the entire southern sky. This new census will be quantified better than ever and should allow truly conclusive comparison of observations with theoretical predictions; the substructure problem may be quantifiably and conclusively reassessed. Populating the ambiguous region of size-luminosity space will help to pin down the nature of the objects Boötes II, Willman 1 and Segue 1 by revealing whether or not they are a continuation of the dSph distribution or a distinct population. In addition to the discovery of discrete satellites, SkyMapper will fill in missing pieces of the many stellar streams and will likely uncover new ones, adding to the Milky Way fossil record. Future missions such as Pan-STARRS, LSST and GAIA will probe to much greater distances and may even allow us to observe the faint end of the galaxy luminosity function.

Appendix A

Candidate Satellite Detections

The following are the 30 detections above the thresholds in Figure 2.5 that do not correspond to any catalogued object. Proposals are being submitted for followup time and as such coordinates are not disclosed here. Each detection is flagged with a letter based purely on the appearance of the SDSS image at that position. **X** denotes a detection that it almost certainly a background galaxy cluster, but may also be an extremely bright star or other obvious contaminant. **O** are objects that do not have a substantial number of visible background galaxies and may be dwarf satellites, and **G** are objects that have pristine background images and should be a true stellar overdensity, but not necessarily a dSph satellite. No judgement has been made regarding the signal strength or CMD appearance of these detections.

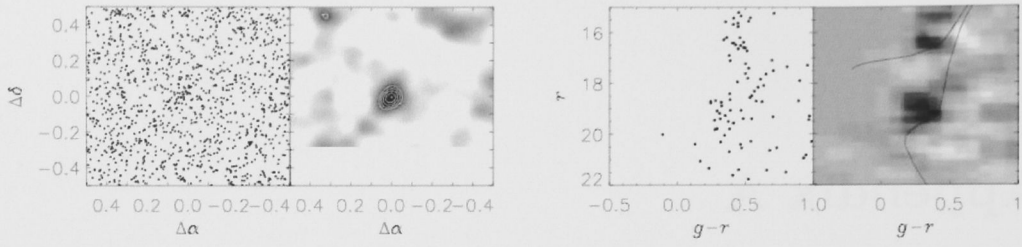


Fig. A.1 — O

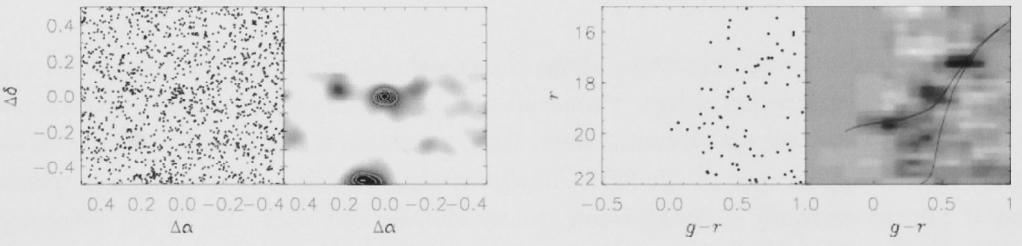


Fig. A.2 — G

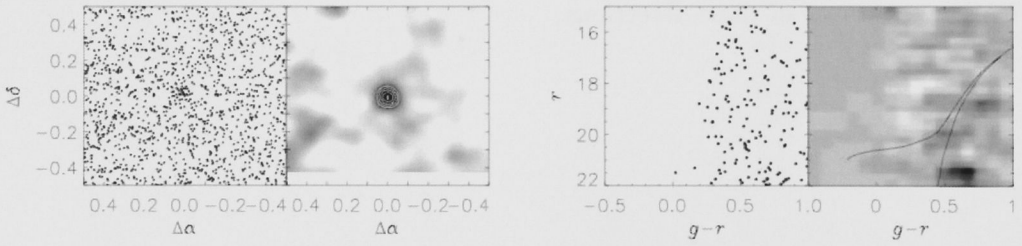


Fig. A.3 — G

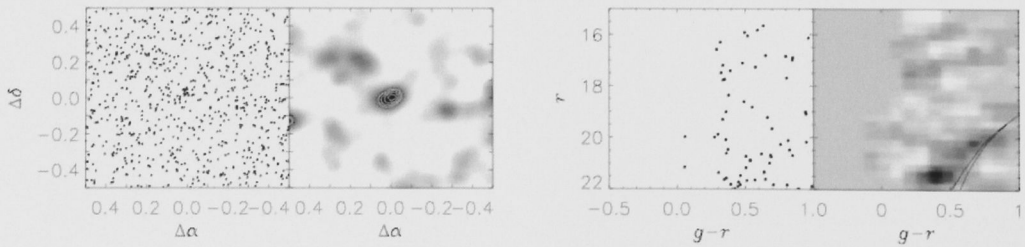


Fig. A.4 — O/G

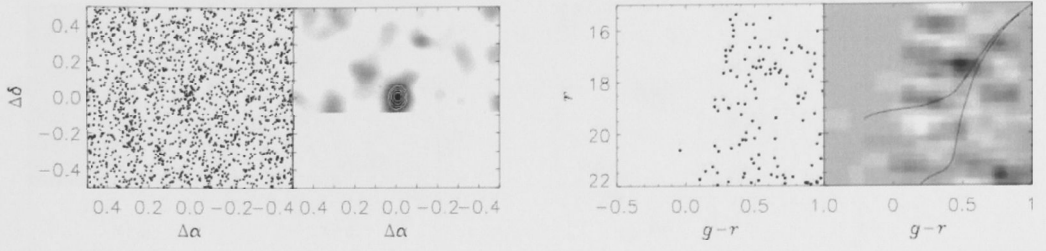


Fig. A.5 — O

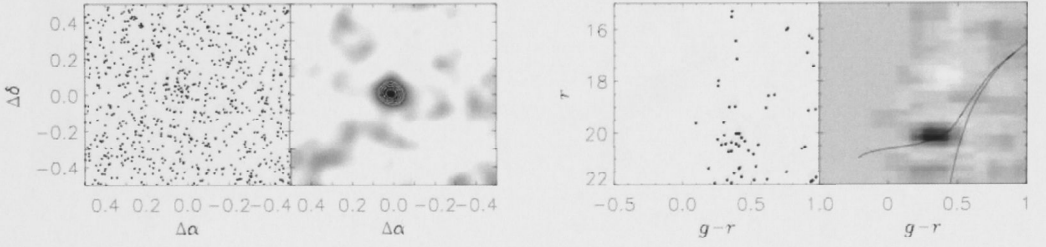


Fig. A.6 — X

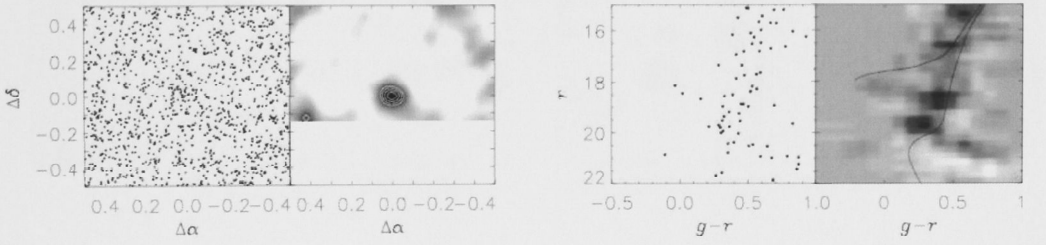


Fig. A.7 — O

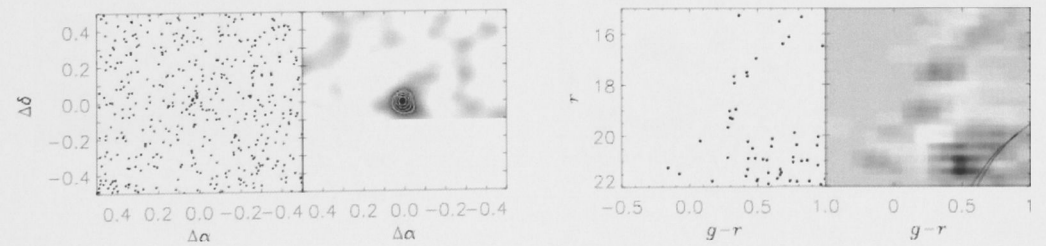


Fig. A.8 — X

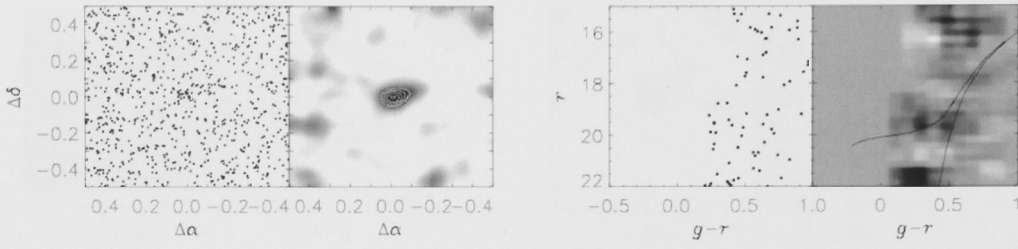


Fig. A.9 — X

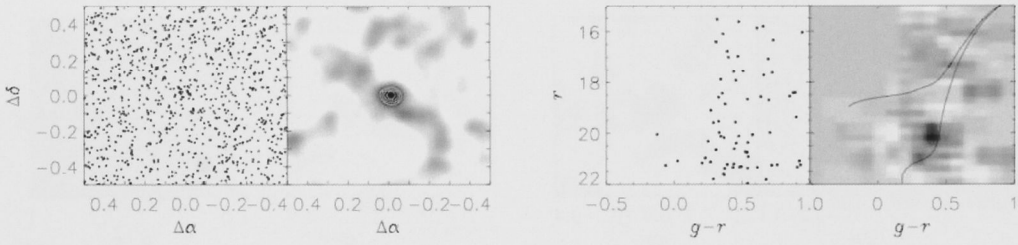


Fig. A.10 — X

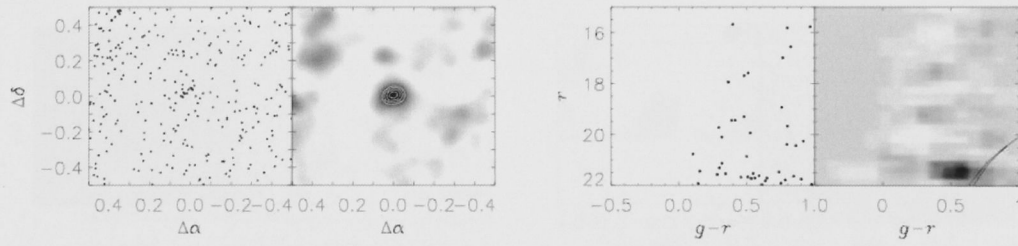


Fig. A.11 — X

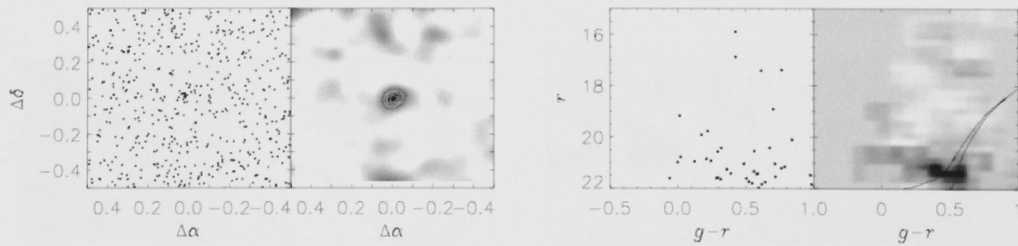


Fig. A.12 — X

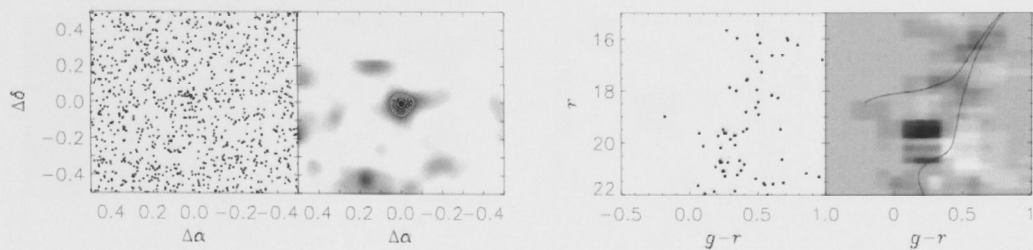


Fig. A.13 — X/O

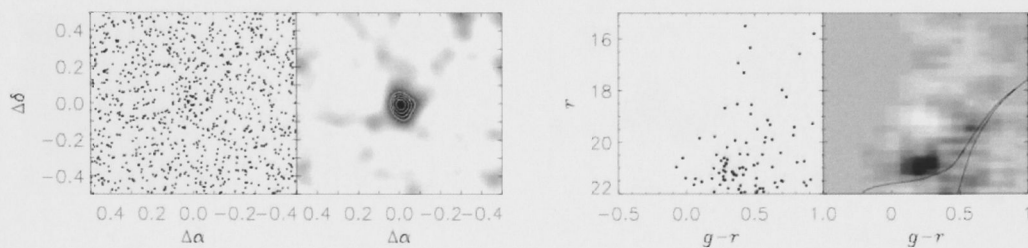


Fig. A.14 — X

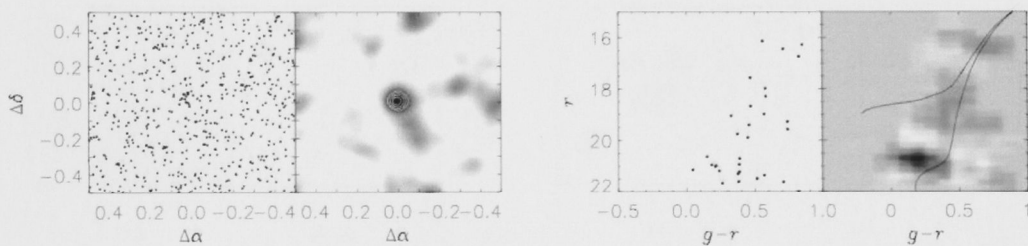


Fig. A.15 — O

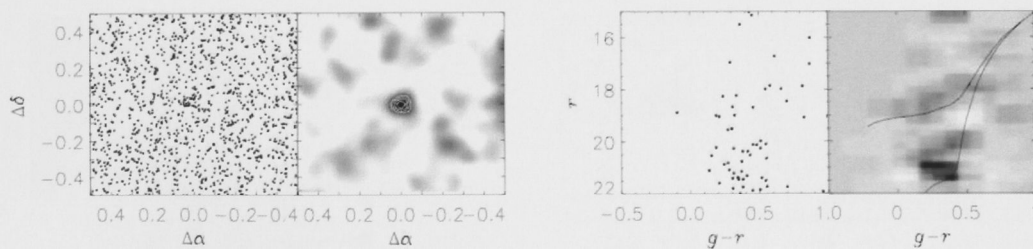


Fig. A.16 — X/O

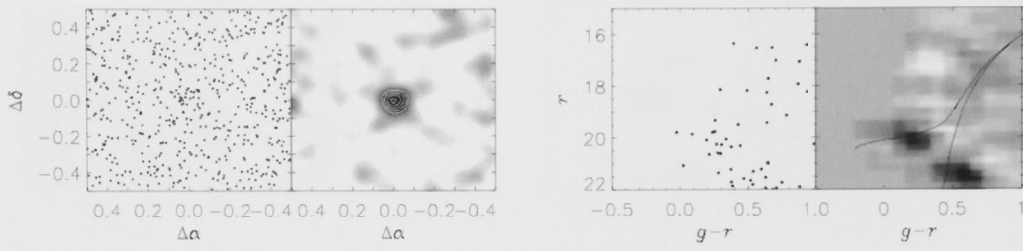


Fig. A.17 — O - "UMa X"

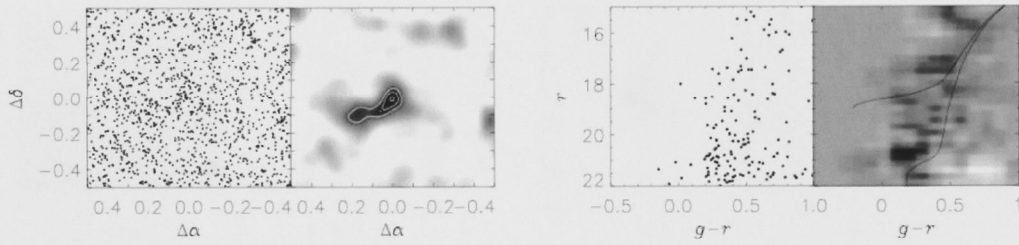


Fig. A.18 — O - "Vir Z"

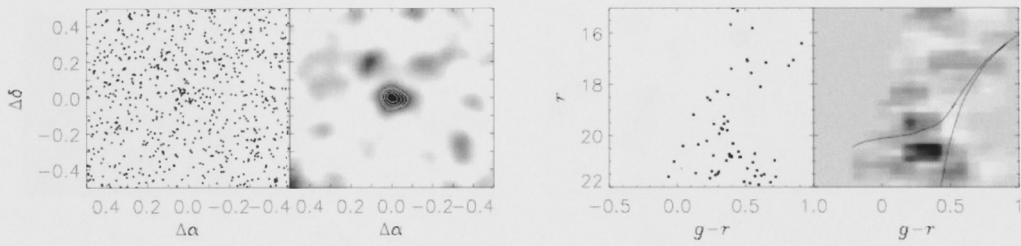


Fig. A.19 — X/O

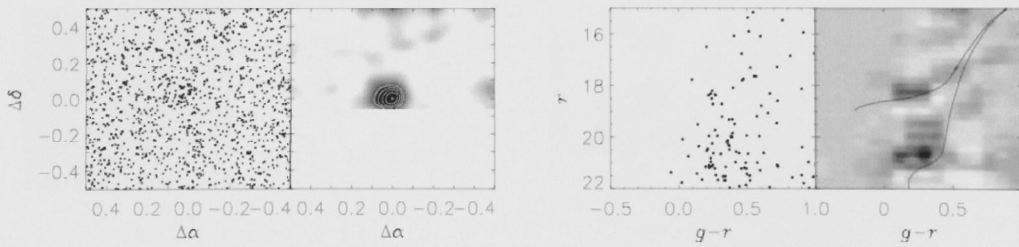


Fig. A.20 — X

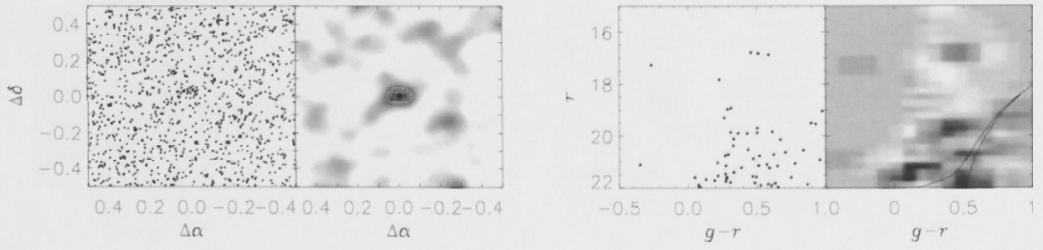


Fig. A.21 — O

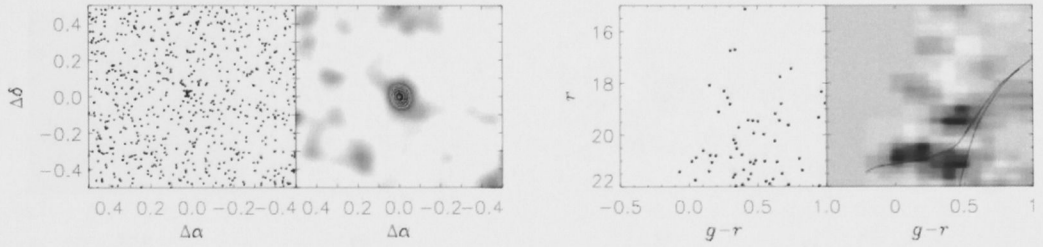


Fig. A.22 — GGG - "CVn W"

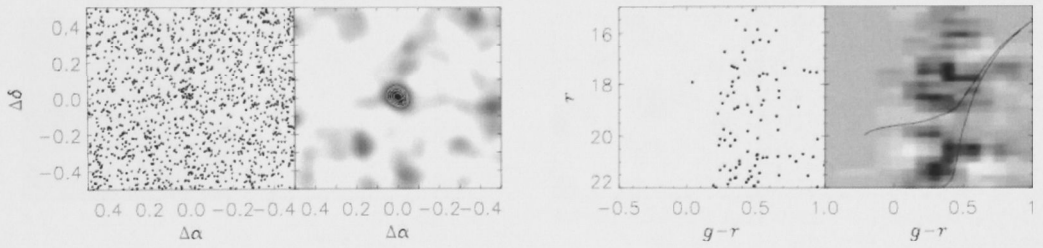


Fig. A.23 — O

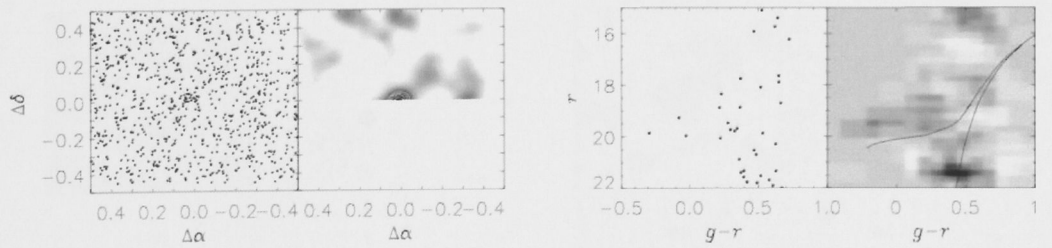


Fig. A.24 — O

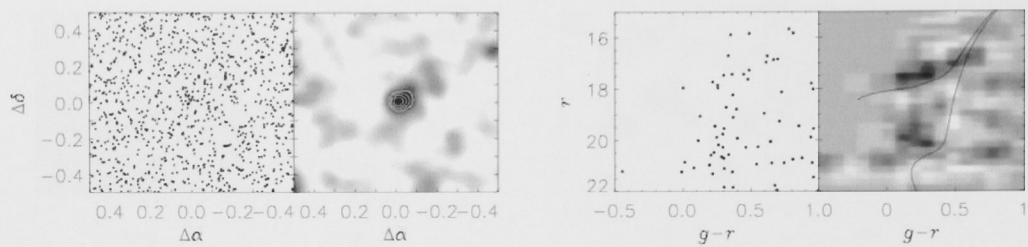


Fig. A.25 — O

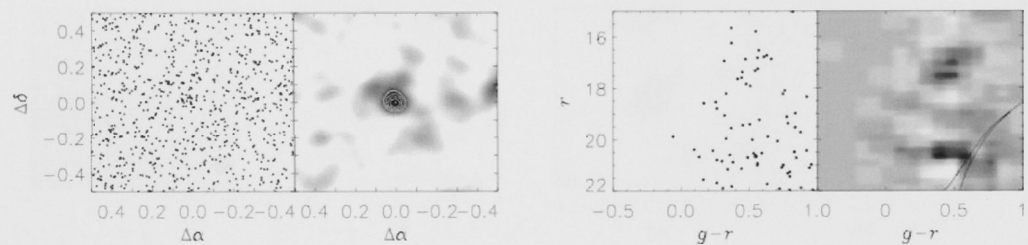


Fig. A.26 — O

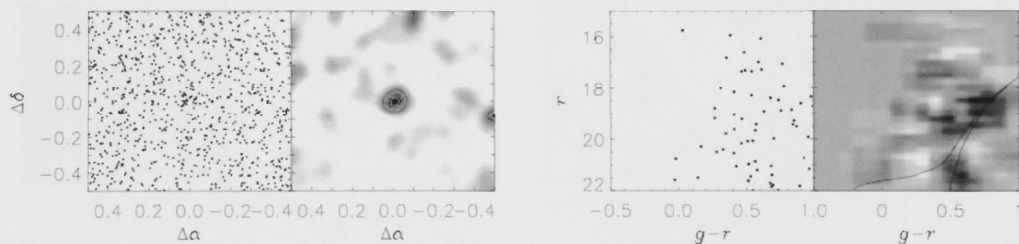


Fig. A.27 — O

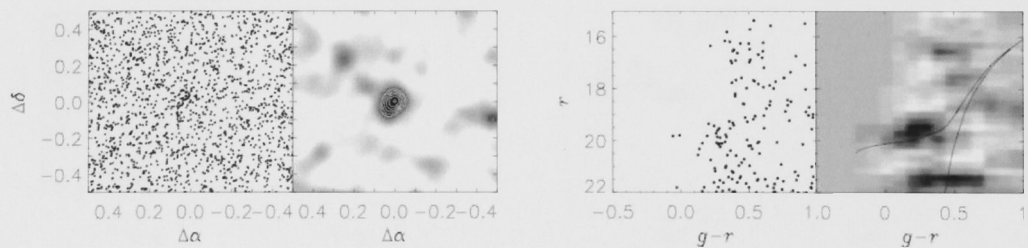


Fig. A.28 — G - "Her X"

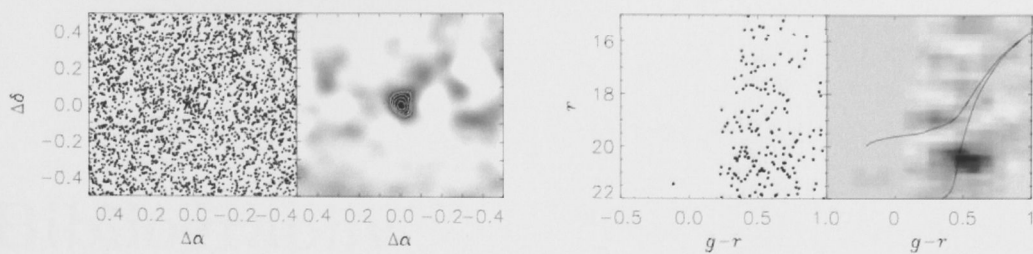


Fig. A.29 — O/G

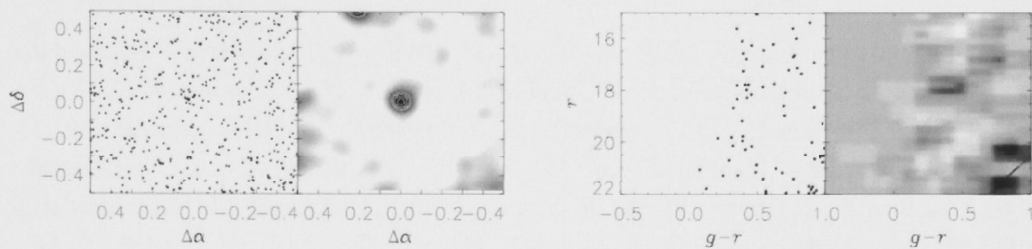


Fig. A.30 — X/O

Bibliography

Abdelqader, M., & Melia, F. 2008, MNRAS, 388, 1869

Adelman-McCarthy, J. K., Agüeros, M. A., Allam, S. S., Allende Prieto, C., Anderson, K. S. J., Anderson, S. F., Annis, J., Bahcall, N. A., Bailer-Jones, C. A. L., Baldry, I. K., Barentine, J. C., Bassett, B. A., Becker, A. C., Beers, T. C., Bell, E. F., Berlind, A. A., Bernardi, M., Blanton, M. R., Bochanski, J. J., Boroski, W. N., Brinchmann, J., Brinkmann, J., Brunner, R. J., Budavári, T., Carliles, S., Carr, M. A., Castander, F. J., Cinabro, D., Cool, R. J., Covey, K. R., Csabai, I., Cunha, C. E., Davenport, J. R. A., Dilday, B., Doi, M., Eisenstein, D. J., Evans, M. L., Fan, X., Finkbeiner, D. P., Friedman, S. D., Frieman, J. A., Fukugita, M., Gänsicke, B. T., Gates, E., Gillespie, B., Glazebrook, K., Gray, J., Grebel, E. K., Gunn, J. E., Gurbani, V. K., Hall, P. B., Harding, P., Harvanek, M., Hawley, S. L., Hayes, J., Heckman, T. M., Hendry, J. S., Hindsley, R. B., Hirata, C. M., Hogan, C. J., Hogg, D. W., Hyde, J. B., Ichikawa, S.-i., Ivezić, Ž., Jester, S., Johnson, J. A., Jorgensen, A. M., Jurić, M., Kent, S. M., Kessler, R., Kleinman, S. J., Knapp, G. R., Kron, R. G., Krzesinski, J., Kuropatkin, N., Lamb, D. Q., Lampeitl, H., Lebedeva, S., Lee, Y. S., Leger, R. F., Lépine, S., Lima, M., Lin, H., Long, D. C., Loomis, C. P., Loveday, J., Lupton, R. H., Malanushenko, O., Malanushenko, V., Mandelbaum, R., Margon, B., Marriner, J. P., Martínez-Delgado, D., Matsubara, T., McGehee, P. M., McKay, T. A., Meiksin, A., Morrison, H. L., Munn, J. A., Nakajima, R., Neilsen, Jr., E. H., Newberg, H. J., Nichol, R. C., Nicinski, T., Nieto-Santisteban, M., Nitta, A., Okamura, S., Owen, R., Oyaizu, H., Padmanabhan, N., Pan, K., Park, C., Peoples, J. J., Pier, J. R., Pope, A. C., Purger, N., Raddick, M. J., Re Fiorentin, P., Richards, G. T., Richmond, M. W., Riess, A. G., Rix, H.-W., Rockosi, C. M., Sako, M., Schlegel, D. J., Schneider, D. P., Schreiber, M. R., Schwobe, A. D., Seljak, U., Sesar, B., Sheldon, E., Shimasaku, K., Sivarani, T., Smith, J. A., Snedden, S. A., Steinmetz, M., Strauss, M. A., SubbaRao, M., Suto, Y., Szalay, A. S., Szapudi, I., Szkody, P., Tegmark, M., Thakar, A. R., Tremonti, C. A., Tucker, D. L., Uomoto, A., Vanden Berk, D. E., Vandenberg, J., Vidrih, S., Vogeley, M. S., Voges, W., Vogt, N. P., Wadadekar, Y., Weinberg, D. H., West, A. A., White, S. D. M., Wilhite, B. C., Yanny, B., Yocum, D. R., York, D. G., Zehavi, I., & Zucker, D. B. 2008, ApJS, 175, 297

Arnold, R., & Gilmore, G. 1992, MNRAS, 257, 225

- Bailin, J., Power, C., Norberg, P., Zaritsky, D., & Gibson, B. K. 2008, *MNRAS*, 390, 1133
- Bellazzini, M. 2004, *MNRAS*, 347, 119
- Belokurov, V., Walker, M. G., Evans, N. W., Faria, D. C., Gilmore, G., Irwin, M. J., Koposov, S., Mateo, M., Olszewski, E., & Zucker, D. B. 2008, *ApJ*, 686, L83
- Belokurov, V., Zucker, D. B., Evans, N. W., Gilmore, G., Vidrih, S., Bramich, D. M., Newberg, H. J., Wyse, R. F. G., Irwin, M. J., Fellhauer, M., Hewett, P. C., Walton, N. A., Wilkinson, M. I., Cole, N., Yanny, B., Rockosi, C. M., Beers, T. C., Bell, E. F., Brinkmann, J., Ivezić, Ž., & Lupton, R. 2006a, *ApJ*, 642, L137
- Belokurov, V., Zucker, D. B., Evans, N. W., Kleyna, J. T., Koposov, S., Hodgkin, S. T., Irwin, M. J., Gilmore, G., Wilkinson, M. I., Fellhauer, M., Bramich, D. M., Hewett, P. C., Vidrih, S., De Jong, J. T. A., Smith, J. A., Rix, H.-W., Bell, E. F., Wyse, R. F. G., Newberg, H. J., Mayeur, P. A., Yanny, B., Rockosi, C. M., Gnedin, O. Y., Schneider, D. P., Beers, T. C., Barentine, J. C., Brewington, H., Brinkmann, J., Harvanek, M., Kleinman, S. J., Krzesinski, J., Long, D., Nitta, A., & Snedden, S. A. 2007, *ApJ*, 654, 897
- Belokurov, V., Zucker, D. B., Evans, N. W., Wilkinson, M. I., Irwin, M. J., Hodgkin, S., Bramich, D. M., Irwin, J. M., Gilmore, G., Willman, B., Vidrih, S., Newberg, H. J., Wyse, R. F. G., Fellhauer, M., Hewett, P. C., Cole, N., Bell, E. F., Beers, T. C., Rockosi, C. M., Yanny, B., Grebel, E. K., Schneider, D. P., Lupton, R., Barentine, J. C., Brewington, H., Brinkmann, J., Harvanek, M., Kleinman, S. J., Krzesinski, J., Long, D., Nitta, A., Smith, J. A., & Snedden, S. A. 2006b, *ApJ*, 647, L111
- Bertin, E., & Arnouts, S. 1996, *A&AS*, 117, 393
- Binney, J., & Tremaine, S. 1987, *Galactic dynamics* (Princeton, NJ, Princeton University Press, 1987, 747 p.)
- Bode, P., Ostriker, J. P., & Turok, N. 2001, *ApJ*, 556, 93
- Brainerd, T. G. 2005, *ApJ*, 628, L101
- Bullock, J. S., Kravtsov, A. V., & Weinberg, D. H. 2000, *ApJ*, 539, 517
- . 2001, *ApJ*, 548, 33
- Cho, D.-H., Lee, S.-G., Jeon, Y.-B., & Sim, K. J. 2005, *AJ*, 129, 1922
- Clem, J., VandenBerg, D., & Stetson, P. 2007, *AJ* submitted, astro-ph/0711.4045
- Colín, P., Avila-Reese, V., & Valenzuela, O. 2000, *ApJ*, 542, 622

- Colless, M., Dalton, G., Maddox, S., Sutherland, W., Norberg, P., Cole, S., Bland-Hawthorn, J., Bridges, T., Cannon, R., Collins, C., Couch, W., Cross, N., Deeley, K., De Propriis, R., Driver, S. P., Efstathiou, G., Ellis, R. S., Frenk, C. S., Glazebrook, K., Jackson, C., Lahav, O., Lewis, I., Lumsden, S., Madgwick, D., Peacock, J. A., Peterson, B. A., Price, I., Seaborne, M., & Taylor, K. 2001, *MNRAS*, 328, 1039
- Dabringhausen, J., Hilker, M., & Kroupa, P. 2008, *MNRAS*, 386, 864
- de Jong, J. T. A., Harris, J., Coleman, M. G., Martin, N. F., Bell, E. F., Rix, H.-W., Hill, J. M., Skillman, E. D., Sand, D. J., Olszewski, E. W., Zaritsky, D., Thompson, D., Giallongo, E., Ragazzoni, R., DiPaola, A., Farinato, J., Testa, V., & Bechtold, J. 2008, *ApJ*, 680, 1112
- Dekel, A., & Silk, J. 1986, *ApJ*, 303, 39
- Dias, W. S., Alessi, B. S., Moitinho, A., & Lépine, J. R. D. 2002, *A&A*, 389, 871
- Diemand, J., Kuhlen, M., & Madau, P. 2007, *ApJ*, 667, 859
- Dotter, A., Chaboyer, B., Jevremovic, D., Kostov, V., Baron, E., & Ferguson, J. W. 2008, *ArXiv e-prints*, 804
- Frenk, C. S., Evrard, A. E., White, S. D. M., & Summers, F. J. 1996, *ApJ*, 472, 460
- Fukugita, M., Ichikawa, T., Gunn, J. E., Doi, M., Shimasaku, K., & Schneider, D. P. 1996, *AJ*, 111, 1748
- Ghigna, S., Moore, B., Governato, F., Lake, G., Quinn, T., & Stadel, J. 1998, *MNRAS*, 300, 146
- Gilmore, G., Wilkinson, M. I., Wyse, R. F. G., Kleyna, J. T., Koch, A., Evans, N. W., & Grebel, E. K. 2007, *ApJ*, 663, 948
- Girardi, L., Grebel, E. K., Odenkirchen, M., & Chiosi, C. 2004, *A&A*, 422, 205
- González, R. E., Lares, M., Lambas, D. G., & Valotto, C. 2006, *A&A*, 445, 51
- Gouliermis, D., Kontizas, M., Kontizas, E., & Korakitis, R. 2003, *A&A*, 405, 111
- Grebel, E. K., Gallagher, III, J. S., & Harbeck, D. 2003, *AJ*, 125, 1926
- Grillmair, C. J., & Dionatos, O. 2006, *ApJ*, 641, L37
- Grundahl, F., Stetson, P. B., & Andersen, M. I. 2002, *A&A*, 395, 481
- Gunn, J. E., Carr, M., Rockosi, C., Sekiguchi, M., Berry, K., Elms, B., de Haas, E., Ivezić, Ž., Knapp, G., Lupton, R., Pauls, G., Simcoe, R., Hirsch, R., Sanford, D., Wang, S., York, D., Harris, F., Annis, J., Bartozek, L., Boroski, W., Bakken, J., Haldeman, M., Kent, S., Holm, S., Holmgren, D., Petravick, D., Prosapio, A., Rechenmacher, R., Doi, M., Fukugita, M., Shimasaku, K., Okada, N., Hull, C.,

- Siegmund, W., Mannery, E., Blouke, M., Heidtman, D., Schneider, D., Lucinio, R., & Brinkman, J. 1998, *AJ*, 116, 3040
- Harris, J. 2007, *ApJ*, 658, 345
- Harris, W. E. 1996, *AJ*, 112, 1487
- Hogg, D. W., Finkbeiner, D. P., Schlegel, D. J., & Gunn, J. E. 2001, *AJ*, 122, 2129
- Holmberg, E. 1969, *Arkiv for Astronomi*, 5, 305
- Holtzman, J. A., Afonso, C., & Dolphin, A. 2006, *ApJS*, 166, 534
- Hubble, E., & Humason, M. L. 1931, *ApJ*, 74, 43
- Ibata, R., Irwin, M., Lewis, G. F., & Stolte, A. 2001, *ApJ*, 547, L133
- Ibata, R. A., Gilmore, G., & Irwin, M. J. 1994, *Nature*, 370, 194
- Irwin, M. J. 1994, in *Dwarf Galaxies*, ed. G. Meylan & P. Prugniel, 27–+
- Irwin, M. J., Belokurov, V., Evans, N. W., Ryan-Weber, E. V., de Jong, J. T. A., Koposov, S., Zucker, D. B., Hodgkin, S. T., Gilmore, G., Prema, P., Hebb, L., Begum, A., Fellhauer, M., Hewett, P. C., Kennicutt, Jr., R. C., Wilkinson, M. I., Bramich, D. M., Vidrih, S., Rix, H.-W., Beers, T. C., Barentine, J. C., Brewington, H., Harvanek, M., Krzesinski, J., Long, D., Nitta, A., & Snedden, S. A. 2007, *ApJ*, 656, L13
- Ivezić, Ž., Lupton, R. H., Schlegel, D., Boroski, B., Adelman-McCarthy, J., Yanny, B., Kent, S., Stoughton, C., Finkbeiner, D., Padmanabhan, N., Rockosi, C. M., Gunn, J. E., Knapp, G. R., Strauss, M. A., Richards, G. T., Eisenstein, D., Nicinski, T., Kleinman, S. J., Krzesinski, J., Newman, P. R., Snedden, S., Thakar, A. R., Szalay, A., Munn, J. A., Smith, J. A., Tucker, D., & Lee, B. C. 2004, *Astronomische Nachrichten*, 325, 583
- Ivezic, Z., Tyson, J. A., Allsman, R., Andrew, J., Angel, R., & for the LSST Collaboration. 2008, *ArXiv e-prints*, 805
- Kaiser, N. 2004, in *Presented at the Society of Photo-Optical Instrumentation Engineers (SPIE) Conference, Vol. 5489, Ground-based Telescopes*. Edited by Oschmann, Jacobus M., Jr. *Proceedings of the SPIE, Volume 5489*, pp. 11-22 (2004)., ed. J. M. Oschmann, Jr., 11–22
- Kamionkowski, M., & Liddle, A. R. 2000, *Physical Review Letters*, 84, 4525
- Kang, X., Mao, S., Gao, L., & Jing, Y. P. 2005, *A&A*, 437, 383
- Kaplinghat, M., Knox, L., & Turner, M. S. 2000, *Physical Review Letters*, 85, 3335
- Katz, N., & White, S. D. M. 1993, *ApJ*, 412, 455

- Kauffmann, G., White, S. D. M., & Guiderdoni, B. 1993, *MNRAS*, 264, 201
- Keller, S. C., Schmidt, B. P., Bessell, M. S., Conroy, P. G., Francis, P., Granlund, A., Kowald, E., Oates, A. P., Martin-Jones, T., Preston, T., Tisserand, P., Vaccarella, A., & Waterson, M. F. 2007, *Publications of the Astronomical Society of Australia*, 24, 1
- King, I. R. 1966, *AJ*, 71, 64
- Kleyna, J. T., Geller, M. J., Kenyon, S. J., & Kurtz, M. J. 1997, *AJ*, 113, 624
- Kleyna, J. T., Wilkinson, M. I., Evans, N. W., & Gilmore, G. 2001, *ApJ*, 563, L115
- Klypin, A., Gottlöber, S., Kravtsov, A. V., & Khokhlov, A. M. 1999a, *ApJ*, 516, 530
- Klypin, A., Kravtsov, A. V., Valenzuela, O., & Prada, F. 1999b, *ApJ*, 522, 82
- Klypin, A., Zhao, H., & Somerville, R. S. 2002, *ApJ*, 573, 597
- Koposov, S., Belokurov, V., Evans, N. W., Hewett, P. C., Irwin, M. J., Gilmore, G., Zucker, D. B., Rix, H.-W., Fellhauer, M., Bell, E. F., & Glushkova, E. V. 2008, *ApJ*, 686, 279
- Koposov, S., de Jong, J. T. A., Belokurov, V., Rix, H.-W., Zucker, D. B., Evans, N. W., Gilmore, G., Irwin, M. J., & Bell, E. F. 2007, *ApJ*, 669, 337
- Kraft, R. P., & Ivans, I. I. 2003, *PASP*, 115, 143
- Kravtsov, A. V., Gnedin, O. Y., & Klypin, A. A. 2004, *ApJ*, 609, 482
- Kroupa, P., Theis, C., & Boily, C. M. 2005, *A&A*, 431, 517
- Kunkel, W. E. 1979, *ApJ*, 228, 718
- Libeskind, N. I., Frenk, C. S., Cole, S., Helly, J. C., Jenkins, A., Navarro, J. F., & Power, C. 2005, *MNRAS*, 363, 146
- Liu, C., Hu, J., Newberg, H., & Zhao, Y. 2008, *A&A*, 477, 139
- Lynden-Bell, D. 1982, *The Observatory*, 102, 202
- Majewski, S. R. 1994, *ApJ*, 431, L17
- Majewski, S. R., Munn, J. A., & Hawley, S. L. 1996, *ApJ*, 459, L73+
- Majewski, S. R., Skrutskie, M. F., Weinberg, M. D., & Ostheimer, J. C. 2003, *ApJ*, 599, 1082
- Martin, N. F., de Jong, J. T. A., & Rix, H.-W. 2008, *ApJ*, 684, 1075
- Martin, N. F., Ibata, R. A., Chapman, S. C., Irwin, M., & Lewis, G. F. 2007, *MNRAS*, 380, 281

- Martínez-Delgado, D., Aparicio, A., Gómez-Flechoso, M. Á., & Carrera, R. 2001, *ApJ*, 549, L199
- Mateo, M. L. 1998, *ARA&A*, 36, 435
- Mayer, L., Mastropietro, C., Wadsley, J., Stadel, J., & Moore, B. 2006, *MNRAS*, 369, 1021
- McConnachie, A. W., Huxor, A., Martin, N. F., Irwin, M. J., Chapman, S. C., Fahlman, G., Ferguson, A. M. N., Ibata, R. A., Lewis, G. F., Richer, H., & Tanvir, N. R. 2008, *ApJ*, 688, 1009
- McConnachie, A. W., & Irwin, M. J. 2006, *MNRAS*, 365, 1263
- McLaughlin, D. E., & van der Marel, R. P. 2005, *ApJS*, 161, 304
- McLeod, B. A., Conroy, M., Gauron, T. M., Geary, J. C., & Ordway, M. P. 2000, in *Further Developments in Scientific Optical Imaging*, ed. M. B. Denton, 11–+
- Metz, M., Kroupa, P., & Jerjen, H. 2007, *MNRAS*, 374, 1125
- Metz, M., Kroupa, P., & Libeskind, N. I. 2008, *ApJ*, 680, 287
- Moore, B., Ghigna, S., Governato, F., Lake, G., Quinn, T., Stadel, J., & Tozzi, P. 1999, *ApJ*, 524, L19
- Moore, B., Governato, F., Quinn, T., Stadel, J., & Lake, G. 1998, *ApJ*, 499, L5+
- Moore, B., Katz, N., & Lake, G. 1996, *ApJ*, 457, 455
- Mori, M., Ferrara, A., & Madau, P. 2002, *ApJ*, 571, 40
- Muñoz, R. R., Majewski, S. R., & Johnston, K. V. 2008, *ApJ*, 679, 346
- Natarajan, P., Croton, D., & Bertone, G. 2008, *MNRAS*, 388, 1652
- Newberg, H. J., Yanny, B., Rockosi, C., Grebel, E. K., Rix, H.-W., Brinkmann, J., Csabai, I., Hennessy, G., Hindsley, R. B., Ibata, R., Ivezić, Z., Lamb, D., Nash, E. T., Odenkirchen, M., Rave, H. A., Schneider, D. P., Smith, J. A., Stolte, A., & York, D. G. 2002, *ApJ*, 569, 245
- Okamoto, T., & Habe, A. 1999, *ApJ*, 516, 591
- Okazaki, T., & Taniguchi, Y. 2000, *ApJ*, 543, 149
- Padmanabhan, N., Schlegel, D. J., Finkbeiner, D. P., Barentine, J. C., Blanton, M. R., Brewington, H. J., Gunn, J. E., Harvanek, M., Hogg, D. W., Ivezić, Ž., Johnston, D., Kent, S. M., Kleinman, S. J., Knapp, G. R., Krzesinski, J., Long, D., Neilsen, Jr., E. H., Nitta, A., Loomis, C., Lupton, R. H., Roweis, S., Snedden, S. A., Strauss, M. A., & Tucker, D. L. 2008, *ApJ*, 674, 1217

- Paust, N. E. Q., Chaboyer, B., & Sarajedini, A. 2007, *AJ*, 133, 2787
- Peebles, P. J. E. 1965, *ApJ*, 142, 1317
- Penzias, A. A., & Wilson, R. W. 1965, *ApJ*, 142, 419
- Piatek, S., Pryor, C., Bristow, P., Olszewski, E. W., Harris, H. C., Mateo, M., Minniti, D., & Tinney, C. G. 2007, *AJ*, 133, 818
- Pier, J. R., Munn, J. A., Hindsley, R. B., Hennessy, G. S., Kent, S. M., Lupton, R. H., & Ivezić, Ž. 2003, *AJ*, 125, 1559
- Plummer, H. C. 1911, *MNRAS*, 71, 460
- Press, W. H., & Schechter, P. 1974, *ApJ*, 187, 425
- Pritzl, B. J., Venn, K. A., & Irwin, M. 2005, *AJ*, 130, 2140
- Rider, C. J., Tucker, D. L., Smith, J. A., Stoughton, C., Allam, S. S., & Neilsen, Jr., E. H. 2004, *AJ*, 127, 2210
- Sakamoto, T., & Hasegawa, T. 2006, *ApJ*, 653, L29
- Schlegel, D. J., Finkbeiner, D. P., & Davis, M. 1998a, *ApJ*, 500, 525
- . 1998b, *ApJ*, 500, 525
- Searle, L., & Zinn, R. 1978, *ApJ*, 225, 357
- Simon, J. D., & Geha, M. 2007, *ApJ*, 670, 313
- Skrutskie, M. F., Cutri, R. M., Stiening, R., Weinberg, M. D., Schneider, S., Carpenter, J. M., Beichman, C., Capps, R., Chester, T., Elias, J., Huchra, J., Liebert, J., Lonsdale, C., Monet, D. G., Price, S., Seitzer, P., Jarrett, T., Kirkpatrick, J. D., Gizis, J. E., Howard, E., Evans, T., Fowler, J., Fullmer, L., Hurt, R., Light, R., Kopan, E. L., Marsh, K. A., McCallon, H. L., Tam, R., Van Dyk, S., & Wheelock, S. 2006, *AJ*, 131, 1163
- Smith, J. A., Tucker, D. L., Kent, S., Richmond, M. W., Fukugita, M., Ichikawa, T., Ichikawa, S.-i., Jorgensen, A. M., Uomoto, A., Gunn, J. E., Hamabe, M., Watanabe, M., Tolea, A., Henden, A., Annis, J., Pier, J. R., McKay, T. A., Brinkmann, J., Chen, B., Holtzman, J., Shimasaku, K., & York, D. G. 2002, *AJ*, 123, 2121
- Snedden, C., Pilachowski, C. A., & Kraft, R. P. 2000, *AJ*, 120, 1351
- Somerville, R. S. 2002, *ApJ*, 572, L23
- Spergel, D. N., Bean, R., Doré, O., Nolta, M. R., Bennett, C. L., Dunkley, J., Hinshaw, G., Jarosik, N., Komatsu, E., Page, L., Peiris, H. V., Verde, L., Halpern, M., Hill, R. S., Kogut, A., Limon, M., Meyer, S. S., Odegard, N., Tucker, G. S., Weiland, J. L., Wollack, E., & Wright, E. L. 2007, *ApJS*, 170, 377

- Spergel, D. N., & Steinhardt, P. J. 2000, *Physical Review Letters*, 84, 3760
- Stetson, P. B. 1994, *PASP*, 106, 250
- Strigari, L. E., Bullock, J. S., Kaplinghat, M., Diemand, J., Kuhlen, M., & Madau, P. 2007a, *ApJ*, 669, 676
- Strigari, L. E., Kaplinghat, M., & Bullock, J. S. 2007b, *Phys. Rev. D*, 75, 061303
- Strigari, L. E., Koushiappas, S. M., Bullock, J. S., Kaplinghat, M., Simon, J. D., Geha, M., & Willman, B. 2008, *ApJ*, 678, 614
- Summers, F. J., Davis, M., & Evrard, A. E. 1995, *ApJ*, 454, 1
- Tollerud, E. J., Bullock, J. S., Strigari, L. E., & Willman, B. 2008, *ApJ*, 688, 277
- Tucker, D. L., Kent, S., Richmond, M. W., Annis, J., Smith, J. A., Allam, S. S., Rodgers, C. T., Stute, J. L., Adelman-McCarthy, J. K., Brinkmann, J., Doi, M., Finkbeiner, D., Fukugita, M., Goldston, J., Greenway, B., Gunn, J. E., Hendry, J. S., Hogg, D. W., Ichikawa, S.-I., Ivezić, Ž., Knapp, G. R., Lampeitl, H., Lee, B. C., Lin, H., McKay, T. A., Merrelli, A., Munn, J. A., Neilsen, Jr., E. H., Newberg, H. J., Richards, G. T., Schlegel, D. J., Stoughton, C., Uomoto, A., & Yanny, B. 2006, *Astronomische Nachrichten*, 327, 821
- Volders, L. M. J. S. 1959, *Bull. Astron. Inst. Netherlands*, 14, 323
- Walker, M. G., Mateo, M., Olszewski, E. W., Gnedin, O. Y., Wang, X., Sen, B., & Woodroffe, M. 2007, *ApJ*, 667, L53
- Walsh, S., Willman, B., & Jerjen, H. 2008a, *ArXiv e-prints*, 807
- Walsh, S. M., Jerjen, H., & Willman, B. 2007, *ApJ*, 662, L83
- Walsh, S. M., Willman, B., Sand, D., Harris, J., Seth, A., Zaritsky, D., & Jerjen, H. 2008b, *ApJ*, 688, 245
- White, S. D. M., & Frenk, C. S. 1991, *ApJ*, 379, 52
- White, S. D. M., & Rees, M. J. 1978, *MNRAS*, 183, 341
- Whiting, A. B., Hau, G. K. T., Irwin, M., & Verdugo, M. 2007, *AJ*, 133, 715
- Willman, B. 2003, PhD thesis, University of Washington
- Willman, B., Blanton, M. R., West, A. A., Dalcanton, J. J., Hogg, D. W., Schneider, D. P., Wherry, N., Yanny, B., & Brinkmann, J. 2005a, *AJ*, 129, 2692
- Willman, B., Dalcanton, J., Ivezić, Ž., Jackson, T., Lupton, R., Brinkmann, J., Hennesy, G., & Hindsley, R. 2002, *AJ*, 123, 848

- Willman, B., Dalcanton, J. J., Martinez-Delgado, D., West, A. A., Blanton, M. R., Hogg, D. W., Barentine, J. C., Brewington, H. J., Harvanek, M., Kleinman, S. J., Krzesinski, J., Long, D., Neilsen, Jr., E. H., Nitta, A., & Snedden, S. A. 2005b, *ApJ*, 626, L85
- Willman, B., Governato, F., Dalcanton, J. J., Reed, D., & Quinn, T. 2004, *MNRAS*, 353, 639
- York, D. G., Adelman, J., Anderson, Jr., J. E., Anderson, S. F., Annis, J., Bahcall, N. A., Bakken, J. A., Barkhouser, R., Bastian, S., Berman, E., Boroski, W. N., Bracker, S., Briegel, C., Briggs, J. W., Brinkmann, J., Brunner, R., Burles, S., Carey, L., Carr, M. A., Castander, F. J., Chen, B., Colestock, P. L., Connolly, A. J., Crocker, J. H., Csabai, I., Czarapata, P. C., Davis, J. E., Doi, M., Dombeck, T., Eisenstein, D., Ellman, N., Elms, B. R., Evans, M. L., Fan, X., Federwitz, G. R., Fiscelli, L., Friedman, S., Frieman, J. A., Fukugita, M., Gillespie, B., Gunn, J. E., Gurbani, V. K., de Haas, E., Haldeman, M., Harris, F. H., Hayes, J., Heckman, T. M., Hennessy, G. S., Hindsley, R. B., Holm, S., Holmgren, D. J., Huang, C.-h., Hull, C., Husby, D., Ichikawa, S.-I., Ichikawa, T., Ivezić, Ž., Kent, S., Kim, R. S. J., Kinney, E., Klaene, M., Kleinman, A. N., Kleinman, S., Knapp, G. R., Korienek, J., Kron, R. G., Kunszt, P. Z., Lamb, D. Q., Lee, B., Leger, R. F., Limmongkol, S., Lindenmeyer, C., Long, D. C., Loomis, C., Loveday, J., Lucinio, R., Lupton, R. H., MacKinnon, B., Mannery, E. J., Mantsch, P. M., Margon, B., McGehee, P., McKay, T. A., Meiksin, A., Merelli, A., Monet, D. G., Munn, J. A., Narayanan, V. K., Nash, T., Neilsen, E., Neswold, R., Newberg, H. J., Nichol, R. C., Nicinski, T., Nonino, M., Okada, N., Okamura, S., Ostriker, J. P., Owen, R., Pauls, A. G., Peoples, J., Peterson, R. L., Petravick, D., Pier, J. R., Pope, A., Pordes, R., Prosapio, A., Rechenmacher, R., Quinn, T. R., Richards, G. T., Richmond, M. W., Rivetta, C. H., Rockosi, C. M., Ruthmansdorfer, K., Sandford, D., Schlegel, D. J., Schneider, D. P., Sekiguchi, M., Sergey, G., Shimasaku, K., Siegmund, W. A., Smee, S., Smith, J. A., Snedden, S., Stone, R., Stoughton, C., Strauss, M. A., Stubbs, C., SubbaRao, M., Szalay, A. S., Szapudi, I., Szokoly, G. P., Thakar, A. R., Tremonti, C., Tucker, D. L., Uomoto, A., Vanden Berk, D., Vogeley, M. S., Waddell, P., Wang, S.-i., Watanabe, M., Weinberg, D. H., Yanny, B., & Yasuda, N. 2000a, *AJ*, 120, 1579
- . 2000b, *AJ*, 120, 1579
- Zentner, A. R., & Bullock, J. S. 2003, *ApJ*, 598, 49
- Zentner, A. R., Kravtsov, A. V., Gnedin, O. Y., & Klypin, A. A. 2005, *ApJ*, 629, 219
- Zucker, D. B., Belokurov, V., Evans, N. W., Kleyna, J. T., Irwin, M. J., Wilkinson, M. I., Fellhauer, M., Bramich, D. M., Gilmore, G., Newberg, H. J., Yanny, B., Smith, J. A., Hewett, P. C., Bell, E. F., Rix, H.-W., Gnedin, O. Y., Vidrih, S., Wyse, R. F. G., Willman, B., Grebel, E. K., Schneider, D. P., Beers, T. C., Kniazev, A. Y., Barentine, J. C., Brewington, H., Brinkmann, J., Harvanek, M., Kleinman, S. J., Krzesinski, J., Long, D., Nitta, A., & Snedden, S. A. 2006a, *ApJ*, 650, L41

- Zucker, D. B., Belokurov, V., Evans, N. W., Wilkinson, M. I., Irwin, M. J., Sivarani, T., Hodgkin, S., Bramich, D. M., Irwin, J. M., Gilmore, G., Willman, B., Vidrih, S., Fellhauer, M., Hewett, P. C., Beers, T. C., Bell, E. F., Grebel, E. K., Schneider, D. P., Newberg, H. J., Wyse, R. F. G., Rockosi, C. M., Yanny, B., Lupton, R., Smith, J. A., Barentine, J. C., Brewington, H., Brinkmann, J., Harvanek, M., Kleinman, S. J., Krzesinski, J., Long, D., Nitta, A., & Snedden, S. A. 2006b, *ApJ*, 643, L103
- Zucker, D. B., Kniazev, A. Y., Bell, E. F., Martínez-Delgado, D., Grebel, E. K., Rix, H.-W., Rockosi, C. M., Holtzman, J. A., Walterbos, R. A. M., Annis, J., York, D. G., Ivezić, Ž., Brinkmann, J., Brewington, H., Harvanek, M., Hennessy, G., Kleinman, S. J., Krzesinski, J., Long, D., Newman, P. R., Nitta, A., & Snedden, S. A. 2004, *ApJ*, 612, L121
- Zucker, D. B., Kniazev, A. Y., Martínez-Delgado, D., Bell, E. F., Rix, H.-W., Grebel, E. K., Holtzman, J. A., Walterbos, R. A. M., Rockosi, C. M., York, D. G., Barentine, J. C., Brewington, H., Brinkmann, J., Harvanek, M., Kleinman, S. J., Krzesinski, J., Long, D., Neilsen, Jr., E. H., Nitta, A., & Snedden, S. A. 2007, *ApJ*, 659, L21
- Zwicky, F. 1937, *ApJ*, 86, 217